AN ABSTRACT OF THE DISSERTATION OF

Ryan T. Armstrong for the degree of Doctor of Philosophy in Chemical Engineering
Presented on January 6, 2012

Title: Microbial Enhanced Oil Recovery: A Pore-Scale Investigation of Interfacial Interactions

Abstract approved:

Dorthe Wildenschild

Current oil production technologies recover only about one-third to one-half of the oil originally present in an oil reservoir. Given current oil prices, even a modest increase in oil recovery efficiency is fiscally attractive. One novel approach to increase oil recovery efficiency is a process called microbial enhanced oil recovery (MEOR), where microorganisms are either used as a clogging agent to redirect flow or to produce biosurfactant that reduces interfacial tension. This dissertation aims to understand the MEOR pore-scale mechanisms relevant to oil recovery by taking a two-fold approach where transparent 2-dimensional micromodel experiments imaged with stereo microscopy and 3-dimensional column experiments imaged with x-ray computed microtomography (CMT) are utilized. Micromodel experiments allow for direct visualization of the biological phase (i.e. biofilm), however, only 2-dimensional information is provided. Conversely, CMT experiments provide 3-dimensional pore-scale information, but lack the ability to image the biological phase. With this two-fold approach, it is possible to distinguish multiple fluid interfaces, quantify fluid phase saturations, measure oil blob size distributions, and visualize the biological phase. Furthermore, a method to measure interfacial curvature from 3-dimensional images is developed, providing researchers a new perspective from which to study multiphase flow experiments. Overall, the presented research utilizes pore-scale imaging techniques to study the interfacial interactions occurring during MEOR in an effort to better explain the physics, and thus, increase the efficacy of MEOR.

©Copyright by Ryan T. Armstrong
January 6, 2012
All Right Reserved

Microbial Enhanced Oil Recovery: A Pore-Scale Investigation of Interfacial Interactions

by

Ryan T. Armstrong

A DISSERTATION

Submitted to

Oregon State University

in partial fulfillment of
the requirement for the
degree of

Doctor of Philosophy

Presented January 6, 2012
Commencement June 2012

Doctor of Philosophy dissertation of Ryan T. Armstrong presented on January 6, 2012

APPROVED:

Major Professor, representing Chemical Engineering

Head of the School of Chemical, Biological and Environmental Engineering

Dean of the Graduate School

I understand that my dissertation will become part of the permanent collection of Oregon State University libraries. My signature below authorizes release of my dissertation to any reader upon request.

Ryan T. Armstrong, Author

ACKNOWLEDGMENTS

First and foremost, I would like to thank my research advisor Dorthe Wildenschild, whose guidance, patience, technical skills, and encouragement was pivotal in the completion of this dissertation. I would also like to thank my parents Dorothy and Lorin Armstrong for their love and constant encouragement. Furthermore, I thank Gabriel Iltis for his support and friendship.

CONTRIBUTION OF AUTHORS

This research would not have been completed without the technical assistance of many highly skilled researchers. Mark Porter provided the experimental data and editorial support for the research presented in Chapter 3. Kendra Brown designed the micromodel pattern, micromodel holder, and UV contrast agent method used for the experiments presented in Chapter 4. Gabriel Iltis, James Connolly, Yohan Davit, and Mark Rivers assisted with the experiments presented in Chapter 5. Brian Bay supported the cone-beam tomography instrument used for the experiments presented in Chapter 6. Jonathan Ajo-Franklin supervised the research presented in Appendix A. Gabriel Iltis completed the image processing for the research presented in Appendix B and undertook the publication responsibilities. Dorthe Wildenschild provided technical and editorial support for all of the research presented in this dissertation.

TABLE OF CONTENTS

Page

TABLE OF CONTENTS (Continued)

TABLE OF CONTENTS (Continued)

LIST OF FIGURES

LIST OF FIGURES (Continued)

LIST OF FIGURES (Continued)

LIST OF FIGURES (Continued)

LIST OF TABLES

LIST OF APPENDICES

Appendix Page

LIST OF APPENDIX FIGURES

“I was born not knowing and have had only a little time to change that here and there.”

Richard P. Feynman

Microbial Enhanced Oil recovery: A Pore-scale Investigation of Interfacial Interactions

Chapter 1. Introduction

1.1 Overview

The world's energy demand is ever increasing. For instance, the United States energy demand, over the past 100 years, has increased from approximately 100 to over 350 millions of BTUs per person per year (U.S. Department of Energy, U.S. Census Bureau). Currently, this energy demand is satisfied with petroleum fuels, a significant fraction of which come from mature oil reservoirs. However, the replacement rate of mature reservoirs with new discoveries has declined steadily over the last two decades. Production decline was first predicted by geophysicist M. King Hubbert in 1956, who used a logistic distribution model to estimate that net oil production would peak around 1970. Due to production decline, increased oil recovery efficiency from mature oil formations has become increasingly important. In most mature oil reservoirs, approximately 40-60% of the original oil in place still remains in place, as a result of recovery inefficiencies (Baviere, 1991). Between 1994 and 2003, approximately 17.5 million m^3 of oil was lost because of premature abandonment of marginal oil wells. However, enhanced oil recovery (EOR) technologies that target residual oil need further development, which is reflected by the fact that currently only 0.3 million m^3 per day of crude oil is recovered from mature oil formations (U.S. Energy Information Administration, 2011).

Microbial enhanced oil recovery (MEOR) is a novel approach where microorganisms and/or their metabolic by-products are utilized to facilitate the mobilization of residual oil from mature oil reservoirs (Youssef et al. 2009). Compared to other enhanced oil recovery technologies, MEOR is economically advantageous since microorganisms require minimal energy input (Lazar et al. 2007; Thomas et al. 2008; Brown et al. 2010). Whereas, thermal-based enhanced oil recovery technologies have a large energy demand and chemical-based EOR technologies use synthetic chemicals derived from petroleum-based compounds (Lazar et al. 2007). Alternatively, microorganisms produce products from renewable resources and can produce a large quantity of product over a relatively short timespan, due to their exponential growth rate (Maneerat et al. 2004; Mukherjee et al. 2006). However, the MEOR

mechanisms through which recovery efficiency increases and the essential parameters for understanding/modeling this technology are mostly unknown.

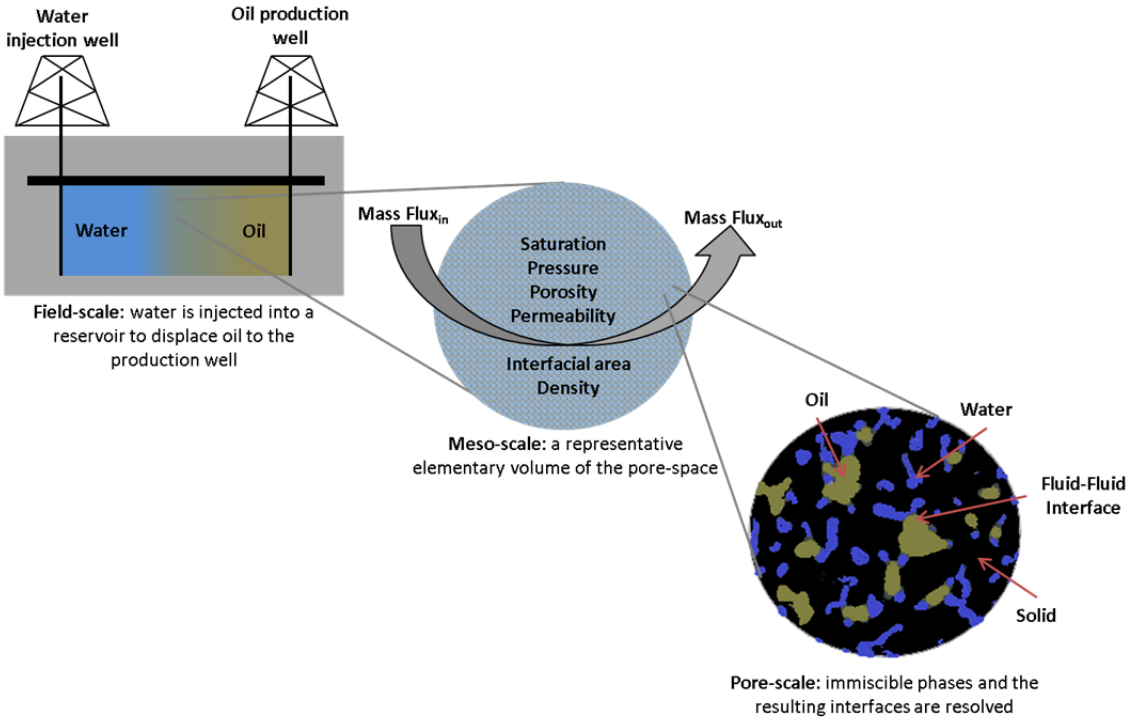

Figure 1.1: The range of length scales relevant to microbial enhanced oil recovery. Accurate characterization at the pore-scale and meso-scale are required for a successful field-scale operation.

As with most engineered systems (e.g. multiphase flow applications) many different length scales exist. Figure 1.1 shows the relationship between length scales ranging from the pore-scale to the field-scale. At the pore-scale individual grains are resolved, along with the spatial arrangement of each fluid phase, and the resulting interfaces between immiscible phases. At the meso-scale, pore-scale parameters are averaged over a representative elementary volume and explicit spatial information is lost. However, averaging is essential, since including all of the pore-scale information into a field-scale model would produce an overly complex model. The crux is to identify the relevant pore-scale parameters and to incorporate only these parameters into the final predictive field-scale model. The importance of pore-scale parameters for the accurate prediction of larger-scale multiphase flow phenomena is demonstrated by various researchers (Chen and Doolen 1998; Karpyn and Piri 2007a; 2007b;

Porter et al. 2010; Joekar-Niasar et al. 2010). However, a fundamental understanding of the pore-scale parameters essential to MEOR and how microorganisms affect the pore-scale physics is currently unknown. The aim of this dissertation is to understand the pertinent pore-scale process dynamics and interfacial interactions, such that, potential candidate oil reservoirs can be effectively identified, resulting in successful microbial enhanced oil recovery operations.

1.2 Research Objectives

The term microbial enhanced oil recovery encompasses any oil recovery operation that utilizes microorganisms, and thus, depending on the bacteria or bacterium used, distinctly different oil recovery mechanisms are possible. The presented research focuses on biosurfactant-facilitated and biomass-facilitated MEOR (see Section 2.4). The goal of this research is to understand the pore-scale physics of biosurfactant-facilitated and biomass-facilitated MEOR by performing micromodel and column experiments that can be imaged with stereo microscopy or computed microtomography, respectively. Quantitative information is extracted from the pore-scale images and then related to reservoir parameters, such as, pore morphology and wettability. The overall focus is to understand the differences in oil recovery with a biosurfactant or with a biosurfactant and bioclogging and in which reservoir type one approach would be preferred over the other by evaluating the pore-scale physics of both approaches. Additionally, this research aims to identify and provide the parameters essential for developing and calibrating predictive numerical models. The specific objectives of this research are listed below:

1. Develop and validate a method to measure the interfacial curvature of fluid-fluid interfaces from 3-dimensional pore-scale images.

2. Identify how the MEOR mechanisms of biosurfactant-facilitated and biomass-facilitated recovery compare to each other and to abiotic recovery where the flow rate of the flooding phase is increased.

3. Identify how porous systems of different inherent wettability lend themselves to biosurfactant-facilitated and/or biomass-facilitated oil recovery.

4. Identify how different porous media pore throat size distributions, pore body size distributions, and thus pore-scale spatial distribution of residual oil and oil blob morphology affect oil mobilization when using biosurfactant-facilitated and/or biomass-facilitated MEOR.

1.3 Organization

In Chapter 2, the current literature and concepts relevant to microbial enhanced oil recovery, and thus, multiphase flow in porous media are reviewed. Chapter 2 is divided into 5 sections: Section 2.1 Hydrocarbon Production, Section 2.2 Multiphase Flow, Section 2.3 Reservoir Characteristics, Section 2.4 Applied Microbiology, and Section 2.5 Pore-Scale Imaging. Section 2.1 covers the general life cycle of an oil reservoir and introduces the terminology specific to petroleum engineering. Section 2.2 introduces the pore-scale physics relevant to multiphase flow, the traditional approach to modeling multiphase flow, and the essential constitutive relationships for modeling multiphase flow. Moreover, viscous and capillary forces are introduced and the influences of these forces on common oil recovery practices are reviewed. In Section 2.4, basic reservoir characteristic, such as, pore morphology and wettability are explained. Section 2.5 introduces microbiology as applied to oil recovery and presents the potential MEOR mechanisms responsible for oil mobilization. Lastly, pore-scale imaging techniques are presented in Section 2.5, along with the concepts relevant to image processing, as used in this dissertation.

Chapters 3, 4, 5, and 6, specifically address the research objectives outlined in Section 1.2, each chapter corresponds to a manuscript that is either currently submitted or will be submitted for publication in a peer-reviewed journal. Chapter 3 presents and validates a method to measure capillary pressure from pore-scale computed microtomography data. Chapter 4 investigates the individual effect of each microbial enhanced oil recovery mechanism. Chapter 5 considers the effectiveness of microbial enhanced oil recovery in fractional-wet porous media, while chapter 6 explores the effect of inherent pore morphology on oil blob mobilization via MEOR. As a final point, Chapter 7 summarizes the presented research, the notable findings, and the potential future directions for the

presented research. Two additional published manuscripts are included in appendices A and B, which pertains to research, conducted utilizing computed microtomography. Even though the appendices are not directly related to the objectives of this dissertation; pore morphological changes due to biomineralization (Appendix A) and the imaging of biofilm with CMT (Appendix B) are relevant to potential MEOR applications and to investigating potential MEOR mechanisms, respectively.

Chapter 2. Microbial Enhanced Oil Recovery

Microbial enhanced oil recovery (MEOR) is a technology where bacteria and their metabolic by-products are utilized to recover additional oil from mature oil reservoirs that would otherwise be unrecoverable. As discussed by Bryant and Lockhart (2002), the issues with MEOR are similar to problems with any other enhanced oil recovery process, only with the added complexity of an active biological system. Thus, in addition to understanding hydrocarbon production, multiphase flow, and reservoir characteristics, a fundamental understanding of oil reservoir microbiology is essential to evaluate the efficacy of MEOR.

2.1 Hydrocarbon Production

The first stage of hydrocarbon production is primary recovery, where natural reservoir energy, such as gasdrive, waterdrive, or gravity drainage, displaces hydrocarbons from the reservoir into the wellbore and to the surface. During production, reservoir pressure declines and once it reaches a point where production rates become uneconomical, or when the proportions of gas or water in the production stream are too high, primary recovery operations are terminated (Baviere, 1991). At this stage approximately 10% of the original oil in place (OOIP) has been recovered (Ollivier and Magot, 2005). To improve recovery, secondary recovery techniques are undertaken where often an external fluid (e.g. water, CO_2) is injected into a reservoir through injection wells located in rock that is hydraulically connected with the production wells (Figure 1.1). The purpose of water flooding is to maintain reservoir pressure and to displace hydrocarbons toward the wellbore. Once the injection fluid is produced in considerable amounts at the production well, secondary recovery operations become uneconomical and are ceased.

After secondary recovery, as much as 60% of the OOIP remains trapped in the oil reservoir due to inefficiencies during the flooding process (Baviere, 1991). Interfacial tension between

immiscible phases and the intrinsic pore structure of a reservoir causes capillary trapping of oil droplets behind the waterfront. Additionally, due to oil reservoir heterogeneity, water flooding does not completely sweep a reservoir, and low permeability regions remain oil saturated while higher permeability zones are swept. A characteristic term called sweep efficiency is used to describe the percentage of a reservoir swept during a water flood. Other common terminologies used in the oil industry and throughout this dissertation are defined below.

$$Original\ Oil\ in\ Place(OOIP) = Volume\ of\ oil\ initially\ saturating\ a\ reservoir \quad (2.1)$$

$$Residual\ Oil\ Saturation(Sor)\ (\%) = (Xi / OOIP) * 100$$
$$Where,\ Xi = OOIP - Volume\ of\ oil\ collected\ after\ water\ flooding \quad (2.2)$$

$$Additional\ Oil\ Recovery(AOR)\ (\%) = \frac{(Tertiary\ recovered\ oil)}{(Oil\ in\ place\ after\ water\ flood)} * 100 \quad (2.3)$$

Enhanced oil recovery (EOR) would be the third stage of hydrocarbon production (often called tertiary recovery). During EOR, the OOIP that is either capillary trapped or located in low permeability zones that were not efficiently swept during secondary recovery are targeted for mobilization (Chapters 4, 5, and 6)

2.2 Multiphase Flow

An oil reservoir is unquestionably a multiphase system, characterized by the existence of two or more immiscible phases and the resulting interfaces between each immiscible phase (Dullien 1992). In the subsurface where flow rates are relatively slow, interfacial forces largely control the resulting hydrodynamics, and thus, oil recovery. To understand these interfacial effects, it is essential to first consider the fundamental physics of multiphase flow, then more complex scenarios such as what occurs during oil recovery can be investigated. A field-scale oil operation under secondary and tertiary recovery can be divided into two separate events: (1) dynamic imbibition (i.e. water flooding) and (2) capillary desaturation (i.e. tertiary recovery), both of which are discussed after a brief introduction to multiphase flow.

2.2.1 Basics of Multiphase Flow

Ultimately, the goal to modeling multiphase flow is to quantify the temporal and spatial variation of pressure and saturation. To model a given system, constitutive relationships, where physical measurements are incorporated into numerical models, are required. Additionally, a flow equation for each fluid phase and a mass conservation equation are necessary. A system specific model is derived by incorporating the constitutive relationships and the flow equations into the mass conservation equation. In the following paragraphs, the traditional approach to modeling multiphase flow will be presented (Bear 1988). Initially, a few physical laws that govern multiphase systems will be introduced, then the constitutive relationships for capillary pressure and relative permeability are discussed, and lastly the flow equation and the mass conservation equation are introduced.

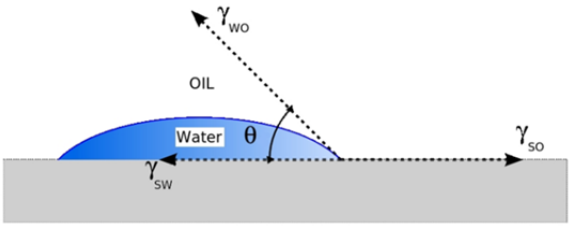

Figure 2.1: Contact angle measurement as defined in Young's equation.

In a multiphase system, immiscible phases are separated by interfaces (i.e. boundaries) across which discontinuities in pressure and density exist (Corey, 1997). For an oil/water system, three interfaces are readily identifiable: (1) oil-water, (2) oil-solid, and (3) water-solid. Along these interfaces there exists a force called interfacial tension (*γ),* which acts tangential to the interfacial boundary and is measured as force per length. When two immiscible fluids are in contact with a solid surface, the equilibrium configuration of the two fluid phases depends on the relative values of the interfacial tension (*γ*) between each pair of the three phases, solid, water, and oil, denoted as, *s*, *w*, and *o* (Figure 2.1). Each interfacial tension acts upon its respective interface and, at equilibrium, defines a unique angle θ, known as the wetting angle, defined by Young's equation.

$$\gamma_{wo}\cos(\theta) = \gamma_{so} - \gamma_{sw} \tag{2.4}$$

The wetting angle is measured as the angle subtended by the tangent to the water-oil interface and the tangent to the water-solid interface constructed at the point formed by the intersection of the three phases (Butt et al. 2006). When one fluid preferentially covers a surface, it is called the wetting phase and the other fluid is called the non-wetting phase. In Figure 2.1 water is considered the wetting phase for θ < 45°, non-wetting phase for θ > 135°, and moderate-wetting or moderate non-wetting phase for 45° > θ < 135° (Lake, 1996 and Marmur, 2009).

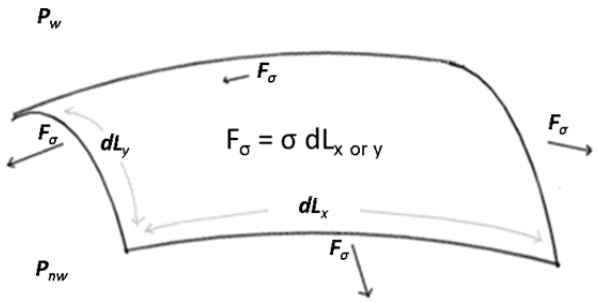

Figure 2.2: A small segment of a curved interface with area dA (i.e. $dA = dL_x dL_y$).

To explain the pressure discontinuity across the fluid-fluid interface, it is instructive to consider a small segment of a curved interface and to balance the pressures in each fluid phase and the interfacial forces (Figure 2.2). Assuming static equilibrium, the Young-Laplace equation can be derived

$$P_c = P_{nw} - P_w = (2\gamma)/R \tag{2.5}$$

where, γ is the interfacial tension (force per length) across the fluid-fluid interface, P_{nw} is the non-wetting phase pressure (force per area), P_w is the wetting phase pressure (force per area), P_c is the capillary pressure (force per area), and R is mean curvature (inverse length). *Eq. 2.5* directly links the mean curvature of an interface to the pressure discontinuity across the interface (see Chapter 3). This pressure difference is inherently a pore-scale phenomenon and is referred to as capillary pressure.

For the purpose of modeling multiphase flow, capillary pressure is often defined as a constitutive function of a macro-scale parameter (i.e. saturation)

$$P_{nw} - P_w = P_c\left(S_w\right) \tag{2.6}$$

where, S_w is the wetting phase saturation (fraction of void space occupied by the wetting phase). A graphical representation of this constitutive relationship is shown in Figure 2.3, where saturation decreases with increasing P_c (the pressure-saturation relationship is further explored in Chapter 3). However, two distinctly different curves exist. The upper curve represents the process of drainage, where a non-wetting fluid displaces a wetting fluid. Conversely, the lower curve represents the process of imbibition, where a wetting fluid displaces a non-wetting fluid. As evident in Figure 2.3, the relationship between capillary pressure and saturation is dependent on the systems history. The term hysteretic, which is the dependency of a current system's state on its past state, is often used to describe the capillary pressure saturation relationship. This hysteretic effect complicates the modeling of multiphase flow, since a system's history is often unknown.

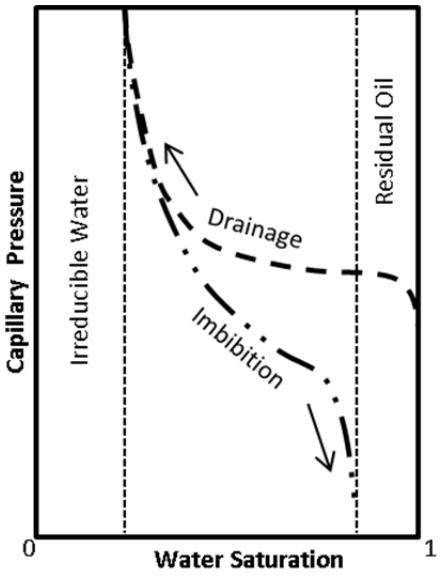

Figure 2.3: Capillary pressure versus water saturation curve.

To model multiphase flow through porous media, a macro-scale approach is taken, where fluid properties are considered continuous over a small volume of space. Using this continuum approach and assuming steady state conditions, Darcy's law, which was originally derived to describe the flow of a single fluid through a porous medium, can be extended to describe the flow of multiple immiscible phases

$$q_\alpha = \left(k_\alpha / \mu_\alpha\right) \left(\nabla P_\alpha - \rho_\alpha g\right) \tag{2.7}$$

where, q_α is the Darcy flux (length per time) of fluid phase α, k_α is the relative permeability (length squared) of fluid phase α, μ_α is the viscosity (force multiplied by time per length squared) of fluid phase α, ρ_α is the density (mass per volume) of phase α, g is the gravitational constant (length per time squared), and P_α is the pressure (force per area) in fluid phase α.

Relative permeability (as used in *Eq. 2.7*) depends on the structure of the porous medium involved, the overall permeability of the medium to a single fluid phase, and on the respective saturations of each fluid phase (Bear, 1988). Consequently, relative permeability is modeled as a constitutive function of saturation

$$k_\alpha = k_\alpha\left(S_w\right) \tag{2.8}$$

An example relative permeability saturation curve is provided in Figure 2.4, which demonstrates that as the permeability of a given phase increases the permeability of the other phase decreases. This seems natural, since if a given fluid phase occupies a given fraction in the pore-space, flow of the other immiscible phase is occluded from that region.

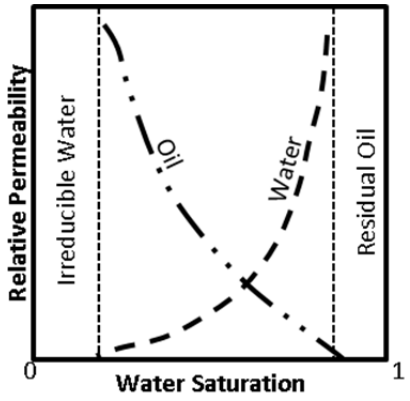

Figure 2.4: Oil-water relative permeability curve.

Lastly, the mass conservation equation for a multiphase system (assuming no sources or sinks) is

$$\frac{\partial\left(\eta \mathrm{S}_{\alpha}\rho_{\alpha}\right)}{\partial t} + \nabla\cdot\left(\rho_{\alpha}\mathrm{q}_{\alpha}\right) = 0 \qquad (2.9)$$

where, η is porosity (void space fraction), S_α is the saturation (fraction of void space occupied by a given phase) of phase α, and $\rho_\alpha q_\alpha$ is the mass flux (mass per unit area per time) of phase α. To construct a multiphase flow model that can be solved for pressure and saturation, *Eq. 2.7* must be substituted into *Eq. 2.9*.

$$\frac{\partial\left(\eta \mathrm{S}_{\alpha}\rho_{\alpha}\right)}{\partial t} - \nabla\cdot\left(\mathrm{P}_{\alpha}\frac{k_{\alpha}}{\mu_{\alpha}}\left(\nabla P_{\alpha} - \rho_{\alpha}\mathrm{g}\right)\right) = 0 \qquad (2.10)$$

To solve for the unknown parameters in *Eq. 2.10* (i.e. S_α and P_α), three additional equations are required. The simplest of the additional three equations is

$$\sum_{i=\alpha}^{n} S_{\alpha} = 1 \qquad (2.11)$$

simply stating that the fluid phases completely occupy the void space. The other two equations are the previously introduced constitutive relationships for capillary pressure (*Eq. 2.6)* and relative permeability (*Eq. 2.8*). Thus, through the utilization of *Eq. 2.6, Eq. 2.8*, *Eq. 2.10*, and *Eq. 2.11*, the temporal and spatial variation of pressure and saturation can be quantified for a particular multiphase system at the macro-scale.

2.2.2 Dynamic Imbibition

Dynamic imbibition, often called water flooding, is a common secondary oil recovery practice, where a wetting phase (often water) is used to displace oil. Imbibition initially occurs at relatively high P_c, during which the wetting phase preferentially invades only the smallest pore-space regions. As P_c is decreased, progressively larger pore-space regions become saturated. However, due to variations in pore morphology, contact angle, interfacial tension, fluid viscosity, and flow rate, imbibition often lacks efficiency and the non-wetting phase remains trapped in the pore-space once imbibition is complete. Water flooding is simulated in the experiments presented in Chapters 4, 5, and 6 by flooding oil saturated micromodels or columns until oil recovery ceases.

Water flooding inefficiency is explained by understanding the competition between viscous and capillary forces, which is critical since relative permeability, oil saturation (thus oil available for recovery) and oil blob morphology are directly dependent on the dominant force. To better understand this competition, Lenormand (1985) introduced the concept of a phase-diagram, where fluid displacement is characterized by two dimensionless numbers: capillary number and viscosity (or mobility) ratio. Capillary number is the ratio between viscous forces and capillary forces

$$N_{ca} = v\mu / \sigma \tag{2.12}$$

where, v is the velocity (length per time) of the displacing phase, μ is the viscosity (force multiplied by time per length squared) of the displacing phase, and σ the interfacial tension (force per length) between both phases. The viscosity ratio is the ratio between the viscosity of the displacing phase and the viscosity of the displaced phase

$$M = \mu_1 / \mu_2 \tag{2.13}$$

where, μ_1 is the viscosity of the displacing phase and μ_2 is the viscosity of the displaced phase. The phase-diagram approach allows for the prediction of one of three displacement types: (1) capillary fingering, (2) viscous fingering, or (3) stable displacement, and thus, is a useful method for characterizing fluid displacement.

In the capillary fingering regime viscous forces are negligible and capillary forces dominate. Capillary fingering occurs at relatively low flow rates, where (due to capillarity) the wetting phase flows through the crevices of the pore-space (i.e. the smallest regions or the pore-space and/or channels formed by surface roughness). Capillary fingering leads to non-uniform advancement of the displacement front, which is a rather inefficient displacement process. In the viscous fingering regime capillary forces are negligible and viscous forces dominate. Viscous fingering occurs at relatively high flow rates and when the displaced phase is more viscous than the displacing phase. Viscous fingering leads to the formation of tree-like fingers that extend out ahead of the displacement front, which is also a rather inefficient displacement process. During viscous fingering, once a finger is formed and extends out into the more viscous fluid it encounters a region of lower pressure and keeps moving forward, which further extends the finger length (Zhang et al. 2010). Conversely, stable displacement occurs at a relativity high flow rate and when the viscosity of the displacing phase is greater than the viscosity of the displaced phase. Stable displacement leads to a flat (i.e. stable) displacement front and low residual saturation (i.e. high displacement efficiency). During stable displacement if a finger starts to develop the finger tip would have a lower pressure than the main fluid font, and thus, the front would catch up (Zhang et al. 2010). For the experiments presented in Chapters 4, 5, and 6 the viscosity of the displaced phase is greater then the viscosity of the displacing phase. However, capillary number is relatively low ($\sim 10^{-7}$). Thus, either capillary fingering and/or viscous fingering are likely to occur during water flooding.

When capillary number is low (which often occurs during water flooding), sufficient time is allowed for the development of crevice flow and snap-off can occur. Snap-off was first characterized by Lenormand et al. (1983, 1984) and has recently been investigated by numerous researchers (e.g. Mahmud et al. 2006; Nguyen et al. 2006; Chang et al. 2009; Knackstedt et al. 2010). Crevice flow, as defined by Blunt and Scher (1995), is characterized as a thin film of wetting fluid that flows through the crevices of the pore-space. During imbibition, as capillary pressure decreases, the wetting film thickness increases. At a critical capillary pressure the wetting film becomes too thick, and thus unstable, in the smallest most restricted pore-space regions (i.e. the pore throats). This instability causes the wetting film interface to collapse, which forces the adjoining non-wetting phase into an adjacent pore body. Depending on the number of surrounding pores saturated with wetting phase, the non-wetting phase may become disconnected from the bulk connected non-wetting phase

and become trapped. The prevalence of capillary trapping in numerous pore morphologies is investigated in Chapter 6.

Numerous researchers have modeled imbibition (e.g. Li and Wardlaw 1986; Nguyen et al. 2006; Hughes and Blunt 2000). The pore network model constructed by Nguyen et al. (2006) explains the pore-scale competition between capillary fingering and stable displacement as a flow rate dependent process, resulting in rate dependent relative permeability curves and residual saturation. At low flow rates (i.e. low capillary number) wetting films are allowed sufficient time to advance ahead of the displacement front and swell, which leads to snap-off. While at high flow rates (i.e. high capillary number) snap-off is suppressed, since displacement time is inversely proportional to displacement rate, and thus, less time is allowed for film flow development. Similar network models that evaluate water flooding rate affects are presented by Blunt and Scher (1995) and Idowu and Blunt (2010). In both models the competition between viscous and capillary forces dictates displacement efficiency.

2.2.3 Capillary Desaturation

After water flooding, discontinuous capillary trapped oil blobs (also referred to as ganglia) often remain in the reservoir, due to displacement inefficiencies (Gray et al. 2008). These globules remain trapped until a force sufficient enough to move them through an adjacent pore neck is applied (Dullien, 1992). At this scale (i.e. the pore-scale) capillary forces largely control oil globule displacement.

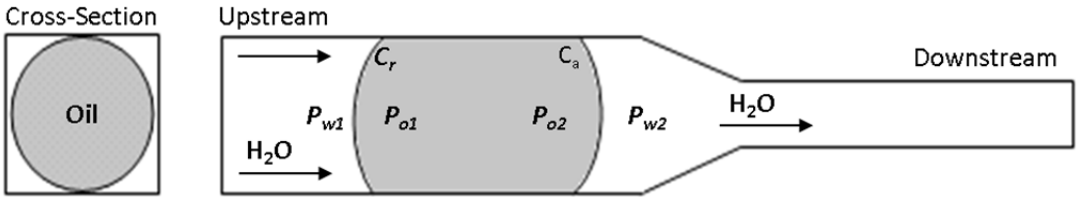

Figure 2.5: An oil droplet capillary trapped in a divergent square-shaped capillary tube.

A simple approach to modeling the displacement of a capillary trapped phase was presented by Kalaydjian and Legait (1987), where an isolated oil droplet is trapped in the upstream region of a divergent square-shaped capillary tube (Figure 2.5). If the flow rate in the surrounding water phase is large enough, the isolated oil droplet will migrate downstream and through the divergent region which is analogous to the movement of an oil droplet from a pore body through a pore neck. Flow in this situation can be envisaged as two separate events. One is of the advancing type, in which oil moves out of the original volume occupied by the droplet and the other is of the retreating type, in which water moves into the original volume occupied by the oil droplet. The advancing type occurs at the downstream interface (i.e. the low-pressure side) of the oil droplet and the retreating type occurs at the upstream interface (i.e. the high-pressure side). Due to the physical structure of the divergent capillary tube the curvature of the advancing interface (C_a) must increase during mobilization, which requires a steep water-phase pressure gradient.

The water-phase pressure drop needed to initialize mobilization is established by calculating the pressure differential across the upstream and downstream interface, using the Young-Laplace equation (*Eq.2.5*), and then balancing these pressures by subtracting the upstream and downstream pressure differentials

$$P_{w1} - P_{w2} = \gamma\left(C_a - C_r\right) \tag{2.14}$$

where, P_{w1} is the downstream water pressure (force per area), P_{w2} is the upstream water pressure, C_r is the curvature (inverse length) of the retreating interface, and C_a is the curvature of the advancing interface. Thus, the critical condition for ganglion mobilization is that the pressure drop from one end of an oil blob to the other, in the direction of flow, must exceed the capillary pressure difference between the interfaces at the upstream and downstream ends of the oil blob (Melrose and Brander, 1974). A method to measure interfacial curvature, and thus the capillary pressure of residual oil blobs is presented in Chapter 3.

Darcy's law (*Eq. 2.7*) can be used to relate the critical pressure gradient needed for oil mobilization to flowrate. For multiphase flow the relative permeability and viscosity for each phase must be considered. However, when the trapped phase is disconnected and is assumed to be a static boundary, only the single-phase application of Darcy's law is

necessary. As shown by De la Cruz and Spanos (1983), Darcy's law for a continuous phase only breaks down once mobilization of the discontinuous phase occurs. This approach only describes the pressure drop and corresponding flow rate needed to mobilize a trapped immiscible phase; once mobilization occurs, Darcy's law will not hold, and more sophisticated approaches must be used to model the system.

To better understand residual blob oil mobilization, it is convenient to consider the dependency of displacement on a dimensionless parameter, such as the capillary number (*Eq. 2.12*). The larger the capillary number, the less dominant capillary forces become and the greater the likelihood for oil mobilization (Gray et al. 2008). By examination of *Eq. 2.12* it is evident that either the invading phase velocity or viscosity must be increased or interfacial tension must be decreased to increase the capillary number. However, significantly increasing the viscosity or velocity of the invading phase is not practical since this would lead to prohibitively high pressures at the injection well. Alternatively, significantly low interfacial tension is achievable with the use of a biosurfactant and is one approach taken when using MEOR (e.g. Baviere, 1991; Lin et al. 1994a; Youssef et al. 2009).

2.3 Reservoir Characteristics

To characterize reservoir rock, pore-scale morphological parameters and surface wettability metrics are often used. Pore-scale images obtained with computed microtomography are often used to quantify morphological parameters. In terms of wettability, macro-scale indices are developed to characterize the bulk wetting nature of a sample. These morphological parameters and wettability indices are unique, reservoir specific properties that are critical for understanding the spatial arrangement and the mobilization of residual oil blobs, and thus, are explained in the following sections.

2.3.1 Pore Morphology

There is a strong relationship between the structural features (i.e. pore morphology) of a reservoir rock and its functional properties (i.e. hydraulic characteristics). The quantification of pore-structure and the correlation of morphological parameters to functional properties is a major challenge. Nonetheless, this challenge has been tackled by numerous researchers (e.g. Prodanović et al. 2005; Cai et al. 2009; Vogel et al. 2010), since understanding pore

morphology is critical to understanding multiphase flow. Numerous reports demonstrate that oil blob morphology and oil saturation, which ultimately affects oil blob mobilization, are directly dependent on pore morphology (Schnaar and Brusseau 2005; Schnaar and Brusseau 2006; Costanza-Robinson et al. 2008; Brusseau et al. 2009).

Table 2.1: Description of general pore morphology parameters obtained with 3DMA-ROCK.

Parameter	Description
effective pore radii	the radius of a sphere of equivalent volume
effective throat radii	the radius of a circle of equivalent area
coordination number	the number of throats connecting a pore
aspect ratio	effective throat radius divided by effective pore radius

To facilitate these efforts, 3DMA-ROCK (Lindquist 2002), a software package that analyzes 3-dimensional pore-scale images of porous media and divides the pore-space into individual pore bodies separated by pore throats, is often used to characterize porous media for multiphase and single-phase flow models (e.g. Prodanović et al. 2007; Cai et al. 2009; Joekar-Niasar 2010; see Appendix A). Pore-space quantification is accomplished by constructing a medial axis through the void space of a CMT pore-scale image, followed by searching the medial axis for regions of minimal surface cross-sectional area, which are then defined as throats (Figure 2.6). 3DMA-ROCK divides the pore-space into individual pore bodies separated by throats. The latter represent only a surface and do not have volume (see Chapter 6). Morphological parameters, such as, effective pore radii, effective throat radii, coordination number, and pore aspect ratio, are easily obtainable with 3DMA-ROCK (Table 2.1).

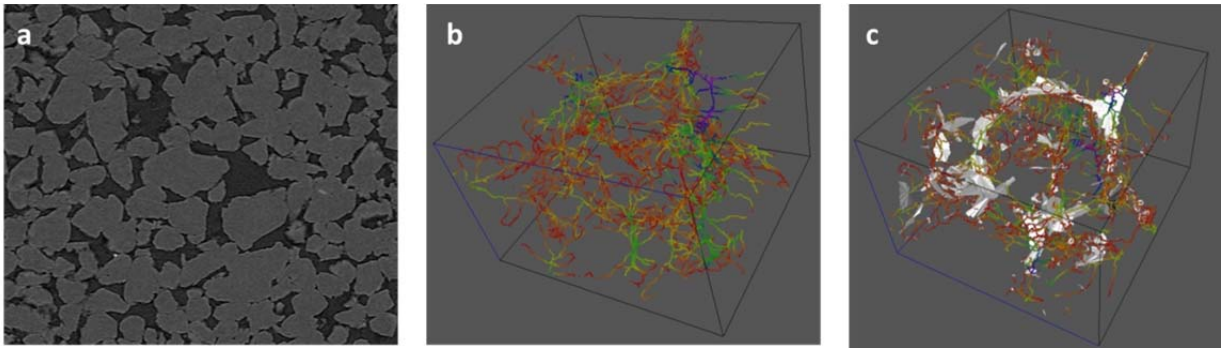

Figure 2.6: CMT image of a Bentheimer sandstone (a). Medial axis created from the pore-scale Bentheimer image (b). Pore-throats (white) identified along the medial axis (c).

2.3.2 Wettability

Wettability is a major factor controlling multi-phase flow, and thus oil production (Tweheyo et al. 1999; Graue et al. 1999; Morrow and Mason 2001; Al-Raoush 2009; Karpyn et al. 2010). To quantify porous media wettability, macro-scale indices (obtained with techniques such as the Carter, USBM, or Amott methods) are used regularly. The Carter method, as used by Kumar et al. (2008), initially calculates water-wet and oil-wet indices by measuring the relative amount of oil or water spontaneously imbibed into a porous sample. The Carter index is then calculated by subtracting the oil-wet index from the water-wet index. The Carter method values ranges from -1.0 to 1.0, where an oil-wet porous medium has a Carter index < 0, while a water-wet porous medium has a Carter index > 0. However, the Carter method and the other wettability metrics previously mentioned only provide macro-scale information.

The wettability of reservoir rock commonly ranges from water-wet to moderate-wet. Yet, in the case of carbonate reservoirs predominantly oil-wet conditions can exist (Treiber et al. 1971). Clean quartz sandstone is generally water-wet; however, if the same sandstone is subjected to high temperature and pressure in the presence of oil, its surface chemical structure can be altered or the surface itself can become coated (e.g. asphaltene deposition, Kumar and Fogden 2009) in such a way that it becomes oil-wet (Okasha et al. 2004; Afrapoli et al. 2010; Lake, 1996). Generally, most oil reservoirs have mixed-wettability due to either long term oil exposure at elevated temperature and pressure and/or the presence of non-quartz surfaces that are predominately oil-wet (e.g. calcite and dolomite, Okasha et al. 2004)

or moderate-wetting (e.g. kaolinite and montmorillonite, Borysenko et al. 2009). In this sense, mixed-wettability or fractional-wettability is used interchangeably since both terms refer to a situation where preferential wetting is spatially heterogeneous at the pore-scale. Herein, fractional wettability is defined as the fraction of pore surface area that is either water-wet or oil-wet (see Chapter 5). Thus, a fractional-wet porous media would have a given oil-wet surface area to water-wet surface area ratio.

2.4 Applied Microbiology

Microorganisms are ubiquitous in nature and numerous microbial species with diverse physiological and metabolic abilities are recovered from oil reservoirs (Youssef et al. 2009). Because of this diversity, MEOR must be implemented with great care, since both beneficial and detrimental microbial activities are possible. For example, when a reservoir's microbial community is stimulated with an abundant carbon source, and if sulfate is present, sulfate reducing bacteria may proliferate and produce large quantities of hydrogen sulfide, which is highly corrosive to oil-extraction equipment. However, numerous beneficial microbial mechanisms are also readily identifiable, for example, biosurfactant production or bioclogging. Currently, researchers are investigating oil reservoir microbial ecology and designing reservoir specific treatment regimes that aim to augment the microbial populations attributed to beneficial activity, while inhibiting those attributed to detrimental activity (e.g. Torsvik, 2005; Youssef et al. 2008; Bao et al. 2009; Zhang et al. 2010; van der Kraan et al. 2010), and thus, control the MEOR mechanisms through which residual oil blob mobilization occurs.

In general, fermentative and other anaerobic microbial populations dominate oil reservoir microbial communities, since oil reservoirs have low redox potentials, and thus, are predominately anoxic. To augment an oil reservoir's microbial community, an electron donor, an electron acceptor, or combination thereof, must be injected into the subsurface environment. Prior to reservoir augmentation, the most common electron donors found in an oil reservoir are: volatile fatty acids, acetate, propionate, benzoate and petroleum hydrocarbons, while the most common electron acceptors found in an oil reservoir are: sulfate, carbonate minerals, and iron (Fisher, 1987). Although the native chemical environment can obviously support microbial growth, MEOR requires a drastic increase in the microbial activity of a few specific beneficial microorganisms. Additionally, other environmental conditions, such as, high salinity, high temperature, and high pressure, must

be considered when implementing MEOR, especially if exogenous microorganisms are injected. Numerous reports have shown that microbial activity and significant hydrocarbon degradation does not occur in petroleum reservoirs that have been exposed to or are currently at temperatures greater than 80^{o}C (e.g. Röling et al. 2003; Wilhelms et al. 2001; Head et al. 2003). In the following sections the MEOR mechanisms attributed to oil mobilization and a few beneficial microbial species involved are reviewed.

2.4.1 MEOR Mechanisms

Numerous proposed mechanisms through which microorganisms increase oil recovery are presented in the literature (for an in depth review of each mechanism and the microbial species involved refer to Youssef et al. 2009) for the microorganisms used in this dissertation (i.e. *Bacillus mojavensis* JF-2 and *Shewanella oneidensis* MR-1) the following mechanisms are possible:

Interfacial tension reduction: Bacteria can facilitate the mobilization of oil through the production of amphiphilic compounds, termed biosurfactants, which reduce interfacial tension (IFT) between immiscible phases.

Wettability change: Bacteria can colonize reservoir rock and form biofilm that has wetting properties significantly different than reservoir rock, thus, a reservoir's wettability can change to a more water-wet or more oil-wet condition depending on the nature of the biofilm.

Bioclogging: The formation of biofilm can clog preferential flow paths and increase a reservoir's sweep efficiency.

Analyzing a successful laboratory-scale MEOR experiment is complicated by the fact that attributing *AOR* to a single mechanism is difficult because MEOR mechanisms do not necessarily occur independently. For example, during bioclogging, when sweep efficiency is increased, the formed biofilm could also potentially change surface wettability and/or increase pore velocity. Thus, to identify the MEOR mechanism responsible for oil recovery (which is the focus of Chapter 4), biofilm formation, wettability change, fluid viscosity change, and IFT reduction must be quantified. Emphasis should be placed on the fact that a combination of phenomena are responsible for oil recovery using MEOR and that multiple measurement techniques derived from the fields of microbiology and petroleum engineering are needed to understand MEOR.

2.4.2 Interfacial Tension Reduction

After secondary recovery, there is usually an insufficient pressure gradient to move residual oil blobs through the surrounding pore throats and a reduction of the capillary force that opposes oil blob movement is needed (Baviere, 1991). One strategy for oil blob mobilization is to increase the capillary number with a biosurfactant by reducing interfacial tension (Butt et al. 2006 and Lin et al. 1994a). Gray et al. (2008) reported on the minimal IFT reduction required for oil mobilization by rationalizing that a biosurfactant must reduce the IFT by at least two orders of magnitude to mobilize oil since the capillary number for most reservoirs under a water flood is 10^{-7} (Willhite and Green, 1998) and core flooding experiments indicate a capillary number of 10^{-5} to 10^{-4} is required to mobilize oil (Stalkup, 1984).

Oil blob mobilization due to biosurfactant-facilitated IFT reduction has been studied at the laboratory-scale under a wide range of circumstances. Suthar et al. (2008) used *Bacillus licheniformis* K125, *Bacillus mojavensis* JF-2, and *Bacillus licheniformis* TT42 in sand packed columns. K125 gave the best results with an *AOR* of 43%, JF-2 produced an *AOR* of 30%, and T42 was the least effective with an *AOR* of 21%. Soudman-asli et al. (2007) studied MEOR in fractured porous media using etched glass micromodels. In this study, a biosurfactant producing bacterium and an exopolymeric-producing bacterium were used; results suggested that plugging of the matrix-fractures by exopolymeric substances inhibited oil recovery resulting in the biosurfactant producing bacterium outperforming the exopolymeric producing bacterium. Yakimov et al. (1997) studied MEOR in oil-bearing sandstone cores with numerous *Bacillus licheniformis* species isolated from a German oil reservoir. In this study, oil recovery efficiencies varied from 9.3 to 22.1% *AOR*. While the reported *AOR* values look promising, attributing these positive lab-scale results to IFT reduction only is difficult. In some cases only *surface* tension (i.e. liquid phase/air interfacial tension) values for the microbial broth were reported (e.g. Suthar et al. 2009). In studies where actual IFT was reported, reduction does not always meet the two orders of magnitude requirement stated by Gray et al. (2008) suggesting that other mobilization mechanisms may be active and responsible for additional recovery.

2.4.3 Wettability Change

Changes in wettability can potentially increase oil recovery since both the spatial arrangement and morphology of residual oil is dependent upon wettability (Kumar et al. 2010b; 2009). As previously mentioned, bacteria can colonize surfaces and form biofilm, which can change a reservoir's wetting properties. Bacterial surface interactions have been reported to change preferential surface wetting properties from water-wet to oil-wet and vise versa (Polson et al. 2010; Chase et al. 1990; Kianipey, 1990). In MEOR studies using *Bacillus mojavensis* JF-2 in sandstone cores, bulk wettability shifted to more water-wet conditions. The Amot wettability index increased from -0.27 to -0.10 in initially oil-wet cores after MOER treatment with JF-2 (Chase et al. 1988) and the USBM wettability method in water-wet cores showed that JF-2 shifted the wettability index significantly in the positive direction toward a more water-wet condition up to a maximum index value of 0.99 (Kianipey et al. 1989). However, a reason for the direction in which microbes change surface wetting has not been proposed and a useful method for evaluating pore-scale surface wetting characteristics needs development such that a change in preferential wetting can be quantified and monitored at the pore-scale (i.e. grain surface) where the change originates.

2.4.4 Bioclogging

A biofilm is a surface-associated community of microorganisms. The biofilm matrix consists of exopolymeric substances (EPS; a mixture of polysaccharides, proteins, and other biological macromolecules) and microorganisms. Biofilms are observed in both natural and engineered systems, and are believed to be the primary habitat for most microorganisms (Costerton et al. 1995). In porous media, the accumulation of biofilm is known to reduce permeability and if this reduction occurs preferentially in high permeability zones, reservoir sweep efficiency during a water flood can potentially improve.

Numerous researchers have studied permeability reduction due to bioclogging (see Appendix B for the development of a method to image biofilm in porous media). Dunsmore et al. (2004) conducted permeability reduction experiments utilizing etched glass micromodels of 9900 md permeability intended to simulate reservoir sandstone. Biofilm production reduced permeability by 50% in the initial 25 hours and this reduction was attributed to cell aggregation and biofilm formation that clogged pore throats and restricted fluid flow. Cunningham et al. (1991) conducted permeability reduction experiments with *Pseudomonas*

aeruginosa in sand and glass bead columns. A 98% permeability reduction was observed over the first 2-3 day period and no further reduction was observed after 5 days. Permeability reduction was also measured in Prudhoe Bay cores by His et al. (1994). A total permeability reduction of 90% was observed and could be reversed by a 5-6% sodium hypochlorite injection which oxidized the bacteria and removed surface attached biofilm. Bioaccumulation in layered permeability zones was studied by Gandler et al. (2006) where columns were layered along their axes with different diameter glass beads. The results showed that bioaccumulation occurred preferentially in the higher permeability layer. Oil recovery experiments were not carried out by Gandler et al. (2006), however, selective plugging was evaluated by Suthar et al. (2009) in sand packed columns where no layered permeability zone existed and an average *AOR* of 28% was obtained.

Schulenburg et al. (2009) performed three-dimensional simulations of biofilm growth in porous media based on a Lattice Boltzmann simulation platform complemented with an individual based biofilm model. These simulations suggest some interesting subtleties of biofilm growth in porous media that are of particular importance to MEOR. Results suggest that biofilm accumulation: (1) increases both the heterogeneity and magnitude of the velocity field, (2) reduces the bulk liquid pore volume, (3) is encouraged in high velocity channels and consequently flow rate through these channels are reduced due to enhanced biofilm accumulation, and (4) in small amounts has a significant influence on permeability. Overall the simulations demonstrated that biofilm/biomass is a potentially effective medium for reducing permeability in relatively heterogeneous porous media.

2.5 Pore-Scale Imaging

Computed microtomography (CMT) and stereo microscopy are two imaging techniques that can provide significant pore-scale information. Computed microtomography can produce three-dimensional images of multiple fluid phases in a porous medium. However, using CMT, biological material that is relatively similar to water in terms of x-ray attenuation characteristics, is not detectable (Appendix B). Thus, to visualize the pore-scale MEOR mechanism of bioclogging, 2-dimensional micromodel experiments, where the biological phase can be directly visualized with stereo microscopy are required. Once images are collected, great care must be taken to extract quantitative information and a significant amount of research has gone into the subtleties of image processing. In the following

sections, computed microtomography and stereo microscopy will be introduced along with a brief introduction to image processing.

2.5.1 Computed Microtomography

Three-dimensional computed microtomography (CMT) has been available for more than three decades and has been a powerful tool for studying a wide array of processes in porous media systems (e.g. Al-Raoush et al. 2009; Wildenschild et al. 2002, 2005; Porter et al. 2010b; Appendices A and B). This imaging technique provides non-destructive and non-invasive 3-dimensional imaging of the interior of objects by mapping x-ray attenuation through a sample. The resulting attenuation values are represented in images as voxels (i.e. the 3-dimensional equivalent of a pixel) which are ultimately labeled as a given phase; for example, oil, water, and solid. The method allows for distinguishing multiple fluid/menisci, quantifying interfacial areas, and measuring oil blob size distributions (e.g. Al-Raoush et al. 2002; 2005; Karpyn et al. 2010). CMT is used in the experiments presented in Chapters 3, 5, and 6.

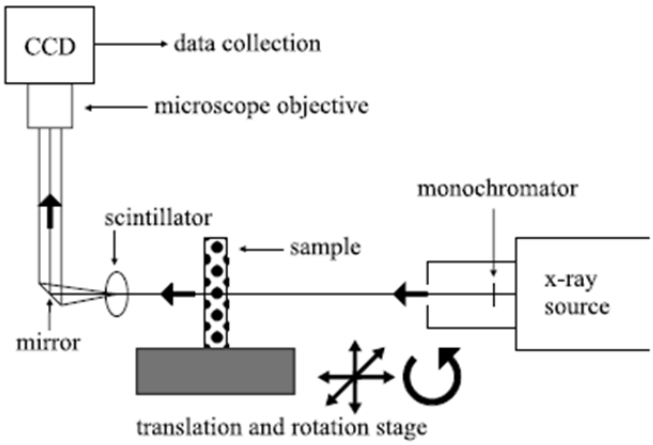

Figure 2.7: Typical computed microtomography (CMT) stage setup.

To further explain CMT, the tomography setup (Figure 2.7) at the Advanced Photon Source at Argonne National Laboratory will be used as an example. The GeoSoilEnviroCARS bending magnet beam-line provides a fan-beam of high-brilliance radiation, collimated to a parallel beam with a vertical beam size of approximately 5 mm. A monochromator is used to decompose the white synchrotron light into different wavelengths allowing a user to customize the monochromatic energy level at which to scan. For a three phase system (e.g.

water, oil, and solid) a tracer, such as cesium or iodine, is added to the water phase and scanning above the photoelectric edge of the tracer is performed to enhance contrast between the immiscible phases. Three-dimensional images result from scanning the sample through 180^{o} rotations in small angular increments (e.g. 0.25^{o}). The raw data (2D projections for each angle) are then reconstructed with a filtered back-projection algorithm using the programming language IDL™ (Research Systems Inc.) to form a 3-dimensional volume of gray-scale data. A voxel length of 10 µm can be easily achieved for a sample size of approximately 1 cm outer diameter.

Cone-beam microtomography was used in the experiments presented in Chapter 6. The general principles behind cone-beam microtomography and synchrotron-based CMT, as explained above, are the same. Tracers, as used in synchrotron-based CMT to enhance image contrast, are also used in cone-beam microtomography. However, imaging at the photoelectric edge of a tracer is not possible since cone-beam microtomography uses a polychromatic energy source. Though, a tracer, such as cesium or iodine, can still provide additional contrast between the immiscible phases then if no tracer is used.

2.5.2 Stereo Microscopy

A stereo microscope is an optical microscope variant designed for low magnification observation of a sample using incident light illumination and is used for the experiments presented in Chapter 4. This imaging technique allows for a greater depth of field and larger working distance than does use of a standard microscope. These attributes lend themselves nicely to micromodel experiments where the entire flow field (approximately 2.5 mm by 1.5 mm for most micromodels) needs to be imaged at moderate resolution (~10 µm/pixel). Imaging of micromodel multiphase flow experiments using stereo microscope allows for the quantification of interfacial curvature, residual oil saturation, and oil blob morphology (Chen et al. 2007; Cheng et al. 2004). One unique benefit to stereo microscopy is that imaging of biofilm/bioaccumulation in a micromodel is feasible, which makes this experimental approach an essential supplement to column experiments imaged with CMT.

2.5.2 Image Processing

The purpose of image processing is to prepare images for the extraction of quantitative information. This requires that features (or different phases, e.g. oil, water, and solid) are well defined, either by edges or unique intensities. The image processing steps of segmentation where individual phases are identified and labeled followed by quantification of interfacial area, oil blob morphology, and the development of a method to measure interfacial curvature are explained in the following.

The segmentation of gray-scale images is a critical step prior to extracting any quantitative information. Throughout the literature a multitude of different segmentation approaches are presented, for example; global threshold segmentation, indicator kriging-based segmentation, k-means segmentation, and gradient-based watershed segmentation (e.g. Porter and Wildenschild 2010, Schnaar and Brusseau 2006, Lindquist and Venkatarangan 1999). Global thresholding (used in Chapter 4) is the simplest approach; however, it is the most susceptible to error. Applying global thresholding, a user defined threshold value is set and any voxel value above the threshold is assigned to a given phase and any voxel value below the threshold is assigned to the other phase. Indicator kriging-based segmentation (used in Chapter 6) on the other hand uses a local thresholding approach, where known regions are defined by assigning upper and lower threshold values. The unknown regions (i.e. voxel values between the two threshold limits) are then assigned to a given phase by a local kriging-based correlation function (Lindquist 2002). Using K-means segmentation (used in Chapter 3), no user defined threshold values are used. K-means works by maximizing the difference in voxel values between different clusters, while minimizing the difference in voxel values in the same cluster (Pappas, 1992).

Image segmentation is often difficult in phase transition regions (e.g. the oil/water interface). At interfaces, large voxel intensity gradients exist and a simple threshold or local correlation function, such as indicator kriging or k-means, often place the location of an interface improperly or incorrectly identify the interface as a third phase (Sheppard et al. 2004). Using a gradient-based watershed segmentation (used in Chapter 5) the known regions (i.e. internal regions of each phase) in an image are identified with a simple threshold and then the unknown regions (i.e. interfacial transition regions) are found by considering the image intensity gradient, such that, the optimal transient between any two phases is found at the

inflection point between any two known phases (Sheppard et al. 2004). This point of inflection is identified by the maximum of the first derivative of the image intensity.

After segmentation, bulk residual oil saturation and oil blob morphological parameters can be calculated. Oil saturation is simply found by counting the number of voxels in an image that belong to the oil phase. Individual oil blob sizes are calculated by finding connected components in a binary residual oil image using neighborhood pixel connectivity (for example, 8 for 2-dimensional images or 26 for 3-dimensional images). Each connected object is classified as an oil blob and volumes are reported as the number of pixels (or voxels for a 3-dimensional image) representing a given blob.

Additionally, after image segmentation, a marching cube algorithm can be implemented to construct isosurfaces between the fluid-fluid interfaces. For example, Porter et al. (2010) used the isosurfaces from segmented images to calculate interfacial areas (e.g. oil/water, oil/solid, and water/solid) in a multiphase system, and validated this method by using a number of test images that resulted in interfacial area estimates within 2-10% of the true value. In this dissertation, a similar approach is taken to develop and validate the measurement of interfacial curvature, which is an essential multiphase flow parameter (see, *Eq. 2.5* and *Eq. 2.14*), from pore-scale images.

The curvature of a surface (e.g. an interface or isosurface) is a unique surface characteristic that defines the amount by which a surface deviates from being flat. At any given point C on a surface S the curvature κ changes as the normal plane $R_n(\phi)$ rotates around the normal vector n (Figure 2.8). Thus, curvature $\kappa_n(\phi)$ at C is a continuous function and has both a maximum and a minimum defined as the two principal curvatures κ_1 and κ_2 , where the mean value of the principal curvatures is R, as defined in *Eq. 2.5*. Depending on whether the segmented images are 2-dimensional or 3-dimensional two different curvature measurement techniques were applied.

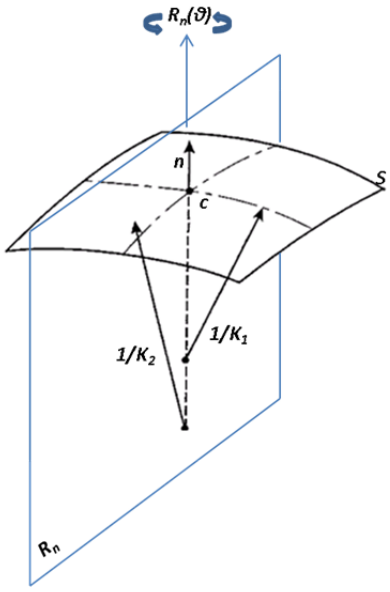

Figure 2.8: Curvature measured at point C on surface S. The surface is uniquely defined by the two principals of curvature K_1 and K_2.

In Chapter 4, for the 2-dimensional stereo microscopy images, interfacial curvature was calculated using level set methods adapted from work presented by Sethian (1996 and Sethian and Smereka, 2003). Level set methods are numerical techniques for analyzing interfaces and interfacial movement. Intrinsic geometric properties of a front (i.e. an interface) are easily determined from the level set function φ. For example, the curvature (K) of each level set is easily obtained from the divergence of the unit vector normal to a front.

$$\mathrm{K} = \nabla \cdot \left[\nabla\varphi / |\nabla\varphi| \right] = \left[\varphi_{xx}\varphi_y^{\,2} - 2\,\varphi_x\varphi_y\varphi_{xy} + \varphi_{yy}\varphi_x^{\,2} \right] / \left[\varphi_x^{\,2} + \varphi_y^{\,2} \right]^{3/2} \qquad (2.15)$$

To implement this method, a segmented binary image is used and the edge of each interface is defined as a front. After applying a Gaussian blur function to the image, the resulting image can be defined as the level set function φ. If the location of each interfacial pixel is registered prior to blurring, the interfacial curvature at each registered point (i.e. pixel) is calculated using *Eq. 2.15*. Thus, the curvature value for all interfacial pixels in a 2-dimensional image can be calculated.

In Chapters 3 and 5, for the 3-dimensional CMT images, interfacial curvature was calculated using the commercially available software Avizo Fire® using the isosurfaces formed between the fluid-fluid interfaces. Isosurface patches between different phases (e.g. the oil and water phase) can then be extracted from the image volume and used for calculating interfacial curvature. Curvature is approximated locally on the triangulated isosurface by a quadratic form. The eigenvalues and eigenvectors of the quadratic form correspond to the principal curvature values and to the directions of principal curvature. From this analysis, a surface scalar field is computed containing the mean value of the two principal curvature values, which is mean curvature as used in the Young-Laplace equation (*Eq. 2.5*). Thus, capillary pressure can be directly measured from CMT images.

2.6 Summary

In the following Chapters the concepts, mechanisms, and approaches described here are implemented to explore MEOR. Chapter 3 validates a method to measure interfacial curvature from CMT data. Chapter 4 explores the MEOR mechanisms previously presented and attempts to decouple the mechanisms. Chapter 5 uses the curvature method presented in Chapter 3 to investigate oil blob mobilization (i.e. capillary desaturation) with MEOR in fractional-wet systems. Lastly, Chapter 6 examines pore morphology effects on capillary trapping (i.e. snap-off) and oil blob mobilization with MEOR.

Chapter 3. Linking Pore-Scale Interfacial Curvature to Column-Scale Capillary Pressure

Ryan T. Armstrong[1], Mark L. Porter[2] and Dorthe Wildenschild[1]

1. School of Chemical, Biological, and Environmental Engineering, Oregon State University, 103 Gleeson Hall, Corvallis, OR 97331-2702

2. Los Alamos National Laboratory, Earth and Environmental Sciences Division, Los Alamos, NM 87545

Advances in Water Resources
211 Mission Street, 26th floor, San Francisco, CA 94105
Submitted 12/12/2011

3.1 Abstract

Synchrotron-based tomographic datasets of oil-water drainage and imbibition cycles have been analyzed to quantify phase saturations and interfacial curvature, as well as, connected and disconnected fluid configurations. This allows for close observation of the drainage and imbibition processes, assessment of equilibrium states, and studying the effects of fluid phase disconnection and reconnection on the resulting capillary pressures and interfacial curvatures. Based on this analysis estimates of capillary pressure (P_c) calculated from interfacial curvature can be compared to P_c measured externally with a transducer. Results show good agreement between curvature-based and transducer-based measurements, when connected phase interfaces are considered. Curvature measurements show a strong dependence on whether an interface is formed by connected or disconnected fluid and the time allowed for equilibration. The favorable agreement between curvature-based and transducer-based P_c measurements shows promise for the use of image-based estimates of P_c for interfaces that cannot be probed with external transducers, as well as opportunities for a detailed assessment of interfacial curvature during drainage and imbibition.

3.2 Introduction

The relationship between capillary pressure and saturation is the foundation on which we build our multiphase flow models and our understanding of the relevant pore-scale physics. Thus, the importance of this relationship cannot be overstated. Capillary pressure (P_c) is inherently a pore-scale phenomenon and is defined as the difference in pressure across a curved interface separating two immiscible fluids, expressed as

$$P_c = P_{nw} - P_w \tag{3.1}$$

where P_{nw} is the non-wetting phase pressure and P_w is the wetting phase pressure (wetting and non-wetting phases are defined below). In a multiphase system, P_c is attributable to the interfacial forces that act tangential to the interfacial boundaries. By considering a small segment of a curved interface, balancing pressure and interfacial forces, and assuming static equilibrium, the Young-Laplace equation can be written as

$$P_c = 2\sigma R \tag{3.2}$$

where σ is the interfacial tension between the wetting and the non-wetting phase and R is mean curvature. Using *Eq. 3.2* the mean curvature of an interface can be directly linked to

capillary pressure. For example, if applying *Eq.3. 2* to a simple capillary tube geometry *R* is defined as

$$R = cos(\alpha) / r \tag{3.3}$$

where α is the contact angle (measured as the angle between the fluid-fluid interface and the solid surface) and *r* is the radius of the capillary tube. When measuring α through a given phase, the phase is considered wetting for $\alpha < 90^{o}$ and non-wetting for $\alpha > 90^{o}$. However, for more complex systems the combined effect of contact angle and pore morphology on *R* is not easily defined and direct measurement of *R* is usually unfeasible for opaque media.

Traditionally, P_c is defined at the macro-scale by the following empirical relationship

$$P_{nw} - P_w = P_c\left(S_w\right) \tag{3.4}$$

where S_w is wetting phase saturation. This traditional approach assumes that capillary pressure is a function of saturation only, and other pore-scale properties, such as interfacial configuration, interfacial curvature, contact angle, and pore morphology are ignored. The previously mentioned properties tend to be lumped into S_w without consideration of their individual effects. Additionally, this traditional relationship produces a non-unique solution because of hysteretic effects, in part, due to oversimplification of the pore scale physics resulting in a non-unique solution during drainage and imbibition.

Even though hysteresis complicates the application of *Eq. 3.4*, the traditional function does result in a range of possible static P_c values that are enclosed by the main imbibition and main drainage branches for all possible saturation histories within a given sample (Leverett, 1940). In this respect, since P_c can be directly related to mean curvature (i.e., *Eq. 3.2*), all possible static interfacial geometries (i.e. mean curvatures) in a given sample are restricted by the main imbibition and drainage branches. Thus, fundamentally, only a unique range of mean curvatures are possible for a given sample. However, understanding the independent effect of interfacial tension, contact angle, and pore morphology on interfacial curvature is difficult.

Using a thermodynamic approach, Hassanizadeh and Gray (1990, 1993) and Gray and Hassanizadeh (1991a, 1991b) and more recently Gray and Miller (2011) stressed the importance of including interfacial properties when modeling multiphase flow at the macro-scale. The general concept in their approach has been to develop a model that explicitly accounts for the interfaces in a multiphase system. They propose that the traditional macroscale $P_c(S_w)$ function does not fully account for all of the pore scale physics and that an additional term, specific interfacial area (a_{nw}), is needed (Hassanizadeh and Gray, 1990, 1993; Gray and Miller, 2011). The following functional relationship for capillary pressure was proposed

$$P_c = P_c\left(S_w,\ a_{nw}\right) \tag{3.5}$$

With the inclusion of a_{nw} in the macro-scale capillary pressure relationship, Hassanizadeh and Gray (1993) hypothesized that all possible static P_c values lie on a unique surface and that the hysteretic effect seen with *Eq. 3.4* is simply an artifact of projecting a 3D surface onto the P_c-S_w plane. A few experimental and numerous modeling results have shown that a unique P_c-S_w-a_{nw} surface exists for a given pore morphology, suggesting that the inclusion of a_{nw} provides a unique solution for P_c, or at least removes most of the hysteretic effect (Reeves and Celia 1996; Held and Celia 2001; Cheng et al. 2004; Joekar-Niasar et al. 2008; Porter et al. 2009, 2010). However, pore network modeling results from Helland and Skjaeveland (2007) show non-unique solutions for P_c (in reference to *Eq. 3.5*) and results from Liu et al. (2011) suggest that a_{nw} is dependent on contact angle, and thus, is not an independent variable (as defined in *Eq. 3.5*). Regardless, saturation, specific interfacial area, and contact angle hysteresis are important parameters to consider and numerous reports have demonstrated their influence on interfacial curvature.

More recently, the difference between dynamic and static P_c has been studied, and it is well accepted that these value are not identical (Hassanizadeh et al. 2002; Manthey et al. 2008; O'Carroll et al. 2005, 2010). This dynamic effect is attributed to the rate of change of saturation. However, herein we address an additional dynamic effect due to interfacial relaxation. Very little experimental evidence has been presented that addresses the relaxation of interfaces during the transition from dynamic to static conditions. Despite the fact that such experimental evidence is requisite for assessing the time needed for equilibration, and thus, the circumstances required to warrant use of an equilibrium assumption. To our knowledge, the only experiments that address equilibration are

presented in the work of Liu et al. (2011), who reported relaxation times of 165 minutes for the radius of interfacial curvature in a smooth-walled divergent channel.

Our approach to quantifying capillary pressure evolution is to investigate interfacial curvature measured from computed x-ray microtomography (CMT) images obtained during imbibition and drainage experiments. In the collected images, fluids were separated into four individual fluid configurations: (1) connected wetting, (2) disconnected wetting, (3) connected non-wetting, and (4) disconnected non-wetting. The average interfacial curvature between each fluid combination was compared to P_c values measured from an external pressure transducer. Curvature measured from the CMT images was then related to capillary pressure using the Young-Laplace equation (*Eq. 3.2*). This approach allows for a direct comparison between P_c calculated from a pore-scale interfacial property (i.e. curvature) and column-scale P_c measured using a pressure transducer.

Pragmatically, the two pressure measurement approaches are different. A pressure transducer evaluates P_c according to *Eq. 3.1*, where P_{nw} is generally measured at the column outlet using a hydrophobic membrane, and P_w is generally measured at the column inlet using a hydrophilic membrane. The disadvantage to this measurement technique is that P_c is not related to any sort of interfacial property and S_w is averaged over the whole column assuming saturation gradients are small. Conversely, P_c calculated from curvature using the Young-Laplace equation (*Eq. 3.2*) directly considers an "intrinsic" interfacial property, i.e., curvature (Hassanizadeh and Gray, 1993). This distinction is crucial, because it is unclear how pressure transducer-based P_c measurements account for disconnected fluid interfaces and how the transducer averages P_c over the entire column. In essence, an external pressure (transducer) measurement is some volume averaged value and, in our opinion, it is critical to understand how well this value represents pore-scale interfacial curvature. Assuming that the error associated with the measurement of interfacial curvature can be minimized, it is our proposition that measuring interfacial curvature from pore-scale images can provide significant improvement in the evaluation of pore-scale capillary pressure.

To the best of our knowledge, this is the first direct comparison between micro-scale P_c measured via interfacial curvature and macro-scale P_c measured via a pressure transducer in a 3D porous medium. A few attempts have been made using other imaging techniques in 2D

micromodels. Cheng et al. (2004) and Pyrak-Nolte et al. (2008) measured interfacial curvature in 2D from microscope images using a level set approach and found a reasonable correlation between transducer measured P_c and curvature measured P_c. Additionally, Liu et al. (2011) measured interfacial curvature from confocal laser scanning microscopy images by fitting the interfaces to the arc of a circle. Ultimately, the accuracy of a given curvature measurement depends on the quality of the original image, where both image resolution and the signal-to-noise ratio are critical. Herein, we validate our curvature measurement method by testing it against CMT images of precision glass spheres and CMT images of capillary tube menisci, and lastly, we compare pore-scale interfacial curvature measurements to column-scale capillary pressure measurements during drainage and imbibition.

3.3 Materials and Methods

3.3.1 Experimental Setup

In this work, we further analyze CMT data for the drainage and imbibition experiments reported by Porter et al. (2010). These experiments were conducted at the GeoSoilEnviro Consortium for Advanced Radiation Sources (GSECARS) bending magnetic beamline, Sector 13, Advanced Photon Source (APS), Argonne National Laboratory. The experimental system consisted of soda-lime glass beads (35% 0.6 mm diameter, 35% 0.8 mm diameter, and 30% 1.0-1.4 mm diameter) packed in a 25.0 mm long glass column with an inside diameter of 7.0 mm. A semi-permeable, hydrophilic membrane was placed at the bottom of the column to prevent the non-wetting phase (Soltrol 220, ρ = 0.79 g/cm^3, σ = 0.0378 N/m) from entering the water line. A rubber stopper containing the non-wetting phase outlet line was placed inside the column in contact with the top of the porous medium. The wetting phase consisted of potassium iodide doped water (1:6 mass ratio of KI:H_2O) and the amount of wetting phase pumped in and out of the column was precisely controlled ($\pm$ 1 μl) by a syringe pump (Gilson 402). In the present work, where the focus is on minute details, i.e., local curvature-based estimates of P_c, the saturation values are based on the imaged sub-section analyzed for curvature, whereas in Porter et al. (2010) the saturations were estimates for the entire column and thus based on the pumped volumes. The pressure of each phase was measured (Validyne P55 Differential Pressure Transducer) in the fluid lines above and below the porous medium. A point on the P_c-S_w curve was obtained by pumping a precise amount of wetting phase into (imbibition) or out of (drainage) the column at a flow rate of 0.6 ml/hr, turning off the pump, allowing the fluids to equilibrate for 10-15 minutes, and then imaging a

5.5 mm section of the column at 13 μm/pixel resolution. In a few cases fluid movement was observed in the CMT images (noticeable by the blurring and/or streaking of the reconstructed image) after 10-15 minutes and the system was allowed to equilibrate until no fluid movement was observed. Thus, it was assumed that the points on the P_c-S_w curve had reached near-equilibrium conditions. The column was initially fully saturated with the wetting phase and primary drainage (PD), main imbibition (MI), main drainage (MD), secondary imbibition (SD), and secondary drainage (SD) curves were measured in succession.

3.3.2 Image Segmentation

The reconstructed gray-scale CMT images obtained from the APS require further image processing to accurately identify the solid and two fluid phases. Typically, the images are filtered to remove random noise in the images, and then segmented so that each phase is identified by a single integer. The segmented data was first filtered with an edge preserving anisotropic diffusion filter and then segmented with a k-means clustering algorithm. Further details regarding the segmentation algorithm and its validation can be found in Porter and Wildenschild (2010a).

Representative elementary volume (REV) analysis for S_w and a_{nw} was conducted (Porter et al. 2010, Fig. 3) to ensure that the size of the image cube analyzed (128.6 mm^3) provides meaningful results when volume averaged. However, interfacial curvatures were not considered in Porter et al. 2010, and thus further REV qualification is included in this report. To resolve this issue a larger cylindrical volume (194.7 mm^3) was extracted from the segmented data and analyzed for curvature. The larger cylindrical volume gave nearly identical curvature results to that measured from the smaller cubed volume (Figure 3.1). Thus, for simplicity in data processing (less memory and CPU required), the smaller cubed data volume (128.6 mm^3), as used on Porter et al. 2010, was used for the analyses presented herein.

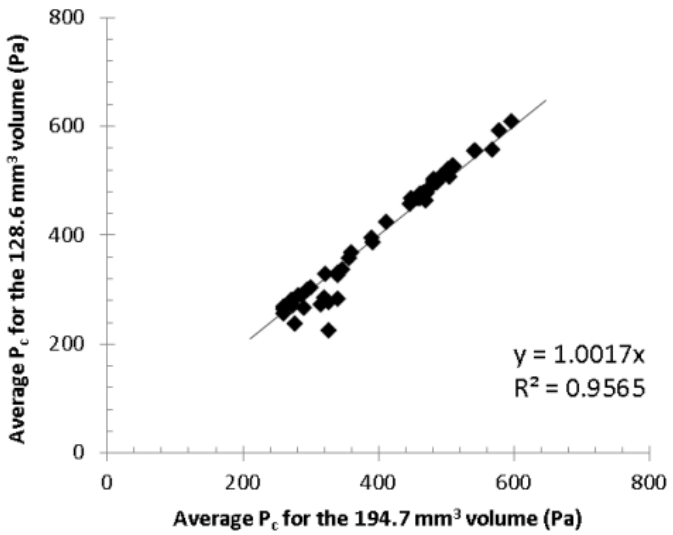

Figure 3.1: The average Pc values calculated from the cubed volume (128.6 mm3) and a larger cylindrical volume (194.7 mm3) are directly comparable, demonstrating that an REV, in terms of interfacial curvature, was obtained with the smaller cubed volume.

3.3.3 Image Analysis: Connectivity

Segmented images were analyzed for connectivity throughout the assigned REV. An algorithm in Avizo Fire® called Reconstruct was used to rebuild an image starting from markers placed at the top and bottom of the segmented volume. The algorithm exclusively retrieves objects in the image space that are connected to the set markers, using a 26 neighborhood voxel-connectivity requirement (see Avizo Fire® documentation for more information). To reflect the experimental setup, a marker for the oil phase was placed at the top REV slice and a marker for the water phase was placed at the bottom REV slice. Thus, any oil phase voxel connected to the top slice was retrieved and considered to be connected. Likewise, any water phase voxel connected to the bottom slice was retrieved and considered to be connected. Using this approach the assigned REV was segregated into four fluid configurations: (1) connected wetting, (2) disconnected wetting, (3) connected non-wetting, and (4) disconnected non-wetting.

3.3.4 Image Analysis: Interfacial Curvature

The first step of the curvature calculation process was to construct isosurfaces from the segmented images. Isosurfaces were generated between the following fluid configurations:

connected wetting/connected non-wetting, connected wetting / disconnected non-wetting, and disconnected wetting/connected non-wetting, using a surface generating marching cube algorithm in Avizo Fire®. The surfaces are smoothed using a 4x4x4 kernel applying sub-voxel weights such that the surface is naturally smoothed. However, no labels are modified, meaning that any two voxel centers that were labeled differently prior to smoothing remain separated by the generated surface afterwards.

Curvature was approximated locally on the triangulated interfacial surface by a quadratic form. The eigenvalues and eigenvectors of the quadratic form correspond to the principal curvature values and to the directions of principal curvature, respectively. This produces a surface scalar field that contains the mean value of the two principal curvature values, i.e., mean curvature (R), as used in *Eq. 3.2*. To smooth the curvature distribution data, mean curvature values that corresponded to adjacent triangular elements were averaged over a common neighborhood. Only triangles sharing a common edge and/or corner are considered common neighbors. The curvature estimation method was tested on artificial CMT data for a meniscus in a capillary tube, real CMT data for a meniscus in a capillary tube, and CMT images of precision glass spheres (0.8 mm ± 0.1 mm).

The artificial CMT capillary meniscus data were generated with a code[1] written in C++ that uses the analytical expression for a curved meniscus in a capillary tube to generate a 3D single-precision floating point array that represents a realistic geometry. The input parameters are: capillary tube diameter, curvature, amplitude of the Gaussian noise signal, and number of pixels in the x, y, and z directions. The artificial data were generated to have similar phase separation and noise as the actual CMT images collected during our experiments, and this was accomplished primarily by adjusting the Gaussian noise signal. Example histograms of both artificial and real CMT data are provided in Figure 3.2. Curvature was constrained by a 25^{o} contact angle. The contact angle was evaluated experimentally by placing a droplet of Soltrol oil on a glass slide submerged in water. The resulting contact angle was computed using ImageJ based on B-spline active contours (Stadler et al. 2006). Lastly, this algorithm allowed us to vary the capillary tube radius to represent the range of P_c values measured during the drainage and imbibition experiments.

[1] Courtesy of James McClure (University of North Carolina).

Capillary meniscus data was also generated experimentally by placing a capillary tube in a (sealed) water reservoir, letting KI-doped water rise in the tube, allowing for equilibrium, and then imaging with CMT. Mean curvature (*R*) was calculated from the CMT image and compared to the analytical solution (*Eq. 3.3*). A third additional validation was performed by measuring curvature on a CMT image of precision glass spheres (0.8 mm ± 0.1 mm).

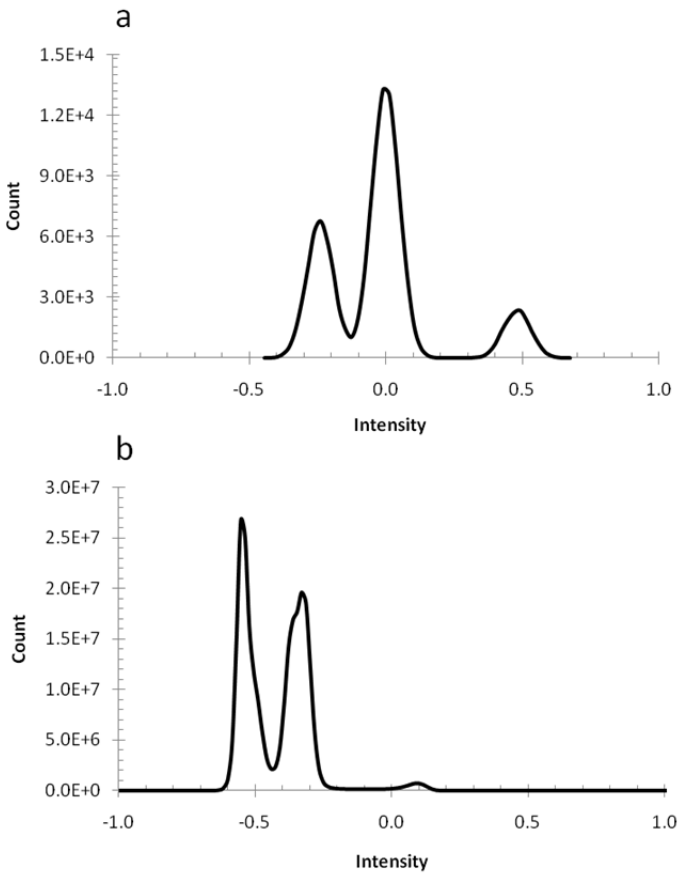

Figure 3.2: The Image histograms for the artificial (a) and real (b) CMT data are similar in terms of phase separation and noise.

3.4 Results and Discussion

3.4.1 Curvature Validation

The artificial CMT capillary meniscus data were generated to represent the range of P_c values encountered during the drainage and imbibition experiments. Figure 3.3 shows the relative

error encountered using this approach for the range of P_c values analyzed, and demonstrates that as P_c increases, error increases. This trend is essentially a resolution problem caused by pixilation (i.e. the pattern of pixels or voxels is visible due to low image resolution). As P_c increases, the capillary tube radius decreases, and thus, the number of pixels representing an interface decreases and error is accrued.

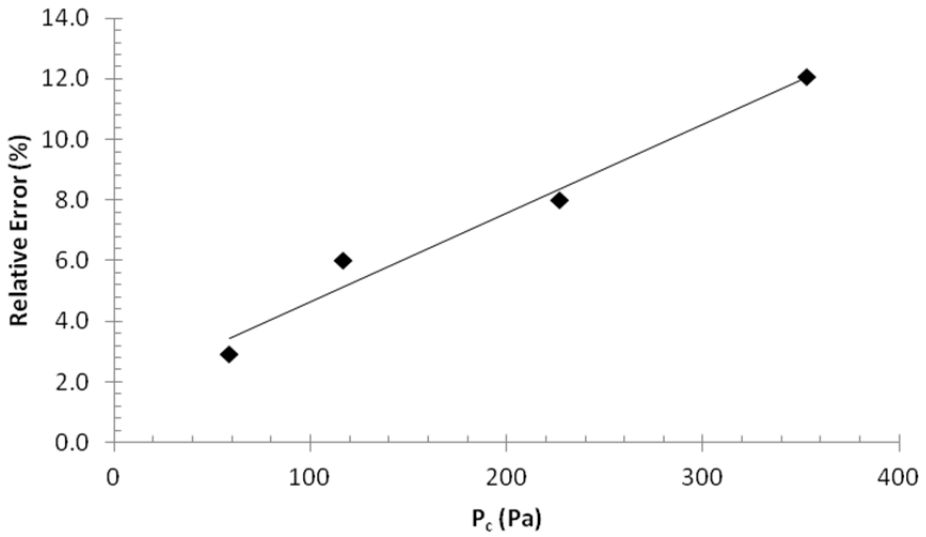

Figure 3.3: Error accrued with increasing capillary pressure as estimated based on the artificial CMT capillary meniscus data.

Since P_c values encountered in these experiments range from 100 Pa to 300 Pa, Figure 3.3 suggests that, based on the artificial meniscus data, the largest error encountered should be ~10%. To support this error estimate, a partially saturated capillary tube was imaged with CMT and the curvature of the meniscus was measured. The mean curvature (i.e. P_c) was found to be within 3.3% relative error from the analytical solution, and the relative error estimated from Figure 1 is 3.0%. Thus, the error versus P_c relationship (Figure 3.3) using the artificial CMT data is supported by experimental data. An additional validation was performed by measuring curvature on a CMT image of precision glass spheres. The measured radius of curvature for this data set was found to be within 5% of the true bead radius (0.8 mm ± 0.1 mm per manufacturer's specifications).

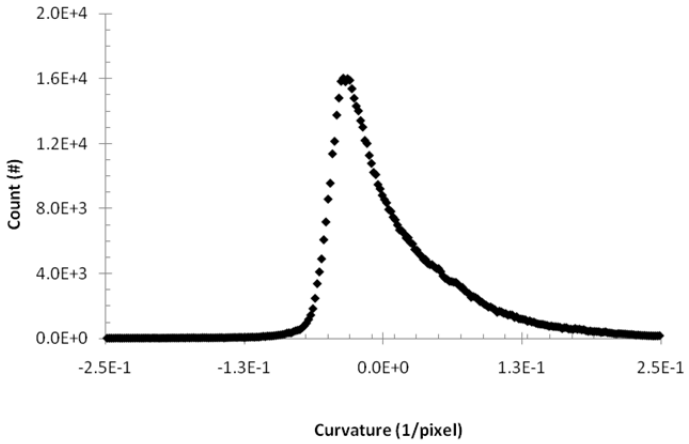

Figure 3.4: Distribution of curvature values for the connected phase interfaces, measured on a CMT image for a drainage point.

Figure 3.4 presents an example of curvature values measured from a single CMT volume of the connected wetting fluid interfaces. A convex interface is negative in the water phase, meaning that for water-wet media only negative curvatures should exist. However, the curvature distributions have a tail of unrealistic positive curvature values (Figure 3.4). After further analysis of the segmented images, it was discovered that the positive values are caused by segmentation error, which improperly reverses the curvature of very small interfaces (see above discussion related to pixelation issues). Interfaces that form pendular rings and interfaces located at pore necks are therefore most susceptible to segmentation error. What appears, to be correct curvatures are observed in Regions 1 and 2 in the gray-scale image in Figure 3.5a , however, after segmentation the interfaces either become flat (e.g. Region 1**,** Figure 3.5b) or curve the wrong way (e.g. Region 2, Figure 3.5b). This is also seen in the isosurfaces, see Figure 3.5c and 3.5d where the curvature values assigned to the surfaces are either zero (Region 1) or positive (Region 2).

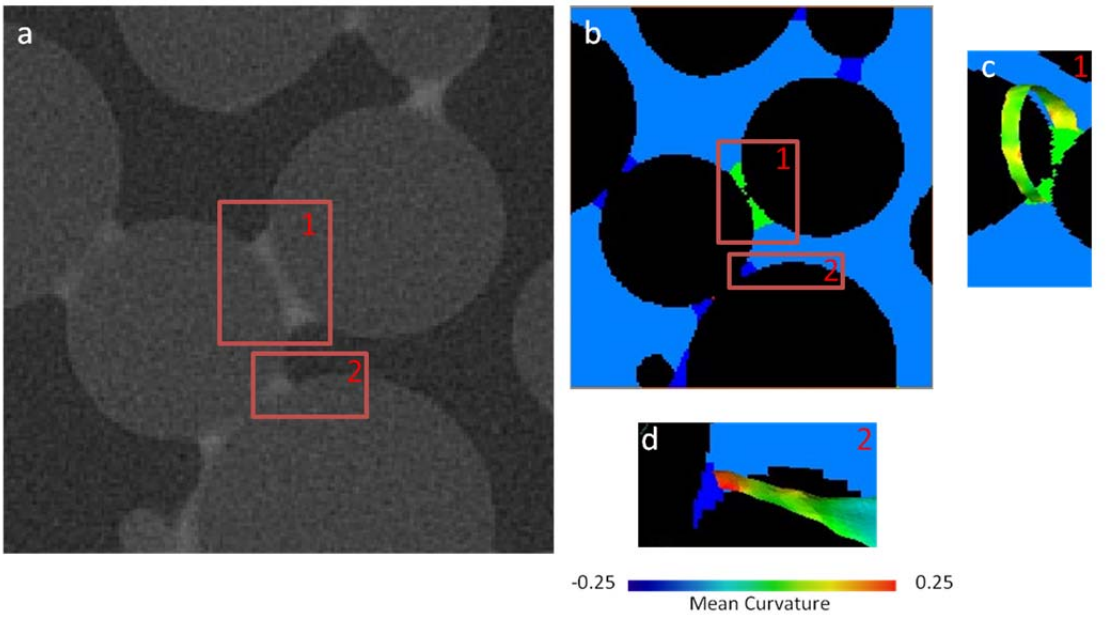

Figure 3.5: Example images of segmentation error, regions of interest are labeled 1 and 2 (red boxes). Gray-scale CMT image (a), segmented CMT image (b), connected water phase is dark blue, disconnected water phase is green, and oil is light blue. A pendular ring isosurface is shown in Region 1 (a and b) with incorrect zero curvature (c). A water/oil interface isosurface is shown in Region 2 (a and b) with incorrect positive curvature (d).

Figure 3.6 shows that the oil phase is less affected by segmentation error, since residual oil blobs exist as larger features (Figure 3.6a) than wetting phase pendular rings (Figure 3.6b). The curvature error resulting from inadequate segmentation of small features is clearly displayed in Figure 3.6b, where the interface for the pendular ring has become convex rather than concave. In Figure 3.7 we present example curvature values measured from a single CMT volume of the disconnected water phase interfaces (i.e. at low saturation). As expected, a single peak curvature value does exist for the collection of pendular rings. However, the majority of the curvature values are positive, and thus, the curvature of the disconnected water phase interfaces at this low saturation are incorrect. The disconnected oil phase interfaces, however, were not affected by the pixilation-related segmentation error; example histograms are provided in Figure 3.8 and are discussed in further detail below. To account for segmentation error, the incorrect positive curvature values were removed from further analysis when calculating P_c from curvature.

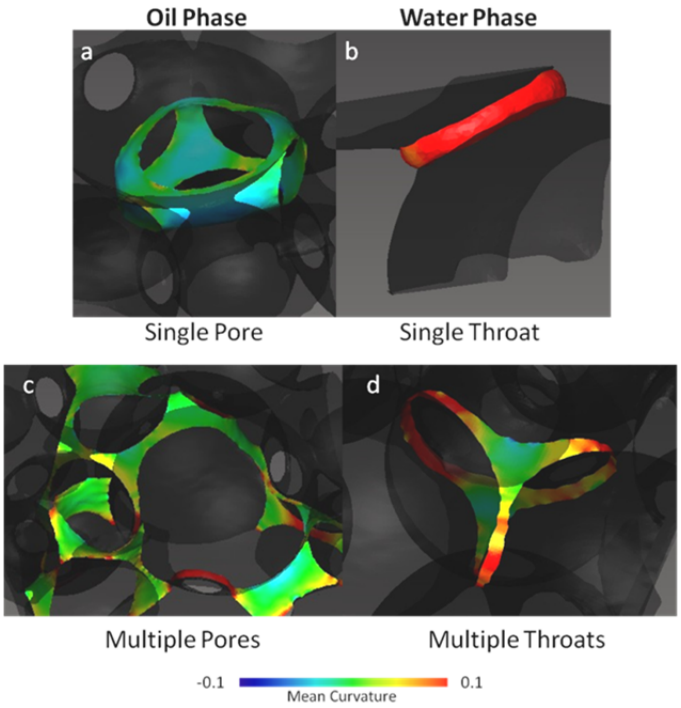

Figure 3.6: Example interfacial morphologies, only the isosurface representing the oil/water interface is shown. Disconnected oil blob trapped in a single pore (a). A pendular ring in a single pore neck (b). Large disconnected oil ganglion spanning multiple pores (c). Tri-pendular ring spanning three pore necks (d). The dark transparent phase is the glass beads.

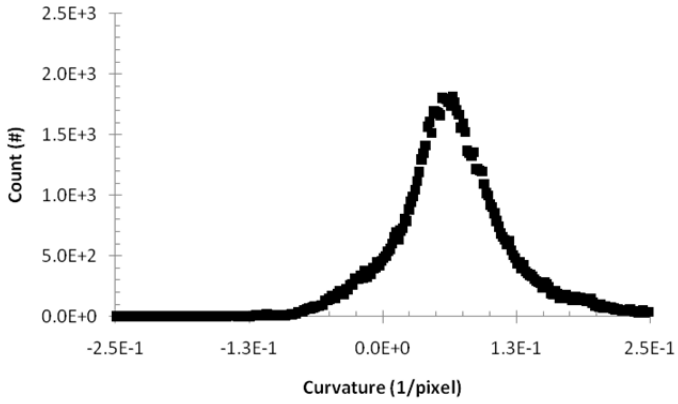

Figure 3.7: Distribution of curvature values for the *disconnected* water phase interfaces as measured from a CMT image, obtained during drainage.

3.4.2 Phase Connectivity and Residual Morphologies

Based on the separation of phases described above (classifying them as 4 different fluid configurations), CMT images were also analyzed for phase connectivity during drainage and imbibition. The existence of disconnected water in glass beads is debatable, and it is likely that water was connected throughout the column via thin films at low saturation. Regardless, disconnected fluid interfaces, identified via this analysis, have significantly different curvature than connected fluid interfaces (as discussed later) and are configured as expected in the pore space. For example, disconnected oil exists as isolated blobs (Figure 3.6a) and disconnected water exists as pendular rings (Figure 3.6b). Disconnected oil is also configured as larger ganglia that span multiple pores (Figure 3.6c) and in some instances disconnected water can be identified as a tri-pendular ring that connects three adjacent pore necks (Figure 3.6d).

Curvature distributions for disconnected oil phase interfaces, during imbibition and drainage, are presented in Figure 3.8a and 3.8b, respectively. These distributions show multiple "peak" pressures for the disconnected fluid interface. Relatively early during imbibition (S_w = 0.37), a small single peak curvature value is present (Figure 3.8a) and with increasing saturation, multiple new (and larger) peaks representing lower curvature values appear. Essentially, these "peak" values correspond to the P_c at which the majority of snap-off occurred and the trajectory of these "peak" values in relation to saturation demonstrates that, as imbibition proceeds, disconnected oil blobs with increasingly lower curvatures (i.e. lower P_c) become trapped. The opposite trend is true for drainage (Figure 3.8b) as disconnected oil becomes reconnected; oil blobs with increasingly higher curvatures become reconnected, until close to full oil saturation (low water saturation, S_w = 0.14) where only a few high curvature (i.e. large P_c) oil blobs remain. These results suggest that over a short time period (i.e. a time span short enough that interfacial relaxation is not occurring) the curvature distribution of disconnected fluid can be used as a history of P_c values experienced by a system.

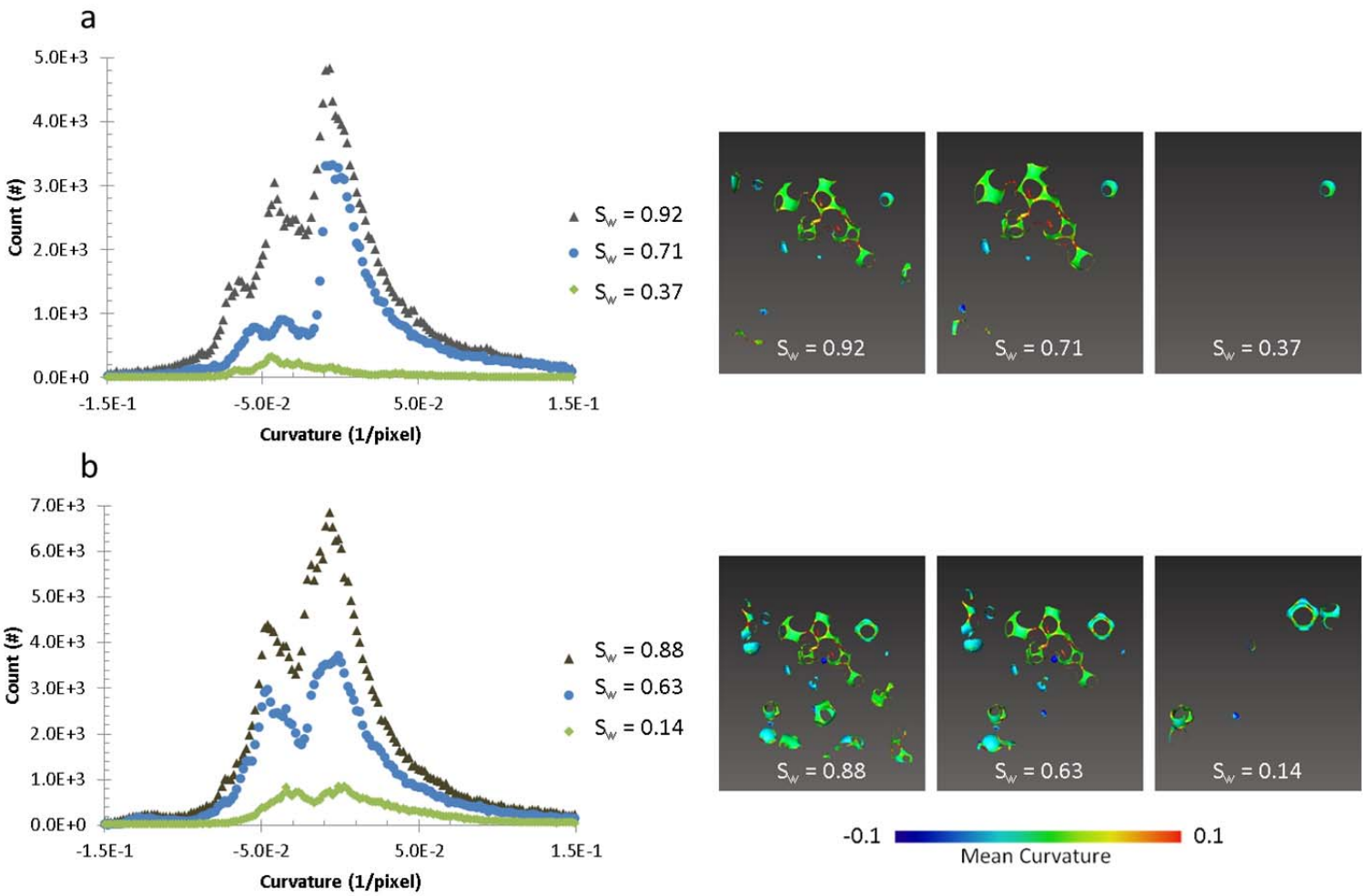

Figure 3.8: Curvature distributions for the disconnected oil phase interfaces during imbibition (a) and drainage (b), S_w is water saturation.

During primary drainage, disconnected non-wetting phase was identified. When changing saturation with the syringe pump, the system is in a state far from equilibrium and initially large pressure fluctuations occur (data not shown). We suspect that fluid phase rearrangement occurs during these pressure fluctuations. For example, under drainage, it is likely that both large and small pores are de-saturated, however, once the pump is stopped the smallest pores are immediately refilled with water (re-imbibition). The occurrence of re-imbibition during equilibration explains why disconnected non-wetting phase is identified during primary drainage. This disequilibrium is likely caused by a relatively large change in saturation with respect to time.

3.4.3 Capillary Pressure Measurements

Once the image volumes are segregated into four fluid configurations, the interface formed between connected water and connected oil is readily identifiable. To calculate P_c from curvature, the average interfacial curvature for connected fluid interfaces was calculated and then related to P_c using *Eq. 3.2*. Figure 3.9 compares the transducer-based and curvature-based (connected fluid only) capillary pressure-saturation curves. If average curvature for both connected and disconnected interfaces in the CMT image was used to calculate P_c the results show poor agreement with the transducer-based P_c measurement. This is to be expected since the P_c of disconnected fluid is not captured by externally measured P_c. Figure 3.9 shows that for drainage, the transducer-based P_c measurement is slightly higher than the curvature-based P_c measurement, yet, the curvature-based measurement corresponds very well with the transducer-based measurement for imbibition.

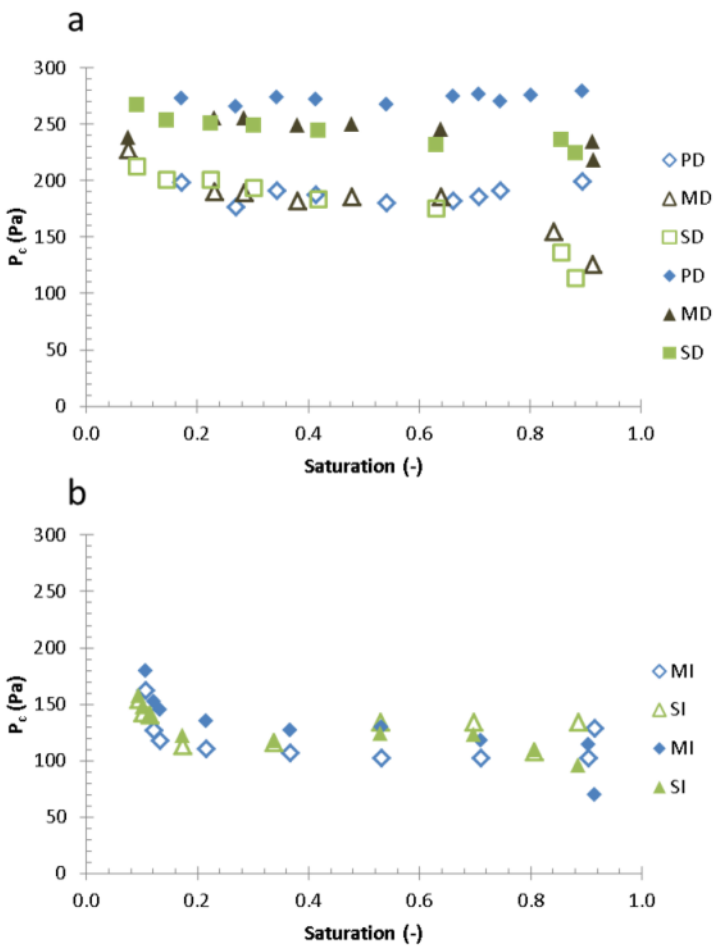

Figure 3.9: Capillary pressure saturation curves for drainage (a) and Imbibition (b). Curvature-based P_c (open symbols) and transducer-based P_c (closed symbols). For these figures PD is primary drainage, MD is main drainage, SD is secondary drainage, MI is main imbibition, and SI is secondary imbibition.

We identify three likely causes for the discrepancy between transducer-based and curvature-based P_c values: (1) error in the curvature estimate due to limited image resolution, (2) error in the transducer measurement, and/or (3) disequilibrium effects. To explore the first possible source of error we compared transducer-based P_c to curvature-based P_c (see Figure 3.10). A 1:1 line is expected at equilibrium, if our curvature measurement is 100% accurate. The data shows a definite upward trend, suggesting that random error is unlikely; however, systematic error is possible. Since error increases with increasing P_c (Figure 3.3) it would be expected that at larger P_c, the measured values would deviate from the 1:1 line. Indeed, measurements obtained during drainage (i.e. higher P_c than during imbibition) lie further

from the 1:1 line than measurements obtained during imbibition. While disequilibrium effects would also cause deviation from the 1:1 line, equilibrium is better evaluated by comparing changes in curvature as a function of equilibration time.

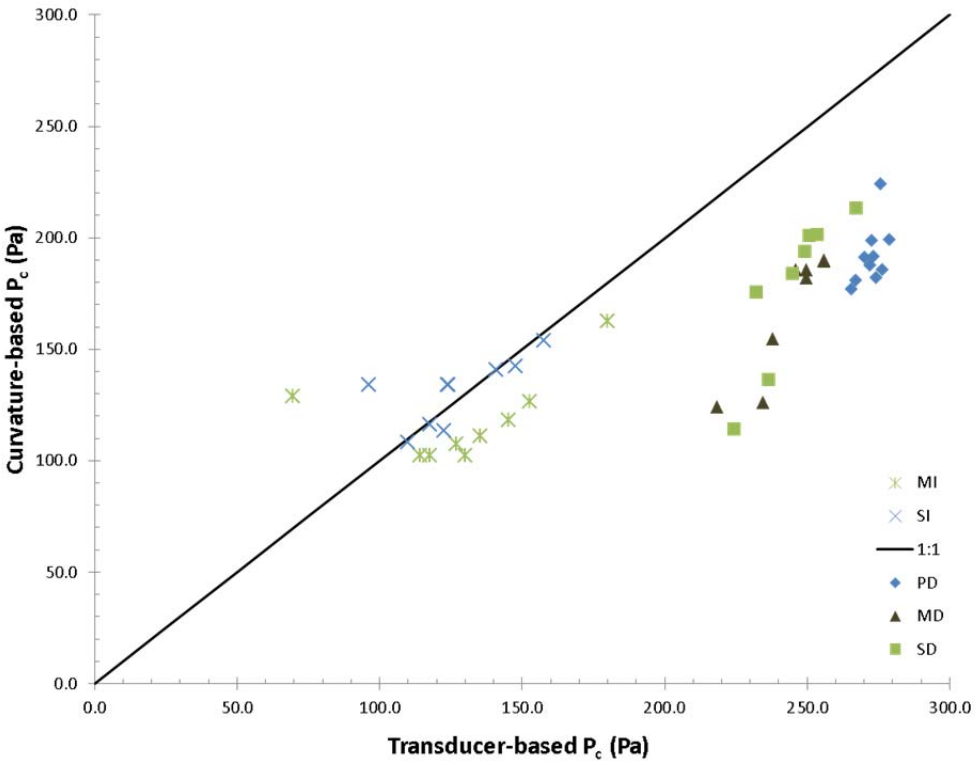

Figure 3.10: Transducer-based P_c versus curvature-based P_c measurements. For this figure PD is primary drainage, MD is main drainage, SD is secondary drainage, MI is main imbibition, and SI is secondary imbibition.

Figure 3.11 shows that the relative percent difference between curvature-based and transducer-based P_c measurements is dependent on the time allowed for equilibration prior to imaging. For both drainage and imbibition, the relative percent difference between the two measurement techniques decreased as equilibration time increased. While there were some effects due to saturation differences (errors that are more pronounced at higher P_c, as mentioned before, and could be the source of some noise) a consistent trend was obtained with increasing equilibration time (regardless of saturation). Results demonstrated that interfacial relaxation was occurring and that P_c values calculated from interfacial curvature did not match the P_c values measured by the pressure transducer prior to equilibration. We

observe that drainage equilibration appears to take longer than equilibration during imbibition, however, these differences could also be caused by the larger errors associated with the higher P_c values encountered during drainage. Overall, it is suspected that longer equilibration time would allow for P_c stabilization and more similar transducer-based P_c and curvature-based P_c values. The pressure transducer data was also analyzed for equilibration (not shown here) and the data indicate that interfacial relaxation was occurring. This suggests that while the fluid pressures in the wetting and non-wetting phases are changing and interfacial relaxation was occurring, the Young-Laplace equation (*Eq. 3.2*) is not valid and that dynamic relaxation of interfaces should be accounted for until equilibrium is achieved. While the exact mechanism through which interfacial relaxation occurs needs further investigation, our data suggests that relaxation was occurring. However, for less idealized porous media (and at larger scales) it is likely that the time needed for relaxation would differ from the time needed in the glass bead pack.

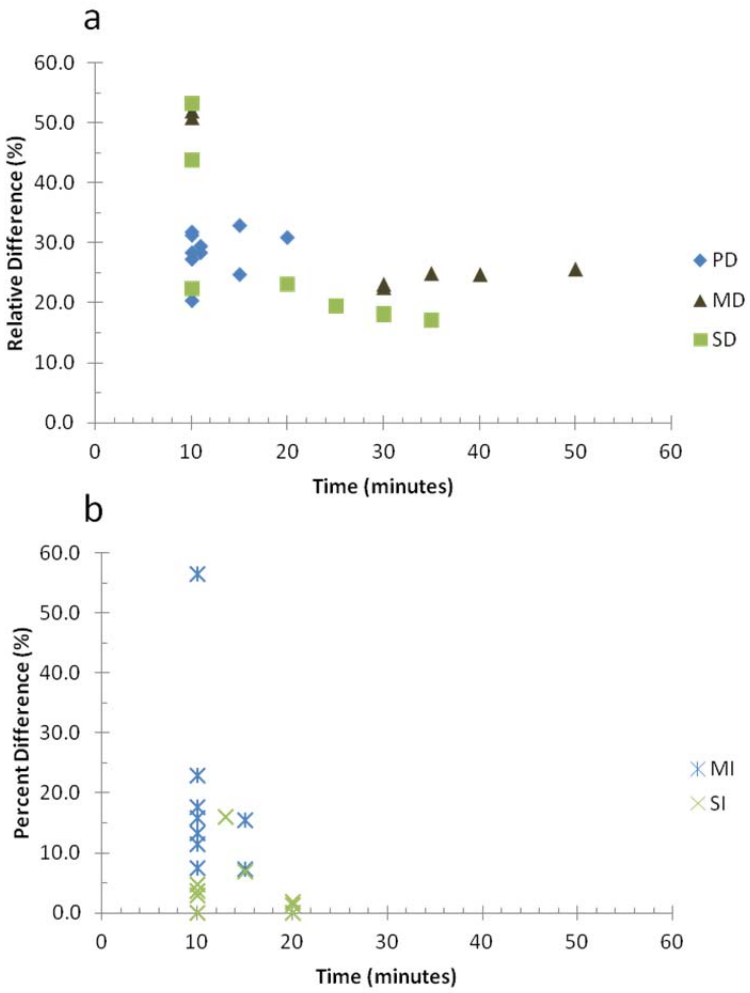

Figure 3.11: Relative percent difference between transducer-based P_c and curvature-based P_c as a function of equilibration time for drainage (a) and imbibition (b).

3.5 Conclusions

A method to measure interfacial curvature from CMT images was presented herein. The method was validated by measuring curvature on a few different ideal systems and then used to compare curvature-based and transducer-based P_c measurements during drainage and imbibition experiments. Overall, results between the two P_c measurement techniques agreed well at equilibrium, but, only if the disconnected fluid interfaces were excluded from consideration. The transducer-based P_c measurements differed rather significantly from curvature-based P_c measurements when equilibrium was not reached. Further experiments,

using longer equilibration times, and facilitating more accurate curvature measurements of the disconnected water phase interfaces via higher resolution images, are needed. Our results are the first to measure interfacial curvature using CMT data, allowing us to explore the capillary pressure saturation relationship from a new perspective, which should fuel further discussion about multiphase flow behavior. Based on the data obtained and analyses performed for this glass-bead pack we can establish the following conclusions:

- P_c based on curvature and transducer measurements compare well for connected fluid interfaces.
- Equilibrium was not reached for some of the early-scan data points.
- The Young-Laplace equation appears to misrepresent capillary pressure during interfacial relaxation.
- Curvature measurements can provide useful insights about multi-phase behavior, in particular transitions between dynamic and equilibrium states.
- Higher resolution images are required to properly segment small features (in this analysis small features, such as pendular rings, were omitted).
- Additional experiments using longer equilibration times are needed to further address equilibration issues.

3.6 Acknowledgement

Acknowledgment is made to the Donors of the American Chemical Society Petroleum Research Fund for support of this research (grant number 48505-AC9) and by US NSF (EAR 337711 and EAT 0610108). Microtomography was performed at GeoSoilEnviroCARS (Sector 13), Advanced Photon Source (APS), Argonne National Laboratory. GeoSoilEnviroCARS is supported by the National Science Foundation-Earth Sciences (EAR-0217473), Dept. of Energy-Geosciences (DE-FG01-94ER14466) and the State of Illinois. Additionally, we would like to acknowledge the following people for their help with either collecting the data: Mark Rivers (GSECARS APS / University of Chicago), or with interpreting the results: James McClure (University of North Carolina), Casey Miller (University of North Carolina), William Gray (University of North Carolina), and Adrian Sheppard (Australian National University).

Chapter 4. Decoupling the Mechanisms of Microbial Enhanced Oil Recovery

Ryan T. Armstrong[1] and Dorthe Wildenschild[1]

1. School of Chemical, Biological and Environmental Engineering, Oregon State University, 103 Gleeson Hall, Corvallis, OR 97331-2702

Journal of Petroleum Science and Engineering
233 Spring Street, New York, NY 10013
Submitted 10/19/2011

4.1 Abstract

Microbial enhanced oil recovery (MEOR) is a process where microorganisms are used for tertiary oil recovery. Numerous mechanisms have been proposed in the literature through which microorganisms facilitate the mobilization of residual oil. Herein, we investigated the MEOR mechanisms of interfacial tension reduction (via biosurfactant) and bioclogging in water-wet micromodels. The microorganisms used were *Shewanella oneidensis* (MR-1) that causes bioclogging and *Bacillus mojavensis* (JF-2) that produces biosurfactant and causes bioclogging. Micromodels were flooded with an assortment of flooding solutions ranging from metabolically active bacteria to nutrient limited bacteria to dead inactive biomass to assess the effectiveness of the proposed MEOR mechanisms of bioclogging and biosurfactant production. Results indicated that tertiary flooding of the micromodel system with biomass and biosurfactant was optimal for oil recovery due to the combined effects of bioclogging of the pore-space and interfacial tension reduction. However, biosurfactant was able to recover oil in some cases dependent on wettability. Biomass without biosurfactant that clogged the pore-space also successfully produced additional oil recovery. When analyzing residual oil blob morphology, MEOR resulted in oil blob size and radius of curvature distributions similar to those obtained by an abiotic capillary desaturation test, where flooding rate was increased post secondary recovery. Furthermore, for the capillary number calculated during MEOR flooding with bioclogging and biosurfactant, lower residual oil saturation was measured than for the corresponding capillary number under abiotic conditions. These results suggest that bioclogging and biosurfactant MEOR is a potentially effective approach for pore morphology modification and thus flow alteration in porous media that can have a significant effect on oil recovery beyond that predicted by capillary number.

4.2 Introduction

Microbial enhanced oil recovery (MEOR) is a tertiary recovery process where bacteria and their metabolic by-products are utilized for oil mobilization in a reservoir. Metabolic by-products are the assortment of compounds produced through microbial metabolic pathways during growth, for example, one such, metabolic by-product can be biosurfactant In principle, MEOR is a straightforward concept where increased recovery occurs through inoculation of a reservoir with microorganisms to clog pores and redirect flow, or to mobilize oil as a result of reduced interfacial tension. But to this point, oil production at the field-scale with MEOR has been inconsistent at best (Hitzman, 1988, 1983; Lazar, 1991). However, results from numerous lab-scale experiments with an assortment of microbial species and a wide range of porous material suggest that MEOR can be an effective tertiary oil recovery

method (Bordoloi et al. 2007; Bryant et al. 1998; Crescente et al. 2008; Soudmand-asli et al. 2007; Suther et al. 2009). One reason for the discrepancy between field-scale and lab-scale results is a lack of understanding of the fundamental mechanisms at the pore-scale through which bacteria impact fluid dynamics, rock surface properties, and interfaces between immiscible phases.

Numerous proposed MEOR mechanisms are presented in the literature, as reviewed in Chapter 2. For an in-depth review of each mechanism and the microbial species involved we refer to Youssef et al. 2009. The MEOR mechanisms of bioclogging, interfacial tension reduction, and wettability alteration have been studied by Afrapoli et al. (2010), Bredholt et al. (1998), Crescente et al. (2008, 2006), and Kowalewski, et al. (2006). In these studies, the emulsification ability of *Rhodococcous sp*. (094) was activated or deactivated depending on the carbon source used for growth and two variants were defined: cells of surfactant-producing bacteria (SPB) and cells of non-surfactant-producing bacteria (NSPB). This approach attempts at decoupling the MEOR mechanisms of bioclogging and biosurfactant production and results from these efforts demonstrate that wettability change with *Rhodococcous sp*. (094) is dependent on which variant is used (Afrapoli et al. 2010). However, the MEOR mechanisms were not completely decoupled, because in the micromodel studies reported by Crescente et al. (2006) the NSPB eventually became SPB due to the presence of dodecane in the micromodel system and experiments with either variant gave the same end results (i.e. microbial accumulation of organism at the oil/water interface and utilization of dodecane as a carbon source with marginal oil recovery of ~9%).

Mobilization of residual oil in porous media has been studied since the early 1980s and it is well understood that residual oil exists as disconnected globules in the subsurface. These globules remain trapped until a force sufficient enough to move them through an adjacent pore neck is applied (Wardlaw and McKellar 1985). In this situation, the ratio between viscous forces that promote flow and capillary forces that resist flow becomes important and is characterized by a unitless ratio, called the capillary number (*Eq. 2.12*). As capillary number increases, capillary forces become less dominant and the likelihood of oil mobilization increases (Gray et al. 2008). Under abiotic conditions where capillary number is increased by increasing flood velocity, solitary ganglia: undergo mobilization, remain trapped, or break-up into multiple daughter ganglion (Wardlaw and McKellar 1985). As stated by Melrose and Brander (1974), "the critical condition for ganglion mobilization is that the pressure drop

from one end of an oil blob to the other, in the direction of flow, must exceed the maximum of the capillary pressure difference between the menisci at the upstream and downstream ends of the oil blob". Once the critical condition is achieved individual ganglion are either mobilized or broken up into multiple smaller daughter ganglion (Wardlaw and McKellar 1985).

Oil blob size distributions in porous media have been widely investigated in the literature (Al-Raoush et al. 2005a, 2005b; Karpyn et al. 2010). Mayer and Miller (1992) proposed to fit NAPL blob size distributions to the Van Genuchten function:

$$F(d) = 1 - [1+(\beta d)^m]^{(1/m)-1} \quad (5.1)$$

where, d is blob size, F(d) the mass percentage of blobs that are smaller than d, and β and m are fitting parameters. In general, β increases with decreasing mean blob size and m is larger for more uniformly distributed blobs. Thus, a convenient quantitative comparison of blob size distributions between different oil recovery experiments is possible using this approach.

Wettability is a major factor controlling multi-phase flow, and thus oil production (Al-Raoush 2009; Graue et al. 1999; Karpyn et al. 2010; Morrow and Mason 2001; Tweheyo et al. 1999). To quantify porous media wettability, macro-scale indices (obtained with techniques such as the Carter, USBM, or Amott methods) are used regularly. However, these measurements lack the capability to characterize wettability change during MEOR treatment, and only provide macro-scale information. To understand micro-scale temporal and spatial changes in wettability, as proposed herein, interfacial radius of curvature measurements using level set methods (Cheng et al. 2007; Liu et al. 2011; Sethian 1996) could be used. When applying this approach, curvature from the perspective of the oil phase is positive for a concave interface (i.e. water-wet surface) and negative for a convex interface (i.e. oil-wet surface). Consequently, lateral shifts in the radius of curvature distribution (i.e. from positive to negative or vice versa) are indicative of wettability change.

The objective of the present study was to investigate the proposed MEOR mechanisms by treating the micromodel system with an assortment of different MEOR flooding solutions ranging from metabolically compromised (i.e. inactive) bacteria to active bacteria to

biosurfactant only. Through these efforts the following questions are addressed. To what extent is oil recovery dependent on the activity of the microbial community? Can dead inactive biomass recover the same amount of oil as actively growing bacteria? Can metabolic by-products (such as, a biosurfactant) recover oil or is bacterial cell mass required for recovery? Conversely, can bacterial cell mass recover oil via clogging or is a biosurfactant required?

When analyzing a successful lab-scale MEOR experiment it is often difficult to accredit additional oil recovery to a single MEOR mechanism since these mechanisms do not occur independently and many studies use non-transparent 3D cores that occlude direct visualization of the processes taking place. In this study, we utilize a stereo microscope to study MEOR in a 2D silicon etched micromodel system. Two microorganisms are used; *Bacillus mojavensis* (JF-2) which is a gram-positive, biosurfactant producing, biofilm forming, facultative aerobe isolated from oil reservoir brine in Oklahoma, and *Shewanella oneidensis* (MR-1) which is a gram-negative, biofilm forming, facultative aerobe isolated from Lake Oneida in New York. The MEOR mechanisms of biogenic gas generation and hydrocarbon degradation are not considered since the organisms used are not biogenic gas generators nor are they known hydrocarbon degraders. The MEOR mechanisms investigated (i.e. IFT reduction, wettability change, and bioclogging) were evaluated in terms of additional oil recovered, residual oil blob size, and interfacial curvature which are parameters essential for understanding the mobilization of capillary trapped oil.

4.3 Materials and Methods

4.3.1 Bacterial Strains and Growth Conditions

Bacillus mojavensis (JF-2, ATCC 39307) and *Shewanella oneidensis* (MR-1, ATCC 700550) were obtained from ATCC. Both organisms were grown in a brine-based growth media called Media E at room temperature under aerobic conditions (Table 4.1). However, MR-1 was grown with 60% less NaCl than reported for Medium E.

Table 4.1: Growth Medium E.

NaCl	25.0 g/L
$(NH_4)_2SO_4$	1.0 g/L
$MgSO_4$	0.25 g/L
Glucose	10 g/L
Phosphate Buffer	100 mM
Trace Metals Solution	1.0%
Yeast Extract	2.0 g/L

4.3.2 Flooding and MEOR Solutions

Media E was used for water flooding and the oil phase was Soltrol 220 which is a mixture of C_{13} and C_{17} hydrocarbons. In total, six flooding solutions were tested to address the questions proposed in the Introduction. For MEOR with JF-2, five different flooding solutions were used: (1) JF-2 / fresh media, (2) JF-2 / spent media, (3) compromised JF-2 / fresh media, (4) compromised JF-2 / salt solution, and (5) no cells / biosurfactant. The last flooding solution (6) was MR-1 / spent media.

Flooding solution (1) was generated by growing JF-2 overnight in batch culture and then centrifuging the bacterial culture at 9,000 rpm for 10 minutes followed by resuspension of JF-2 in new growth media. Flooding solution (2) was generated by growing JF-2 overnight in batch culture without resuspension in new media. For flooding solution (3) a JF-2 culture grown overnight was subjected to 20 mg/L KI for 2 hours followed by centrifugation and resuspension in fresh growth media with 2 mg/L ampicillin. Flooding solution (4) was prepared the same way as flooding solution (3), however, JF-2 was resuspended in a nutrient free 25 g/L NaCl solution (which is the same NaCl concentration as Media E). The biosurfactant flooding solution (5) was prepared by separating JF-2 biomass from spent cultures (i.e. after exponential growth). To separate the produced biosurfactant from the bacterial cells, microbial cultures of JF-2 were centrifuged at 9,000 rpm for 10 minutes

followed by filtration of the supernatant through a 0.22 µm pore diameter membrane. The IFT of the resulting biosurfactant solution matched the IFT achieved with flooding solution (2). Flooding solution (6) was prepared by growing MR-1 overnight in Media E (with 60% less NaCl) without resuspension in new media.

4.3.3 Micromodel

A pattern modeled after a 3D glass bead pack (Figure 4.1) was photo-etched into a silicon wafer to a depth of 50 microns. To create hydrophilic flow channels, the manufacturer treated the silicon surface in an O_2 plasma at 100 mtorr and 100 W of forward power in a parallel plate RIE (reactive-ion etching) system. Micromodels with two different oil/water contact angles were created: $19^{o}\measuredangle$ and $38^{o}\measuredangle$. Contact angle was measured by submerging a treated silicon wafer in Soltrol 220 and then placing a water droplet on the surface. The water droplet was imaged with a stereo microscope and the resulting contact angle was computed using ImageJ software based on B-spline snakes (active contours, Stadler et al. 2006)

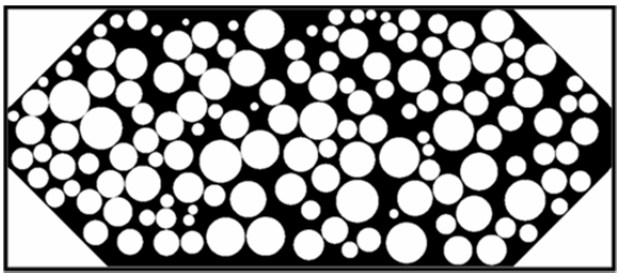

Figure 4.1: Micromodel pattern (black = flow channels, white = solid).

4.3.4 Flooding Procedure

Water flooding was performed under fixed flux conditions using a capillary number (N_{ca}) of $7.9x10^{-7}$ (see Section 2.2.2). The micromodel was initially saturated with Medium E followed by saturation with Soltrol 220 at $N_{ca} > 10^{-3}$ to ensure complete saturation, which is visually confirmed. To simulate secondary recovery, the oil-saturated micromodel was then flooded with Medium E until oil recovery ceased and residual oil remained as a disconnected phase.

4.3.5 MEOR

After water flooding, 1 of the 6 MEOR flooding solutions mentioned above was used for MEOR. MEOR was conducted at the same flow rate as water flooding ($N_{ca} = 7.9x10^{-7}$) and the test was terminated once no additional oil was recovered. Prior to each experiment the micromodel and tubing was sterilized with 100% ethanol followed by a 3x rinse with sterile growth media.

A standard curve relating bacterial cell mass (as dry weight) to optical absorbance of a bacterial solution at 600 nm was generated. Dry cell mass was measured by filtering cell cultures through a 0.45 μm (nominal diameter) membrane, rinsing the cell cake with 3 100ml aliquots of DI H_2O and then drying the cell mass at 80^oC for 24 hours. The dried cell mass was then weighed and related to optical absorbance. Optical absorbance measurements (Beckman Coulter spectrophotometer DU ® 530) were then used to calculate the biomass concentration in each MEOR flooding solution.

4.3.6 Abiotic Recovery

A capillary desaturation curve was produced for both the $19^o\measuredangle$ and $38^o\measuredangle$ micromodels by increasing the flow rate logarithmically. Water flooding was initiated at $N_{ca} = 7.9x10^{-7}$, which was increased until essentially no residual oil remained in the micromodel. With each 10 fold flow rate increase, equilibrium was reached by allowing three pore volumes of the flooding phase to pass through the micromodel. Once equilibrium was reached, residual oil saturation was measured and the flow rate was increased further.

4.3.7 Light Microscopy

A stereo microscope (Leica Z16 APO) equipped with a 3.3 megapixel digital camera (QImaging MicroPublisher 3.3 RTV) and automated image capture software (QCapture Pro) was used. All published images were acquired with a 0.8x objective, 1.0x camera mount, and 0.5x zoom setting, resulting in images with an 8.3 μm/pixel resolution. Microscope images were written into TIFF file format with a 2048 x 1536 pixel window.

UV dye (Multi-Purpose Total Dye) was added to the oil phase to provide the necessary contrast for image segmentation. The UV dye was excited with a standard UV bulb emitting light between 400 and 500 nm, which caused fluorescence around 550 nm. Microscope images were used to calculate original oil in place, residual oil saturation, additional oil recovery, residual oil blob size, and interfacial radius of curvature.

4.3.8 Image Segmentation and Analysis

Colored 16-bit images were acquired; filtering out the red and blue channels of the colored image enhanced the signal produced by the oil phase UV tracer (Figure 4.2). The resulting gray-scale image was median filtered (2x kernel, Figure 2b) and a threshold was used to delineate the oil phase (Figure 4.2c). Since the physical pore volume of the micromodel is known only the oil phase volume, as calculated from the microscope images, was needed to calculate oil saturation.

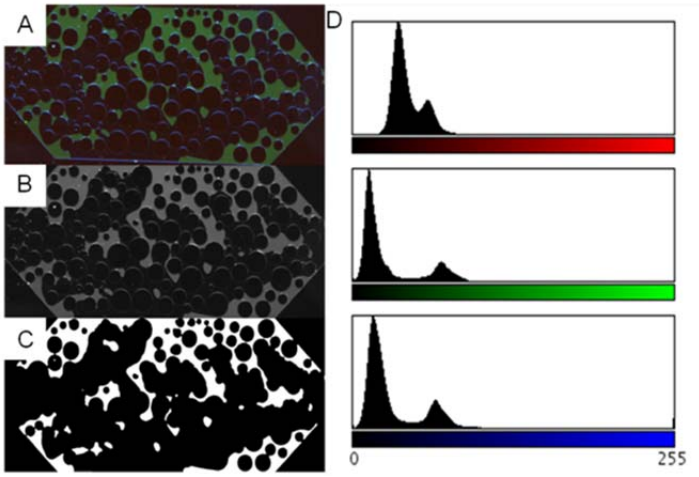

Figure 4.2: Image segmentation. (a) 16-bit RBG colored image (green = oil), (b) median filtered 16-bit gray scale image, (c) binary image, (d) red, green, and blue channel histograms for image (a).

Interfacial curvature was calculated from the stereo microscope images using level set methods (Sethian 1996; Cheng et al. 2007; Liu et al. 2011) where the curvature (K) of each level set is easily obtained from the divergence of the unit vector normal to a front (*Eq. 2.15*).

The curvature algorithm was tested by overlaying circles of known radii onto a 2D pattern of a glass bead pack (Figure 4.1). Radius of curvature for each circle (where radius of curvature is the inverse of curvature) was calculated and compared to the known value. The largest percent error encountered was 5.0% while most errors were less than 2%. Cheng et al. (2007) found that the error generated with this method was mainly due to radius size, resulting in larger error for smaller radius of curvature.

Individual oil blob size was calculated by finding connected components in the binary residual oil image using a neighborhood pixel connectivity of 8. Each connected object was classified as an oil blob and volumes are reported as the number of pixels representing a given blob.

Interfacial tension was measured using a du Noüy ring tensiometer (CSC No. 70545). And viscosity was measured using a viscometer (falling sphere type, VWR).

4.4 Results and Discussion

Results reported as *AOR* per biomass infused into the micromodel for the MR-1 flooding solution and four of the five JF-2 flooding solutions are presented in Figure 4.3. Results are for the $38^{o}\measuredangle$ micromodel, since this is the most comprehensive dataset and results for the biosurfactant flooding solution are excluded, since no biomass was infused with this treatment. Bacteria suspended in fresh media and bacteria suspended in spent media recover approximately the same quantity of oil. Compromised bacteria suspended in fresh media gave the best oil recovery while compromised bacteria suspended in the salt solution recovered no oil. The IFT between Media E and Soltrol was measured at 24.5 dynes/cm which was the IFT during water flooding; however, the IFT between the salt solution and Soltrol was slightly larger (29.0 dynes/cm). The IFT results reported in Figure 4.3 are for IFT during MEOR and correspond to the IFT between a given flooding solution and Soltrol 220. In the case of the compromised bacteria suspended in new media some metabolic activity definitely occurred, because surface tension (i.e. air/flooding solution) was reduced from 54.3 dynes/cm to 40.1 dynes/cm during treatment, resulting in a final IFT between Soltrol and the flooding solution of 8.7 dynes/cm. This suggests that some biosurfactant production

was occurring, and thus, metabolic activity was present. However, IFT reduction was not as drastic as treatment with bacteria suspended in fresh media or bacteria suspended in spent media which resulted in final IFT values of 0.4 and 0.7 dynes/cm, respectively. The MR-1 treatment without biosurfactant production and marginal IFT reduction resulted in 7.1% additional oil recovery (a reduction in IFT from 24.5 to 12.1 dynes/cm was observed and is likely caused by the production of metabolic by-products and not the production of a biosurfactant). Furthermore, biosurfactant treatment with a minimum IFT of 1.2 dynes/cm recovered no oil (this is later explained by the capillary desaturation curve). These results demonstrate the significance of bioclogging with JF-2 since the highest *AOR* values reported were obtained for bioclogging with minimal IFT reduction. Conflicting results are obtained for bioclogging with MR-1, since only marginal recovery was measured; however, micromodel images show that less MR-1 biomass clogged the micomodel pore-space than JF-2 biomass (compare Figure 4.3, columns b and e).

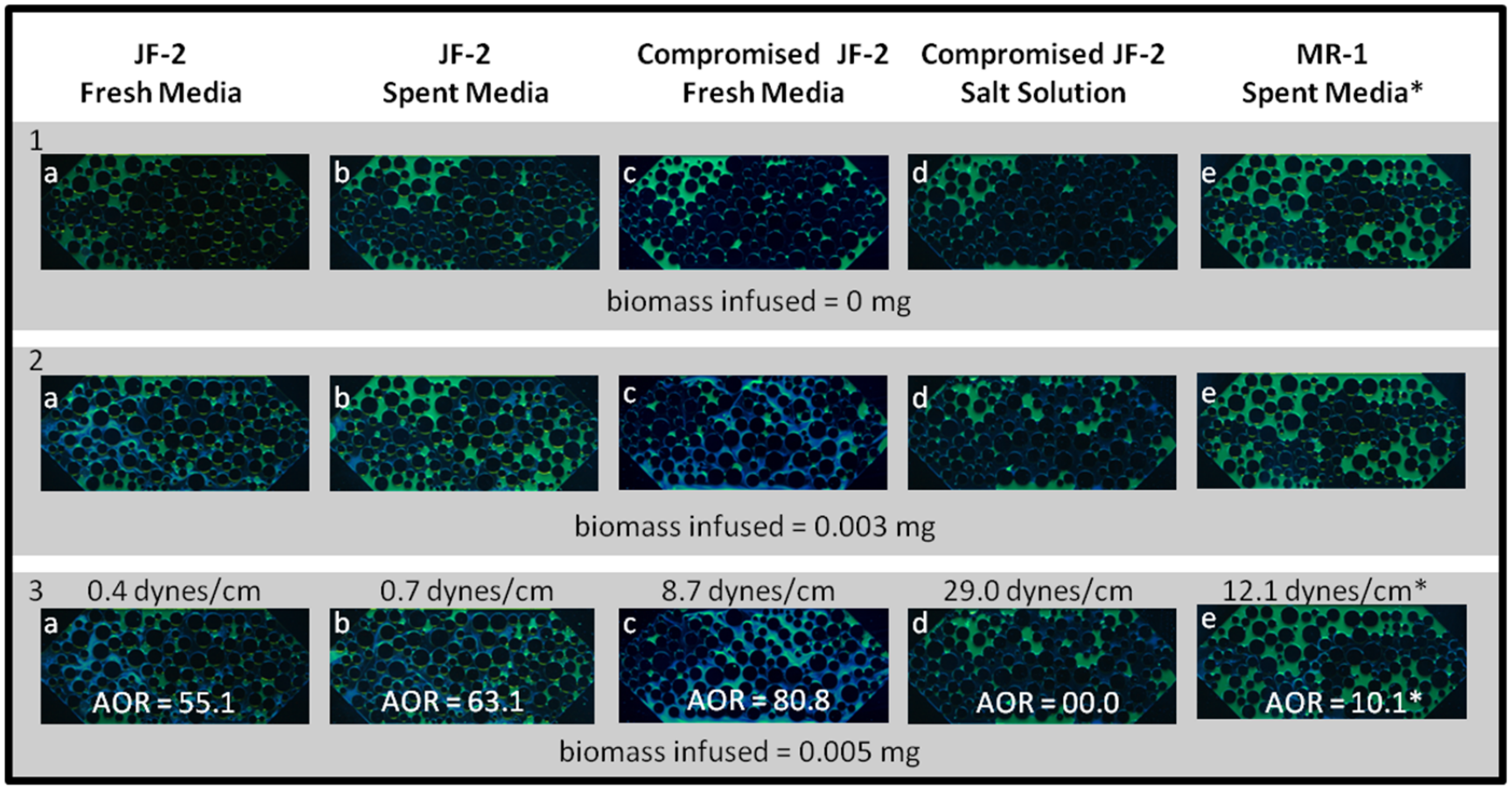

Figure 4.3: Selected stereo microscope images for each flooding solution tested for the 38° ∡ micromodel. Results are reported as *AOR* per biomass infused into the micromodel (green = oil, blue/white = biomass). Each column corresponds to a given flooding solution and each row corresponds to equivalent biomass infused.

Although the same quantity of biomass was infused during MEOR for each flooding solution the amount of biomass that clogged the micromodel during treatment varied significantly based on visual observation. Compromised bacteria suspended in the salt solution were the least effective at bioclogging and resulted in no oil recovery (Figure 4.3, column d). MR-1 biomass was very sparse, and this was the second least efficient oil recovery approach in terms of *AOR*. Bacteria suspended in fresh media did not start clogging the micromodel until after 24 hours which is well beyond the batch growth cycle of JF-2 and essentially makes this treatment option equivalent to treatment with bacteria in spent media. Both JF-2 treatment options (i.e. fresh media and spent media) gave similar *AOR* results and the extent of bioclogging with either treatment was visually similar (Figure 4.3, column a and b). In addition to the significance of bioclogging for oil recovery, these results demonstrate that potentially "stressed" JF-2 cultures suspended in spent medium or treated with KI and suspended in growth medium with ampicillin appeared to more effectively clog the micromodels (Figure 4.3, column b and c). At this point, it is not possible to suggest any potential stress induced bioclogging mechanisms, without a thorough analysis of the microbial communities nutrient uptake rates and the expression of potential stress induced genes. However, it was observed that in batch culture, during late stationary phase, JF-2 cells would coagulate together forming larger particles, which should be more effective at clogging than individual cells.

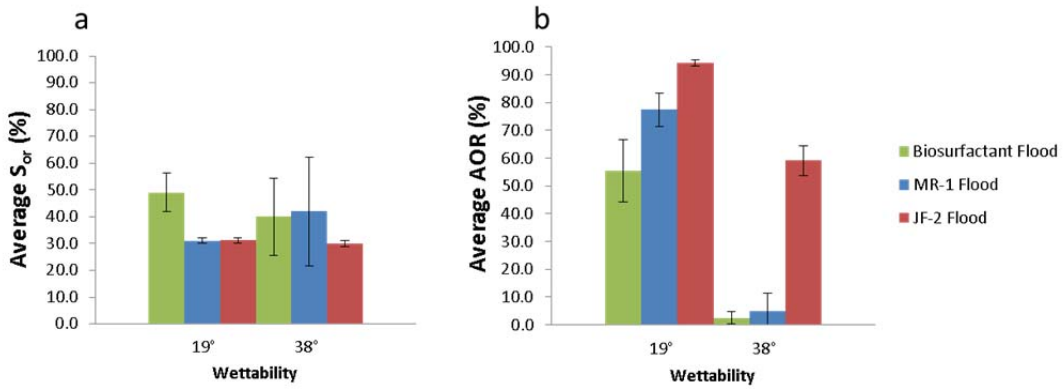

Figure 4.4: Results for residual oil saturation after water flooding (a) and additional oil recovered after MEOR (b) for the $19^{o}\measuredangle$ and $38^{o}\measuredangle$ micromodels. Results are averages of triplicate experiments and error bars correspond to a 90% confidence interval.

To investigate the effect of wettability on oil recovery using MEOR, three different treatment options (i.e. biosurfactant, JF-2 in spent media, and MR-1 in spent media) were tested in

both the 19° ∡ and 38° ∡ micromodels. Results for S_{or} and *AOR* for each treatment option and each micromodel are presented in Figure 4.4. Independent of contact angle, simultaneous bioclogging and biosurfactant treatment with JF-2 was the most effective MEOR treatment. The average S_{or} for biosurfactant treatment with the 19° ∡ micromodel is considerably larger than the average S_{or} for MR-1 and JF-2 treatments (Figure 4.4a). However, this does not detract from the *AOR* results since MR-1 and JF-2 treatments initially started with a lower S_{or} than biosurfactant treatment and still achieved a greater *AOR*. The measured IFT between the biosurfactant solution and Soltrol 220 during the 19° ∡ micromodel experiment was 0.4 dynes/cm while the measured IFT between the biosurfactant solution and Soltrol 220 during the 38° ∡ micromodel test was 1.2 dynes/cm. This difference in IFT between the two biosurfactant treatments may have resulted in some disparity between the *AOR* values obtained in the 19° ∡ and 38° ∡ micromodel experiments; however, the difference in *AOR* is most likely a result of wettability (which is later explained via consideration of the capillary desaturation curve data). For all treatment options, *AOR* was highest in the 19° ∡ micromodel while lower *AOR* values were obtained for the 38° ∡ micromodel, indicating that for these micromodel systems, MEOR is most effective for highly water-wet conditions.

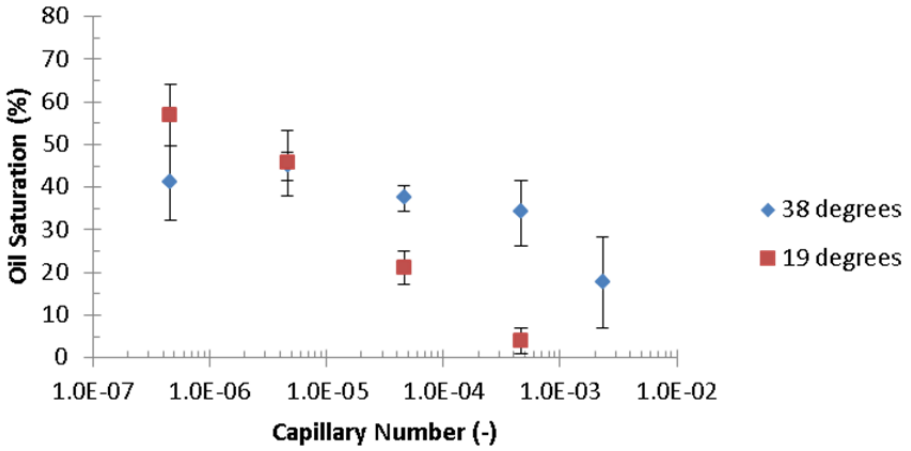

Figure 4.5: Results for residual oil saturation after water flooding (a) and additional oil recovered after MEOR (b) for the 19° ∡ and 38° ∡ micromodels. Results are averages of triplicate experiments and error bars correspond to a 90% confidence interval.

To further investigate the significance of wettability, a capillary desaturation curve under abiotic conditions was established for both micromodels (Figure 4.5). The capillary

desaturation curves show that an order of magnitude higher capillary number is needed in the 38° ∠ micromodel to achieve the same recovery as the 19° ∠ micromodel, which explains why oil recovery with biosurfactant treatment was successful in the 19° ∠ micromodel, but did not occur in the 38° ∠ micromodel. When secondary recovery in the 38° ∠ micromodel was performed at a capillary number of 10^{-6} followed by biosurfactant treatment, an *AOR* of 14.1% was achieved, which is consistent with the capillary desaturation curve for the 38° ∠ micromodel, giving an oil saturation of 0.39 at a capillary number of 10^{-5}. Overall, these results demonstrate that as contact angle increases, a significantly larger capillary number is needed for oil recovery in the micromodel system and that using MEOR (i.e. with bioclogging and biosurfactant) a 2-3 order of magnitude increase in capillary number is possible. For example, with JF-2 treatment in the 19° ∠ micromodel, initially flooded at $N_{ca} = 7.9x10^{-7}$, final oil saturation was ~5% which corresponds to a capillary number of 10^{-4} on the capillary desaturation curve, thus MEOR-facilitated oil recovery can be explained by a 3 order of magnitude increase in capillary number.

Because MEOR was performed under fixed flux conditions, capillary number can be calculated by taking into account changes in IFT, viscosity, and porosity (which ultimately affects pore velocity). Biomass formed by JF-2 was dense enough to provide sufficient contrast for image segmentation of the biophase; thus, porosity change could be calculated from the collected images. Porosity values from an upper and lower image threshold were used for calculating average pore velocity. The horizontal error bars for JF-2 in Figure 4.6 represent these lower and upper bounds. The porosity calculation assumed that biomass spanned the entire 50 µm micromodel depth and that no micro-porosity existed in the biomass (thus, biomass was considered impermeable). Viscosity was measured using a falling sphere viscometer and results indicate a viscosity of 1.2 cP for the JF-2 flooding solution in spent media. MR-1 biofilm was not dense enough to facilitate such analysis and is excluded from these calculations. The analysis was only carried out for the 19° ∠ micromodel data since this dataset provided recovery results for both the biosurfactant and JF-2 treatments.

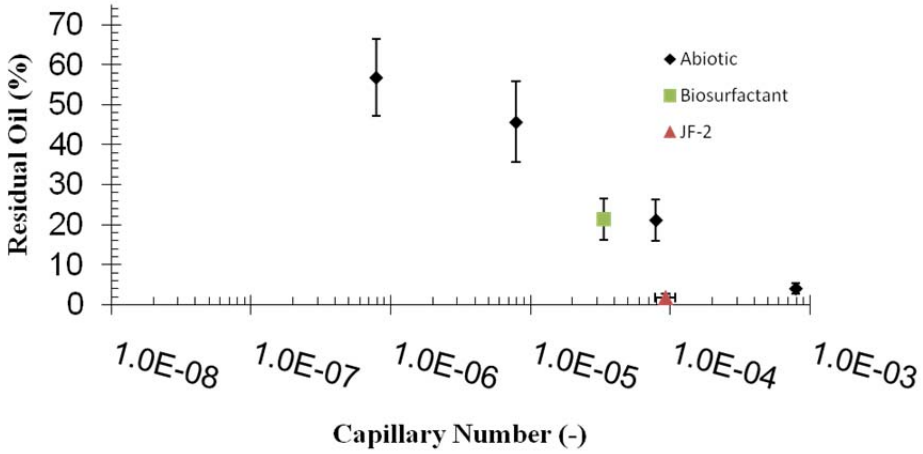

Figure 4.6: Capillary desaturation curve for the 19o∠ micromodel in comparison to residual oil saturations for the biosurfactant and JF-2 MEOR tests. The vertical error bars correspond to a confidence interval of 0.95. The horizontal error bar for JF-2 corresponds to the threshold limits obtained during image segmentation of the JF-2 biofilm. Results are based on triplicate experiments.

In the 19^{o}∠ micromodel residual oil saturation after biosurfactant treatment (carried out at N_{ca} = 7.9x10^{-7}) corresponded to the oil saturation obtained for the equivalent capillary number during the abiotic test; thus, recovery in the case of biosurfactant treatment was uniquely explained by IFT reduction (Figure 4.6). For JF-2 treatment, oil recovery was not entirely explained by capillary number since lower residual oil saturation was obtained at a capillary number below that used in the abiotic test. We conclude that the additional *AOR* obtained with JF-2, which could not be explained by capillary number change, was caused by the re-direction of preferential flow paths due to biofilm formation. After water flooding, microscope images (Figure 4.7) show that residual oil saturation is heterogeneous and that large oil globules exist in regions disconnected from the preferential flow path that appears to proceed along the middle region of the micromodel. Final images of bioclogged micromodels display disproportionate bioaccumulation near the inlet and central preferential flow path of the micromodel (Figure 4.7). This should essentially redirect flow to outer regions of the micromodel that were not efficiently swept during water flooding. Accumulation of biomass in the pore-space of the preferential flow path is reasonable since advective transport of biomass should be greatest in this region. This proposition is supported by the modeling results reported by Schulenburg et al. (2009) where biofilm accumulation increased both the heterogeneity and magnitude of the velocity field and

accumulation increased in the preferential flow paths. Our results suggest that biomass can be effective in altering pore morphology, and thus flow field, in porous media, a process that can increase oil recovery beyond what is predicted by capillary number increase alone.

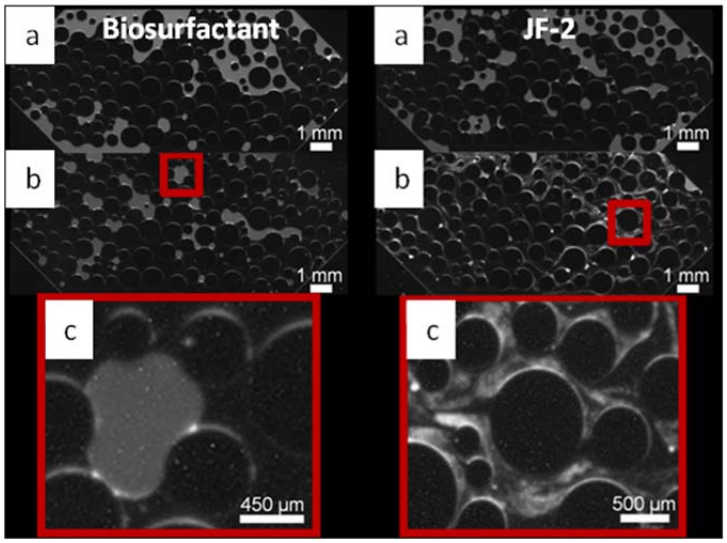

Figure 4.7: Biosurfactant flood (left) and JF-2 flood (right); (a) primary recovery, (b) residual oil saturation after enhanced recovery. Red box in (b) corresponds to enlarged region in (c). JF-2 biofilm can be seen in the right-hand column as dense streamlined gray matter (b) and(c).

Pore morphology change due to bioclogging could explain the *AOR* obtained with JF-2, and also explains why an apparently sparse MR-1 biofilm still recovered oil. However, results that contrast these findings were reported by Soudmand-asli et al. (2007) who studied MEOR in fractured porous media. Etched glass micromodels with a fractured network were used with both a biosurfactant-producing bacterium and an exopolymeric-producing bacterium. Results suggested that plugging of the matrix-fractures by exopolymeric substances inhibited oil recovery, resulting in the biosurfactant-producing bacterium outperforming the exopolymeric-producing bacterium. The results presented herein, in comparison to the findings of Soudmand-asli et al. (2007) suggest that the connectivity of fractures versus pores, and thus, pore morphology, could be a major controlling factor as to the effectiveness of bioclogging.

To further explore the differences between biotic and abiotic recovery, blob size distributions (BSD) were calculated and curve-fitted to the van Genuchten (1980) function (Figure 4.8 and 4.9 and the fitting parameters are reported in Table 4.2). MEOR treatment increased β and m (*Eq. 5.1*) indicating that mean blob size decreased and became more uniform than the initial BSD after primary recovery at $N_{ca} = 7.9x10^{-7}$. Furthermore, the BSD after MEOR is similar to the BSD obtained abiotically by increasing the capillary number (Figure 4.8 and 4.9). For instance, when bioclogging occurs the resulting BSD (Figure 4.8) is very similar to that obtained with flooding at $N_{ca} = 10^{-4}$ to 10^{-5} (Figure 4.9). In support of the BSD data, stereo microscope images show that after primary recovery, residual oil existed as large ganglia that spanned multiple pores (Figure 4.7a, left and right). After biosurfactant flooding (Figure 4.7b, left) large ganglia still existed, and after bioclogging (Figure 4.7b, right) only oil blobs residing in single pores remained. Similar quantitative observations of reduced oil blob size during MEOR and a comparison between the size distribution of residual blobs resulting from MEOR and those resulting from abiotic recovery have not been reported in the literature. Results indicate that, as with abiotic recovery, MEOR mobilizes the large residual oil ganglia. The mobilized ganglia are then either recovered from the micromodel or broken up into smaller multiple oil ganglia that are more uniform in size than residual oil globules after water flooding.

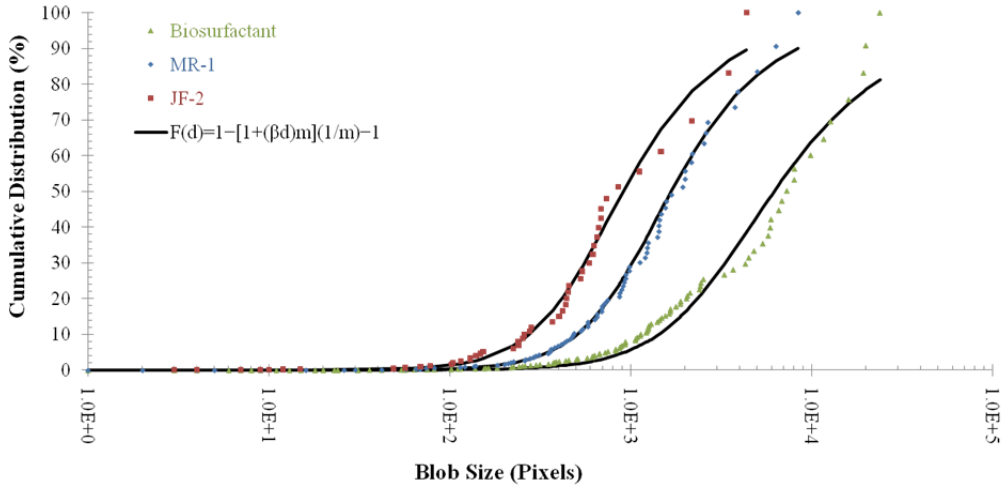

Figure 4.8: Blob size distributions for the MEOR experiments. Results are based on triplicate experiments.

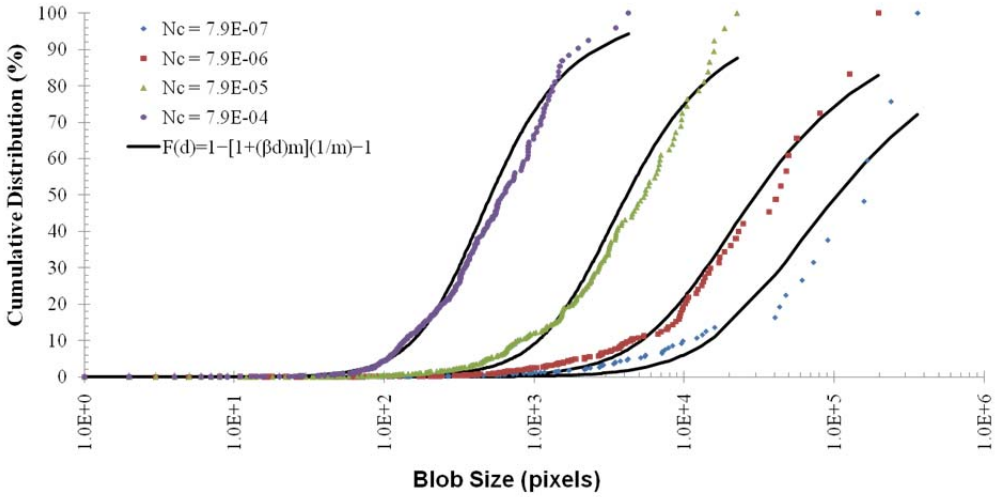

Figure 4.9: Blob size distributions for the abiotic experiments. Results are based on triplicate experiments.

Table 4.2: Fitting parameters for the Van Genuchten function. Results are based on triplicate experiments.

Flood	Parameters	
	β	m
Biosurfactant	3.37E-04	1.8
MR-1	9.67E-04	2.1
JF-2	1.78E-03	2.1
Nc = 7.9E-07	3.50E-05	1.5
Nc = 7.9E-06	9.51E-05	1.6
Nc = 7.9E-05	4.52E-04	1.9
Nc = 7.9E-04	3.15E-03	2.1

Microbial treatment in the $19^{\circ}\measuredangle$ micromodel shifted the radius or curvature distribution (RCD) to smaller and more uniform radii (Figure 4.10) than the initial RCD after primary recovery at $N_{ca} = 7.9 \times 10^{-7}$ (Figure 4.11). The largest RCD shift occurred when bioclogging and biosurfactant production occurred simultaneously (i.e. with JF-2, Figure 4.10). Again, biosurfactant flooding and bioclogging appear to have a similar effect on the RCD as increasing the capillary number under abiotic conditions where the RCD shifts to smaller and more uniform values. No negative radii of curvature were measured during the abiotic or

biotic experiments indicating that micromodel wettability remained mostly water-wet during microbial treatment. Researchers have reported that MEOR treatment can change the wettability of porous media using macro-scale indices, such as, the Amott, USBM, or Carter method (Donaldson et al. 1969; Amott 1959). After MEOR treatment with JF-2 the Amott wettability increased from -0.27 to -0.10 in initially oil-wet cores (Kianipey et al. 1989) and the USBM wettability method in water-wet cores showed that JF-2 shifted the wettability significantly in the positive direction toward a more water-wet condition up to a maximum of 0.99 (Donaldson et al. 1969). These results support our findings, since the curvature distributions prior to and after MEOR treatment are positive, indicating water-wet curvatures.

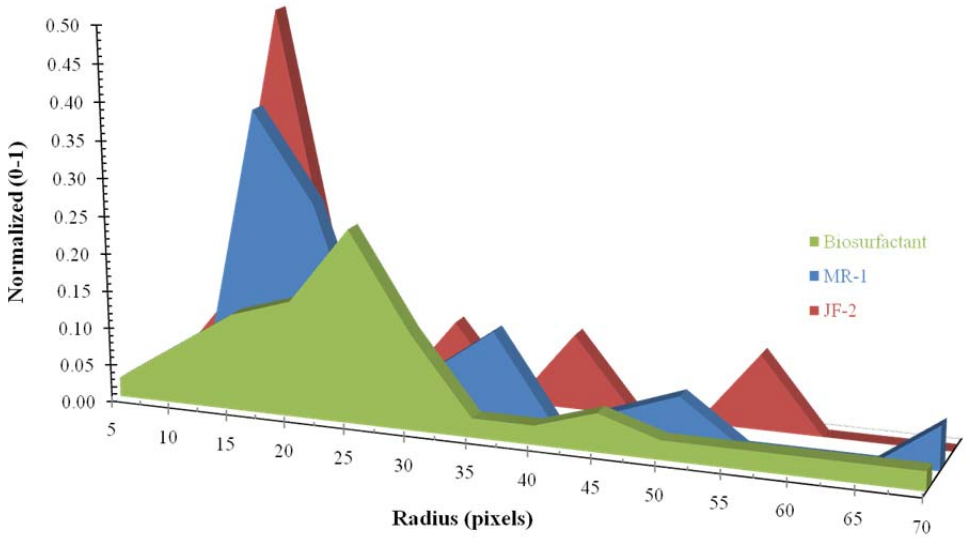

Figure 4.10: Radius of curvature for residual oil blobs after MEOR. Results are based on triplicate experiments and all of the measured radius of curvature for each experiment are reported.

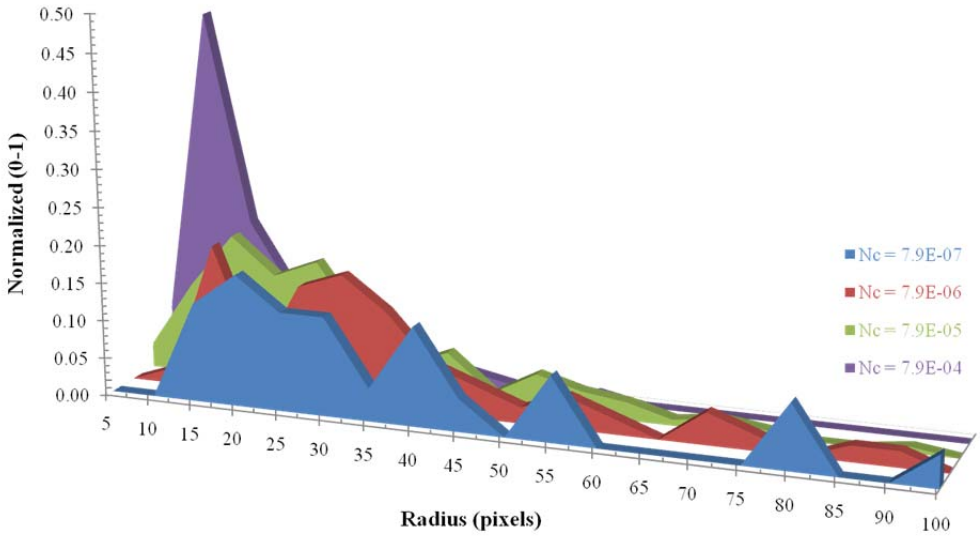

Figure 4.11: Radius of curvature for residual oil blobs after abiotic capillary desaturation experiments. Results are based on triplicate experiments and all of the measured radius of curvature for each experiment are reported.

Table 4.3: Curvature results for the MEOR and abiotic tests. Results are based on triplicate experiments.

Flood	Parameters	
	$R_{average}$	stdev
Biosurfactant	25.8	15.4
MR-1	23.6	15.3
JF-2	20.8	13.9
Nc = 7.9E-07	46.4	39.6
Nc = 7.9E-06	43.4	39.9
Nc = 7.9E-05	23.6	22.2
Nc = 7.9E-04	13.0	9.1

The utilization of bacteria for enhanced oil recovery was ultimately explained by capillary number effects, where changes in viscosity, pore velocity, and interfacial tension were mutually affected. Results indicate that abiotic and biotic oil recovery proceeded in an analogous manner according to the *AOR*, BSD, and RCD data. However, for combined

bioclogging and biosurfactant, capillary number could not fully explain recovery and it is assumed that a change in pore morphology, due to bioclogging, was responsible for the additional recovery. Additional oil recovery was optimal when both bioclogging and biosurfactant production occurred simultaneously; however, this finding is contingent on pore morphology and it is expected that in different porous networks the effectiveness of a given MEOR mechanism or combination thereof, may differ. To address the questions posed in the introduction; our results indicate that a metabolically stressed JF-2 culture is ideal for bioclogging and subsequent oil recovery and that dead inactive biomass cannot recover oil. For example, flooding with compromised bacteria suspended in a salt solution recovered no oil. Results further indicate that biosurfactant without biomass can recover oil, but recovery is dependent on wettability. Conversely, active bacterial biomass can recover oil, but the addition of a biosurfactant will improve recovery. The presented results explain the importance of bioclogging for oil recovery in a simple micromodel system. However, at the field-scale other complications, such as bioclogging around the wellbore, will ultimately arise and the deleterious effects of clogging need further investigation at that scale.

4.5 Conclusions

- *AOR* was optimal when bioclogging and biosurfactant production occurred simultaneously.

- JF-2 cultures under stress caused by nutrient limitation and/or environmental conditions were more efficient at bioclogging than JF-2 cultures under ideal growth conditions. This increased bioclogging is likely caused by the coagulation of cells during stress.

- MEOR was most effective under highly water-wet conditions.

- JF-2 treatment in the $19^{o}\measuredangle$ micromodel recovered the same amount of oil as its abiotic equivalent recovered at a capillary number of ~10^{-4} indicating that MEOR can replace water flooding at high flow rates and thus the associated pressure build-up.

- The change in BSD and RCD that occurred between water flooding and post MEOR in the $19^{o}\measuredangle$ micromodel resembled that which occurred under abiotic conditions as a result of brine flooding with increasing flow rate.

- During MEOR, large ganglia were broken up into smaller daughter ganglia that either became mobilized or trapped in single pores.

- Ganglia that spanned multiple pores still existed after biosurfactant treatment, but not after biosurfactant and bioclogging treatment.
- Biotic and abiotic oil mobilization proceeded in a similar manner (blob morphology and distributions changed analogously).
- The effectiveness of a given MEOR mechanism is likely dependent on pore morphology, in particular the connectivity beyond the clogged flow paths.

4.6 Acknowledgements

Acknowledgment is made to the donors of the American Chemical Society Petroleum Research Fund for support of this research (grant number 48505-AC9). Also, we thank Kendra Brown for designing the micromodels in CAD and for development of the microscope UV tracer method used in the presented experiments and Birdie Ciccarelli for help in the laboratory.

Chapter 5. Microbial Enhanced Oil Recovery in Fractional-Wet Systems: A Pore-Scale Investigation

Ryan T. Armstrong[1] and Dorthe Wildenschild[1]

3. School of Chemical, Biological, and Environmental Engineering, Oregon State University, 103 Gleeson Hall, Corvallis, OR 97331-2702

Transport in Porous Media
233 Spring Street, New York, NY 10013
Accepted 11/24/2011

5.1 Abstract

Microbial enhanced oil recovery (MEOR) is a technology that could potentially increase the tertiary recovery of oil from mature oil formations. However, the efficacy of this technology in fractional-wet systems is unknown and the mechanisms involved in oil mobilization therefore need further investigation. Our MEOR strategy consists of the injection of *ex situ* produced metabolic byproducts produced by *Bacillus mojavensis JF-2* (that lower interfacial tension via biosurfactant production) into fractional-wet cores containing residual oil. Two different MEOR flooding solutions were tested; one solution contained both microbes and metabolic byproducts while the other contained only the metabolic byproducts. The columns were imaged with x-ray computed microtomography (CMT) after water flooding, and after MEOR, which allowed for the evaluation of the pore-scale processes taking place during MEOR. Results indicate that the larger residual oil blobs and residual oil held under relatively low capillary pressures were the main fractions recovered during MEOR. Residual oil saturation, interfacial curvatures, and oil blob sizes were measured from the CMT images and used to develop a conceptual model for MEOR in fractional-wet systems. Overall, results indicate that MEOR was effective at recovering oil from fractional-wet systems with reported additional oil recovered (AOR) values between 44% and 80%; the highest AOR values were observed in the most oil-wet system.

5.2 Introduction

Microbial enhanced oil recovery (MEOR) is a tertiary oil recovery process where microorganisms and/or their metabolic byproducts are utilized for the mobilization of crude oil trapped in mature oil formations. The proposed MEOR mechanisms leading to oil recovery fall into two broad categories: (**Mechanism 1**) alteration of oil/water/rock interfacial properties and (**Mechanism 2**) changes in flow behavior due to bioclogging (Gray et al. 2008). Numerous reports show the efficacy of MEOR at the lab-scale (e.g. Soudmand-asli et al. 2007; Bordoloi et al. 2007; Suthar et al. 2008,2009; Yakimov et al. 1997; Bao et al. 2009), however, a complete understanding of the mechanisms involved is lacking and the effectiveness of each mechanism for different reservoir parameters (such as wettability) is unknown.

As stated by Youssef et al. (2009), three general strategies exist for the implementation of MEOR: (1) Injection of nutrients to stimulate indigenous microorganisms, (2) Injection of

exogenous microorganisms(s) and nutrients, or (3) Injection of *ex situ* produced products. The first two strategies have the added difficulty of dealing with subsurface bacterial transport, competition for nutrients among the desired organism and other indigenous microorganisms, and maintaining nutrient levels throughout a reservoir for extended periods of time (Gray et al. 2008). Therefore, it is likely that the third strategy is the simplest, and thus, the most likely for success at the field-scale. This third strategy is the approach used in the experiments presented here. In particular, we focus on the injection of *ex situ* generated products produced by *Bacillus mojavensis* JF-2 and the effect of these products on oil mobilization in fractional-wet systems.

Bacillus mojavensis JF-2 is a gram-positive, biosurfactant producing, facultative aerobe, isolated from oil reservoir brine in Oklahoma (Jenneman et al. 1983). As categorized above, the possible MEOR mechanisms associated with JF-2 include the following: reduction of interfacial tension via biosurfactant production (**Mechanism 1**), changes in wettability (**Mechanism 1**), and bioclogging (**Mechanism 2**). Mobilization of crude oil in a sand packed column after addition of JF-2 biosurfactant was initially demonstrated by Jenneman et al. (1983). Lin et al. (1993, 1994a, 1994b) studied the production of biosurfactant by JF-2 under anaerobic and aerobic conditions, biosurfactant structural characterization (i.e. the chemical structure of the biosurfactant), and biosurfactant yield. From these studies a growth medium, referred to as Media E, was formulated that optimizes biosurfactant production and therefore maximizes IFT reduction. Evidence of wettability alteration was reported by Kianipey et al. (1989) who found that for oil-wet flow cells where residual oil saturation decreased from 0.18 to 0.14, the Amott wettability indices (Amott, 1959) increased from -0.269 to -0.10 indicating more water-wet conditions after MEOR. Similar, for water-wet sandstone Chase et al. (1988) found that JF-2 shifted the USBM wettability indices (Donaldson et al. 1969) significantly in the positive direction towards a more water-wet condition. Currently, no literature exists on oil recovery with JF-2 via bioclogging. However, most organisms including JF-2 can form biofilm and the effect that biofilm formation can have on oil recovery should not be overlooked.

Wettability is a major factor controlling residual oil saturation, and thus, it is essential to characterize reservoir wettability (Tweheyo et al. 1999; Graue et al. 1999; Morrow and Mason 2001). Reservoir rock wettability can be altered by contact with absorbable crude oil components (e.g. asphaltenes) which can lead to heterogeneous forms of wettability

characterized by the term fractional wettability (Anderson et al. 1986). A fractional-wet system is where a portion of the reservoir rock is strongly oil-wet, while the rest is strongly water-wet (Salathiel 1973). Fractional-wet systems have previously been studied by packing columns with different ratios of water-wet sand and sand rendered oil-wet by treatment with an organic silane solution (Al-Raoush 2009; Han et al. 2006; Fatt et al. 1959). Fatt et al. (1959) found that nonuniform wettability can distort the capillary pressure curve such that it no longer represents the true pore-size distribution. The findings of Al-Raoush (2009) indicate that wettability can have a dramatic effect on residual oil entrapment. Residual oil blobs increase in size and length as the porous medium is comprised of fewer oil-wet surfaces. Additionally, simulation results using pore-network models developed by Zhao et al. (2010) support the experimental trends found by Al-Roush (2009). Using x-ray microtomography, Han et al. (2006) found that the distribution of residual water phase is less uniform in fractional-wet columns than water-wet columns and that fractional-wet columns contained fewer and larger residual water blobs. Kumar et al. (2008) developed a technique to modify the hydrophobicity of carbonate cores, such that, well-defined wettability states could be obtained. Pore-scale images acquired with CMT after spontaneous imbibition in the fractional-wet cores showed that the oil phase was concentrated in the larger, presumably oil-wet pores, suggesting that imbibition occurred preferentially through the water-wet regions (Kumar et al. 2008).

The effect microorganisms can have on wettability and approaches taken to understand such wettability alteration during MEOR vary in the literature. Traditionally, surface wettability has been quantified by placing a liquid drop on a solid surface and then measuring the resulting contact angle, known as the wetting angle which is defined by the Young-Laplace equation (Marmur et al. 2009). Other than directly measuring contact angle, porous media wettability is often quantified using macro-scale indices (obtained with techniques such as the Carter or Amott methods (Amott, 1959; Bobek et al. 1956)). Changes in these macro-scale indices due to microbial activity have been shown by Afrapoli et al. (2009) who found more water-wet conditions after MEOR using these measurements. However, the direction in which microorganisms change wettability is not consistent. For example, changes in surface wettability towards more water-wet conditions have been reported by Mu et al. (2002) while Polson et al. (2010) reported the opposite trend.

MEOR is a large-scale outcome driven by pore-scale processes. Therefore, to better understand the various MEOR mechanisms facilitating oil recovery, pore-scale investigations are needed. In particular, high resolution 3-dimensional images of the pore-space and the immiscible fluid distributions are needed to understand pore-scale temporal and spatial changes in interfacial curvature and oil blob morphology during MEOR. X-ray computed microtomography (CMT) has been available for more than three decades and has been a powerful tool for studying a wide array of multi-phase processes in porous media systems (e.g. Al-Raoush et al. 2009; Porter and Wildenschild 2010; Wildenschild et al. 2002). Using CMT numerous researchers have distinguished multiple fluids and their menisci, quantified interfacial areas (Culligan et al. 2004; Porter et al. 2009, 2010), and measured oil blob size distributions (e.g. Al-Raoush et al. 2005a, 2005b; Schnaar and Brusseau 2006; Karpyn et al. 2010). However, similar CMT analyses have not been applied to MEOR. Thus, it is unclear how MEOR affects interfacial curvature and residual oil blob morphology, both essential parameters needed for understanding and predicting the complex physical phenomena that occur during MEOR.

5.3 Materials and Methods

5.3.1 Experimental Overview

A total of 18 MEOR column experiments (and 2 control column experiments) were performed, 9 of which were treated with JF-2 while the remainder were treated with biosurfactant. Fractional-wet systems were generated by packing the CMT columns (I.D. = 6 mm, length = 60 mm) with three different ratios of oil-wet and water-wet glass beads. Each group of 9 was comprised of 3 replicates comprising 0% oil-wet, 25% oil-wet, and 50% oil-wet beads (percentages are by weight). Additionally, 2 control experiments were carried out using 0% oil-wet and 50% oil-wet beads. Columns were imaged once residual oil saturation was established after water flooding and after 84 hours, 140 hours, and 156 hours of MEOR. The control columns were imaged after 156 hours of water flooding (without MEOR).

Oil-wet beads were prepared by treating glass beads with a 5% octodecylthrichlorosilane (OTS) in toluene solution which is known to produce highly hydrophobic surfaces. The OTS treated beads were 500 to 600 µm in diameter and untreated beads (i.e. water-wet beads) were 1.0 to 1.2 mm in diameter which allowed for unique identification of the water-wet and oil-wet beads via size during image analysis. The 0% oil-wet bead pack was mixed using the

same glass bead size ratio as the 50% oil-wet bead pack to avoid differences in pore morphology. Naturally, in this case the smaller beads were not treated with OTS. Thus, differences seen between the 0% and 50% oil-wet bead packs are strictly due to wettability. However, slight differences in pore morphology between the 25% and 50% oil-wet bead packs may exist. The effect of pore morphology on water flooding and MEOR is an ongoing research focus of ours and will be reported on in a future manuscript.

5.3.2 Water Flooding

Prior to water flooding CMT columns were sterilized with 3 pore volumes of ethanol, and then rinsed with 3 pore volumes of Media E to remove any residual ethanol. The columns were then saturated with Soltrol 220 followed by water flooding with Media E. Water flooding was performed under fixed flux conditions at 0.18 ml/hr with a standard syringe pump. Once 3 pore volumes of Media E was pumped through a column it was assumed that residual oil saturation was established, and the column was imaged with CMT. At this stage, 6 replicates for each fractional wettability were tested (i.e. 0% oil-wet, 25% oil-wet, and 50% oil-wet) as well as the 2 control columns. After the columns had been imaged at residual oil saturation, MEOR commenced.

5.3.3 MEOR

Two different MEOR flooding solutions were used; one contained bacteria and their metabolic byproducts while the other contained only the metabolic byproducts (biosurfactant). The bacterium used was *Bacillus mojavensis* JF-2 (ATCC 39307). JF-2 was grown on Media E (Table 4.1**,** similar to Lin et al. 1993, 1994a, 1994b) at room temperature, under well-mixed conditions in a bioreactor and the content of this bioreactor was used as one of the two MEOR flooding solutions tested (bacteria and biosurfactant). The bioreactor contained 500 ml of Media E and was inoculated with 1 ml of concentrated cells grown up from a batch culture. During growth, pH and interfacial tension (IFT) were recorded and the reactor was visually inspected. Prior to the MEOR experiments, the growth curve for JF-2 was characterized under the same conditions as the MEOR experiment. The second MEOR flooding solution used was a biosurfactant solution which was prepared by separating the JF-2 biomass from spent bacterial cultures (i.e. after exponential growth). Bacterial cultures of JF-2 were centrifuged at 9,000 rpm for 10 minutes, followed by filtration of the supernatant through a 0.22 μm pore diameter membrane to remove the bacterial cells. The IFT of the

resulting biosurfactant solution was measured with a Du Noüy ring tensiometer and the same value as prior to biomass removal was obtained. Thus, the JF-2 and biosurfactant flooding solutions had similar IFT. However, with JF-2 treatment, bioclogging of the pore-space occurs, and thus, herein we compare IFT reduction with and without bioclogging.

5.3.4 Microtomography

Columns were imaged using synchrotron based x-ray microtomography at the GeoSoilEnviroCARS (GSECARS) 13-BM-D Beamline at the Advanced Photon Source, Argonne National Laboratory. The GSECARS bending magnet beam-line provides a fan-beam of high-brilliance radiation, collimated to a parallel beam with a vertical size of approximately 5 mm. Two images were collected and stacked in the vertical center of each column. Thus, only a 10 mm window in the vertical center of each column was imaged and analyzed to avoid any boundary effects that may occur at the column inlet and outlet. Cesium chloride was added as a contrast agent to the brine phase (1:6, CsCl:H_2O by wt.) prior to imaging (i.e. once either water flooding or MEOR treatment was complete). For water flooding, it was assumed that the CsCl was diluted from the column within the first few pore volumes during MEOR treatment. Images were collected at energies above and below the photoelectric edge for cesium (i.e. 36.885 keV and 35.085 keV). On-the-fly scanning, where the sample stage rotates continuously through 180° during data collection, reduced data collection time for a single scan to 5 minutes, which allowed for the collection of numerous data sets in our allotted beam time. For each scan, 720 projections were collected over 180° and the images were collected at a resolution of 11.3 µm/pixel after 2x binning of the data. The raw data (2D projections) were reconstructed to produce a 3D volume of gray-scale data using a filtered back-projection algorithm written in the programming language IDL™ (Research Systems Inc.).

5.3.5 Image Processing

Tomography volumes were segmented with the commercial software Avizo Fire® using a gradient-based watershed routine based on the approach by Sheppard et al. (2004). The principle of gradient-based watershed segmentation is to identify the known regions (i.e. internal regions of each phase) in an image using a simple threshold. The unknown regions (i.e. interfacial transition regions) are then identified by considering the image intensity

gradient, such that the transient between any two phases is found at the inflection point (i.e. the maximum of the first derivative of the image intensity) between any two known phases.

All images were median filtered (3x3x3) and arithmetic operations were performed on the above-the-edge and the below-the-edge images to help accentuate a given phase (i.e. oil, water, or glass beads). The median filtered above-the-edge image was used for calculating the image intensity gradient and thereby labeling voxels which represented the glass phase. Subtracting the above-the-edge image from the below-the-edge image increased the water phase signal, and thus, the resulting image was used to label all water phase voxels. Addition of the above-the-edge and the below-the-edge images decreased the noise in the oil phase and allowed for labeling of the oil phase voxels. Once the known regions were labeled, the watershed segmentation routine was implemented to classify the image into three distinct phases (i.e. oil, water, and glass). An example image from each step in the image segmentation process is provided in Figure 5.1.

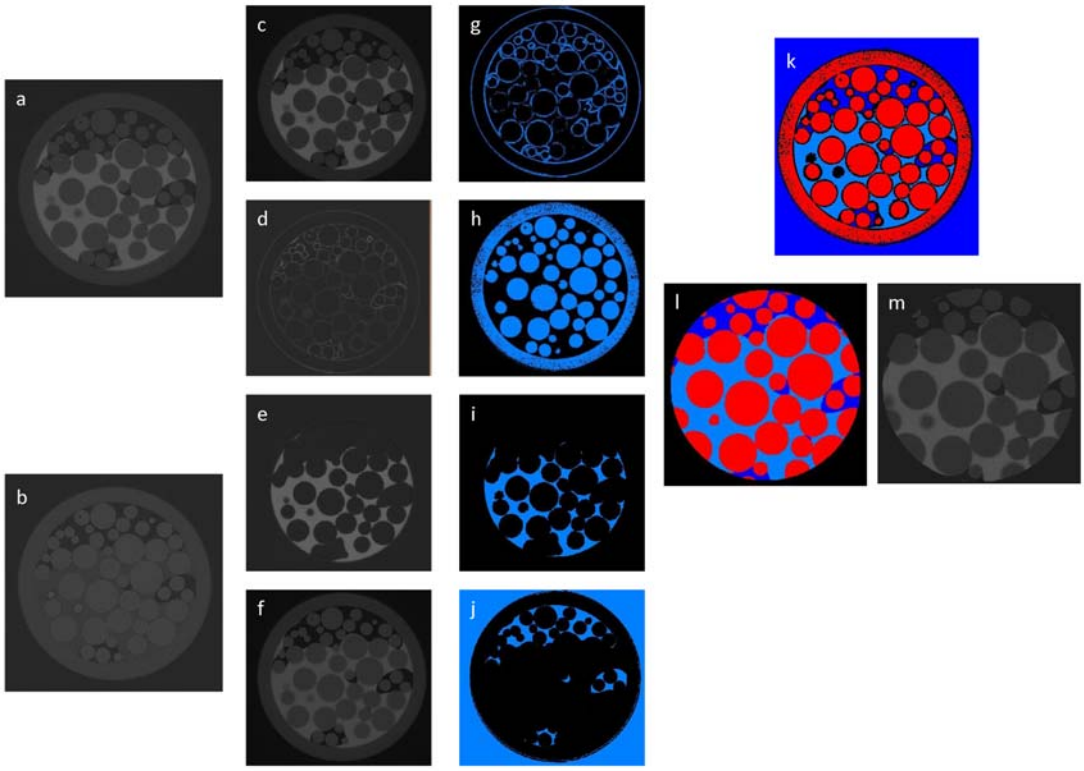

Figure 5.1: Example images taken during segmentation; above-the-edge gray-scale image (a), below-the-edge gray-scale image (b), median filtered (3x3x3) above-the-edge image (c), image intensity gradient (d), below-the-edge image subtracted from the above-the-edge image (e), addition of above-the-edge and below-the-edge images (f), threshold of the image intensity gradient (g), threshold of the bead phase (h), threshold of the water phase (i), threshold of the oil phase (j), addition of the threshold images (k), final cropped image after watershed routine (l), and original gray-scale image (m) cropped in the same region as the final segmented image (l).

5.3.6 Residual Oil Morphology

The segmented images were used to characterize residual oil blob size, oil saturation, and interfacial curvature. Oil blobs were individually labeled using a neighborhood voxel connectivity of 26 (i.e. voxels are connected if their faces, edges, or corners touch, and thus, the number of oil blobs found is more conservative then if a connectivity of 18 or 6 is used). Oil blob size was computed as the total number of voxels in each disconnected oil blob. Residual oil saturation was also calculated by voxel counting and used to report changes in oil saturation during MEOR.

Isosurfaces of the oil phase, the water phase, and the oil/water interface were created using a standard marching cube algorithm. The oil/water interface isosurface was used for calculating mean radius of curvature which is the inverse of mean curvature. To avoid pixilation effects, the oil/water interface isosurface was smoothed prior to computing interfacial curvature and curvature for each triangular element on the isosurface was averaged over its common neighbors.

To validate the curvature calculation method, precision dry beads (0.8 mm ± 0.1 mm) were imaged at similar resolution as the MEOR images collected herein (11.8 μm/pixel) and the radius of curvature of these beads were calculated from the segmented image. The calculated radius of curvature value was found to be within 5% of the true bead radius. Radius of curvature (i.e. the inverse of mean curvature) is measured from the perspective of the water phase, thus, a convex interface is reported as a negative radius of curvature value (implying water-wet conditions) while a concave interface is reported as a positive radius of curvature (implying oil-wet conditions).

5.4 Results and Discussion

Prior growth curve results for JF-2 show that after ~20 hours the bacteria stop doubling and go into a self-maintenance stationary phase (Online Resource 5). Both pH and IFT was monitored in the bioreactor for the duration of the MEOR experiment. Results show that during the first ~20 hours, a rapid drop in pH and IFT occurs (Figure 5.2), indicating that both fermentation and biosurfactant production are occurring. The pH reduction can be explained by fermentative respiration of the organism which creates excess protons and fatty acids in the growth media which reduce pH. The composition of these fermentation byproducts was partially characterized by Javaheri et al. (1985) where the main fermentation byproduct was identified as acetate with no detection of methanol, ethanol, propanol, or butanol during fermentation. However, the exact composition of the metabolic byproducts produced by JF-2 during fermentation has not been characterized. Apart from biosurfactant (which is not a strictly fermentative byproduct) it is unclear if other compounds produced during fermentation are essential for oil recovery.

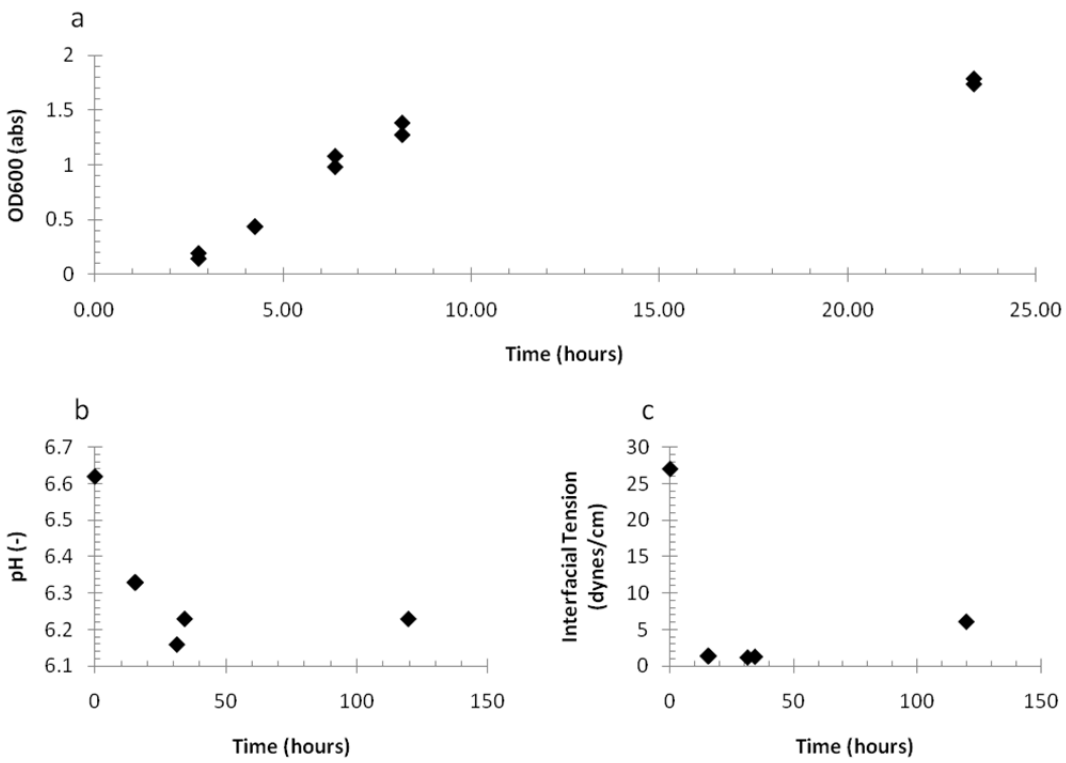

Figure 5.2: Growth curve for JF-2 (a), pH data for JF-2 flooding solution as a function of time during MEOR (b), and IFT data for the JF-2 flooding solution as a function of time during MEOR (c).

Oil recovery versus time for MEOR using either the JF-2 or biosurfactant flooding solutions are shown in Figure 5.3. Residual oil saturations reported at 0 hours correspond to oil saturations measured after water flooding as averages of 6 replicate columns, and the error bars correspond to a confidence interval of 90%. Residual oil saturation values reported at times >0 hours are average values of two different regions in the same column, and thus, no error bars are associated with these data points. Results show that the majority of oil recovery occurred in the first ~80 hours while only marginal recovery occurred over the remainder of time. The 50% oil-wet columns had the largest residual oil saturations after water flooding while the 0% oil-wet columns had the lowest residual oil saturations after water flooding. However, after MEOR, residual oil saturations for all of the columns approached a similar level. The control columns, as expected, showed essentially no change in residual oil saturation over the duration of the test, demonstrating that the oil recovery observed in the MEOR columns was in fact due to flooding with bacteria and/or their metabolic byproducts (i.e. biosurfactant).

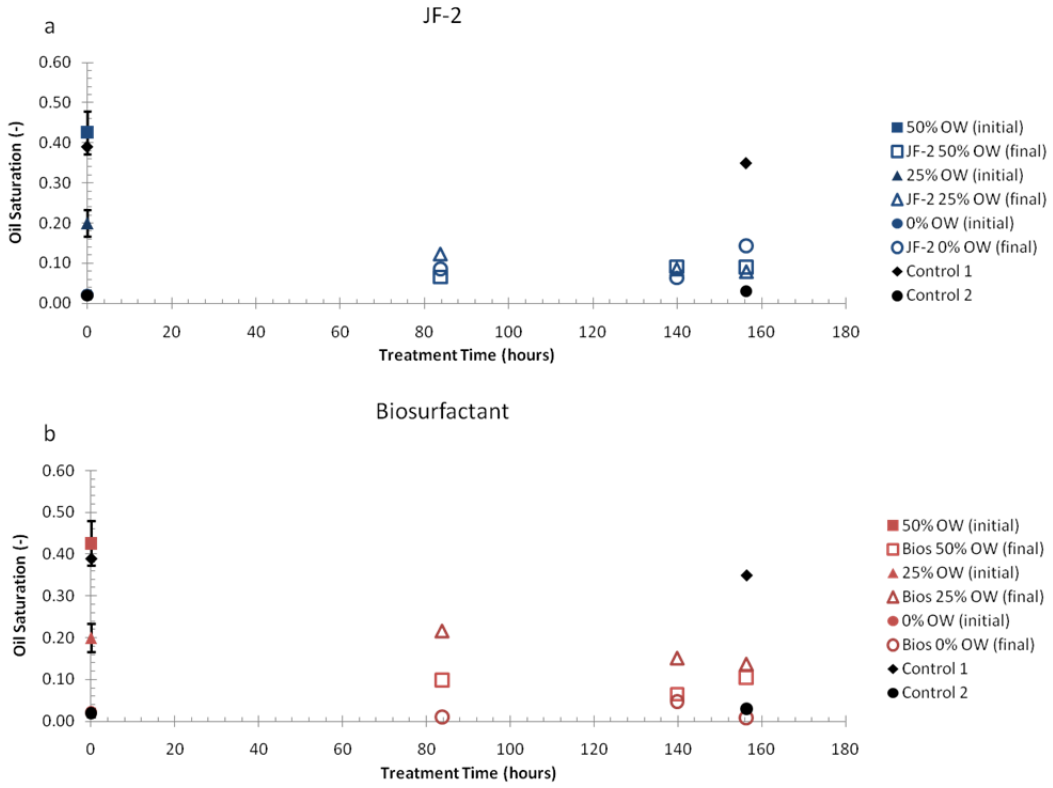

Figure 5.3: Residual oil saturation (calculated from the CMT images) versus treatment time for JF-2 MEOR (a) and biosurfactant MEOR (b). Data points at 0 hours represent the average oil saturation value measured directly after water flooding from 6 replicate columns for each wettability tested. Data points at 84, 140, and 156 hours represent the average oil saturation value measured at two separate locations in the same column during MEOR. Oil saturation error bars at 0 hours (i.e. directly after water flooding) correspond to a confidence interval of 90%.

Additional Oil Recovered (AOR) values are shown in Table 5.1.The results show that the overall effectiveness, in terms of AOR, for the flooding solutions tested were quite similar. AOR results for the 0% oil-wet columns are reported as n/a in Table 5.1 since residual oil saturations after MEOR treatment were slightly higher in these columns than after water flooding. It is likely that residual oil upstream from the imaged volume was mobilized into the imaged volume causing these spurious results in the water-wet columns. This would obviously also be likely to happen during MEOR in the fractional-wet columns, but the effect is masked by the overall larger recovery in these columns. It is expected that if larger

volumes were imaged, reasonable AOR values would have been obtained for the 0% oil-wet columns as well. However, since residual oil saturations in the control columns remained constant during the experiments, this suggests that the pumping of three pore volumes during water flooding was sufficient for obtaining residual oil saturation. Thus, the spurious AOR results in the 0% oil-wet columns were not due to premature discontinuation of the water flood.

Table 5.1: Additional oil recovered (*AOR*) for the MEOR columns.

Treatment	**JF-2**	**Biosurfactant**
Fractional oil-wet	***AOR***	***AOR***
50%	79.2	73.7
25%	51.1	44.0
0%	n/a	n/a

To better understand what drives oil mobilization, oil/water interfacial mean curvature (reported as mean radius of curvature) was analyzed after water flooding and after MEOR. The mean radius of curvature values for the columns treated with either the JF-2 or biosurfactant flooding solutions are shown in Figure 5.4a and 5.4b. Considering that grain diameter (0.50-1.20 mm diameter) is a reasonable proxy to pore radius (0.25-0.60 mm) the reported mean radius of curvature values (0.23-0.34 mm) appear reasonable for these experiment. After water flooding, the smallest average radius of curvature value was observed in the 0% oil-wet columns, while the fractional-wet columns had consistently larger average radius of curvature values. These results suggest that the surface tension between the oil and the oil-wet bead surfaces may play a role in trapping since different mean radius of curvature values (and residual oil saturations) exist depending on the fraction of oil-wet surfaces that are present in the porous bead pack. Similar results are shown by Motealleh et al. (2010) were their grain-based pore-scale model demonstrated that the existence of a single oil-wet grain in the model domain can change trapped phase topology and that in a fractional-wet system the range of stable curvatures decreases and tends toward larger radius of curvatures.

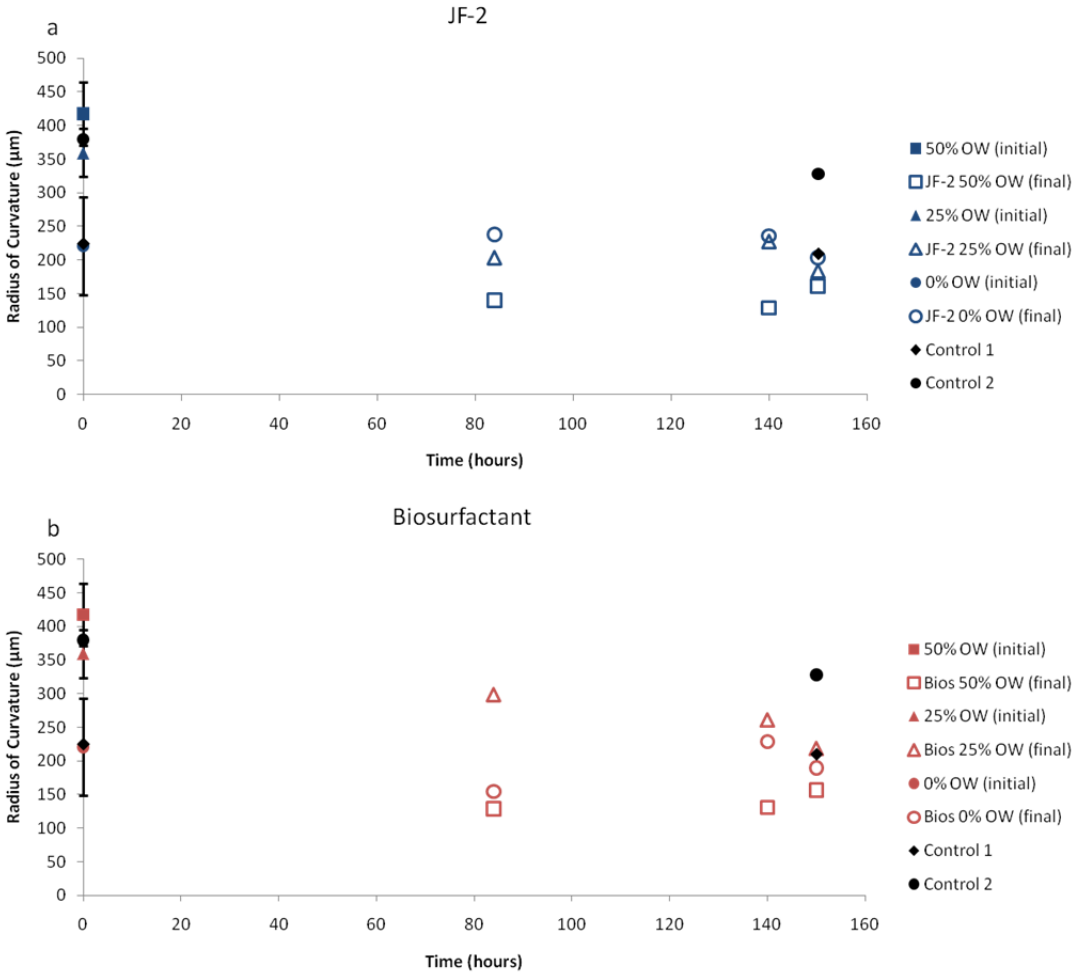

Figure 5.4: Average mean radius of curvature (calculated from the CMT images) versus treatment time for JF-2 MEOR (a) and biosurfactant MEOR (b). Data points at 0 hours represent the mean radius of curvature value taken directly after water flooding from 6 replicate columns for each wettability tested. Data points at 84, 140, and 156 hours represent the mean radius of curvature value taken from two separate locations in the same column during MEOR. Oil saturation error bars at 0 hours (i.e. directly after water flooding) correspond to a confidence interval of 90%.

It should be noted, that during MEOR, residual oil saturation and radius of curvature values in the 25% oil-wet columns are consistently above the 50% oil-wet columns. Potentially, this could be explained in terms of percolation where the 50% oil-wet columns have enough interconnected oil-wet pores to percolate across the column causing lower residual oil saturations. This can be demonstrated by generating a distance map of the pore space with

respect to the water-wet surfaces. Once again assuming that the average pore radius is approximately 0.25 mm and then removing any pore space that is within 1 pore radii distance of a water-wet surface, a volume rendering of the most oil-wet regions in the pore space can be created (Figure 5.5). As evident in Figure 5.5, the 50% oil-wet column has interconnected oil-wet regions from the top to the bottom of the imaged volume, while the 25% oil-wet column has no interconnected oil-wet regions. This interconnectedness is critical for mobilization, as pore-network models by Man et al. (2002) have demonstrated, that oil located in oil-wet pores surrounded by water-wet pores cannot escape and thus becomes trapped during imbibition. Also, as fractional wettability increases, residual oil saturation begins to decrease since oil-wet percolation networks become established across the model domain.

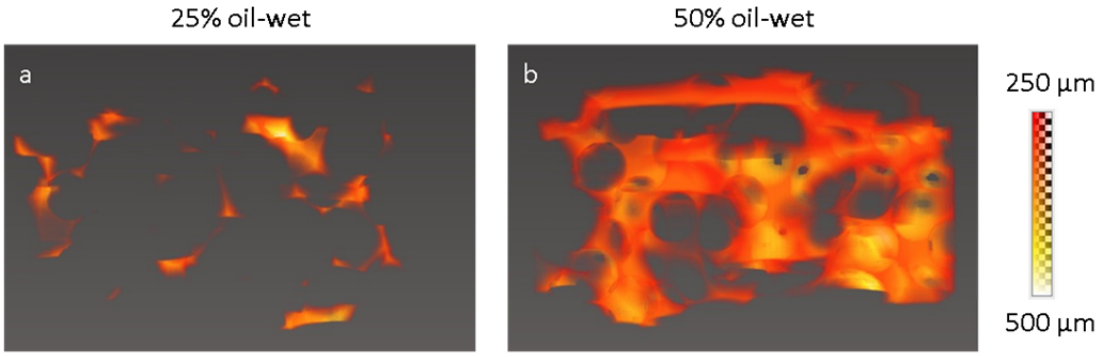

Figure 5.5: A distance map of the pore space relative to the water-wet surfaces for the 25% oil-wet (a) and 50% oil-wet (b) columns. Any pore space that is within 1 pore radii distance (i.e. 0.25 mm) of a water-wet bead is removed from the volume rendering.

The presence of bacterial cells in the flooding solution had little effect on interfacial curvature (Figure 5.4a and 5.4b). However, this may be a result of using metabolically inactive bacterial cells during flooding since it is unclear if metabolically active bacteria are required or not for interfacial attachment. Thus, different results may occur depending on the MEOR strategy taken: (1) injection of nutrients to stimulate indigenous microorganisms, (2) injection of exogenous microorganisms(s) and nutrients, or (3) injection of *ex situ* produced products. In general, after MEOR, mean interfacial radius of curvature decreases (Figure 5.4a and 5.4b). This decrease in mean radius of curvature after MEOR suggests that the remaining residual oil is strongly trapped in the smallest pores and that during MEOR,

mainly residual oil blobs held under relatively low capillary pressure (i.e. large radius of curvature) are being mobilized. Oil/water interfacial isosurfaces after MEOR treatment show that the remaining residual oil is indeed trapped mostly in oil-wet pore necks since mostly positive (i.e. oil-wet curvatures) are seen in the imaged regions, and in some cases, the residual oil exist as pendular rings (Figure 5.6). When comparing images of the oil/water interfaces after water flooding and after MEOR in Figure 5.6**,** it is apparent that in the fractional-wet columns interfacial curvature shifts towards more positive values indicating more oil-wet curvatures. This shift in curvature is not seen in the 0% oil-wet columns (Figure 5.6c1 and 5.6c2). These images further suggest that during water flooding, the oil-wet regions of the bead pack do not drain since mostly water-wet curvatures are present. Not until after MEOR, when interfacial tension was reduced, do the oil-wet regions drain as indicated by the presence of oil-wet curvatures. Figure 5.6 also illustrates distinct differences in the oil-water interface morphology from post water flood to post MEOR for fractional-wet systems.

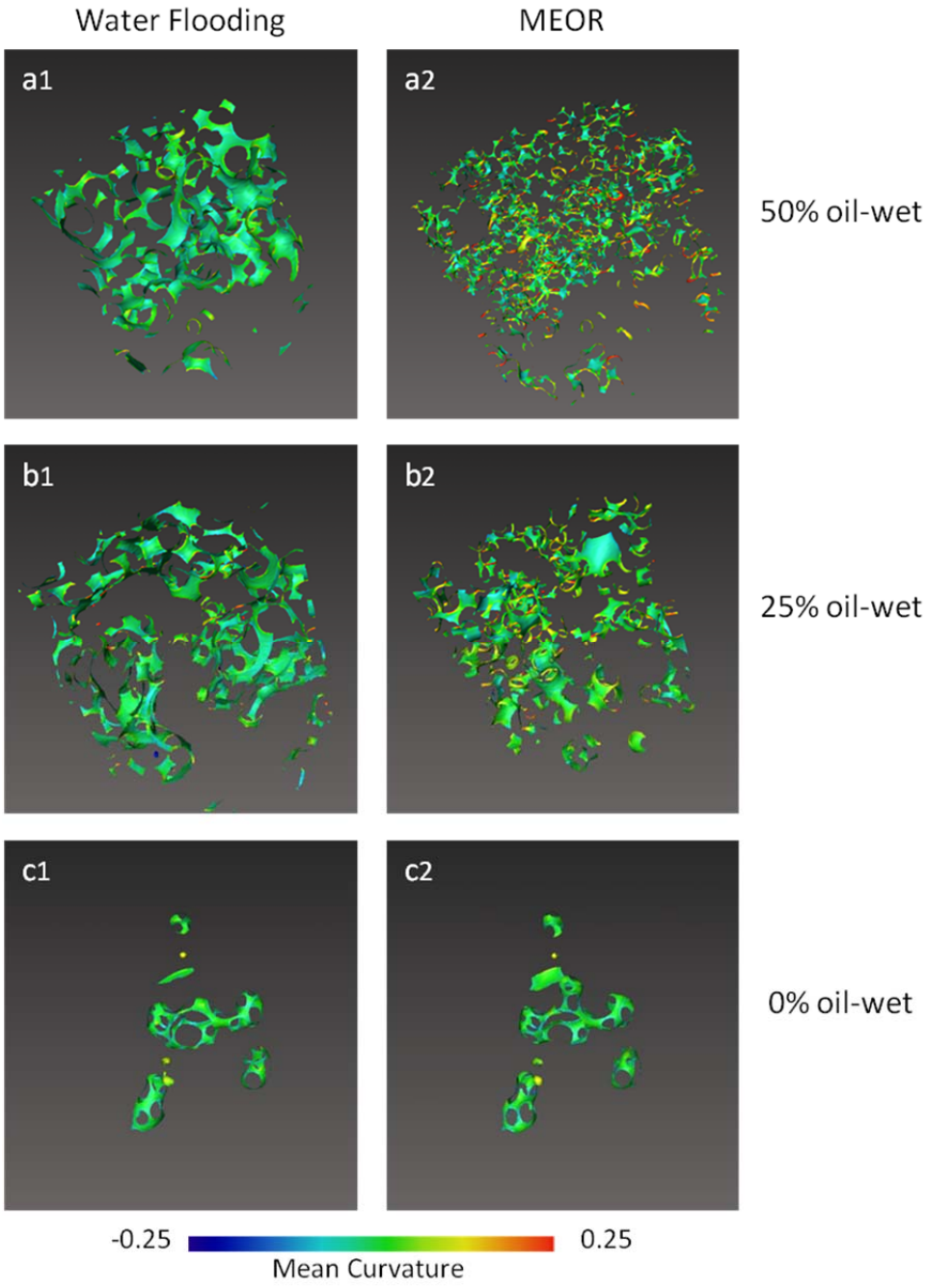

Figure 5.6: Example isosurfaces of the oil/water interface after water flooding (a1, b1, and c1) and after MEOR (a2, b2, and c2) for the 50% oil-wet (a1 and a2), 25% oil-wet (b1 and b2), and 0% oil-wet (c1 and c2) columns. From the perspective of the water phase, negative mean curvature values correspond to convex interfaces (i.e. water-wet curvature) and positive mean curvature values correspond to concave interfaces (i.e. oil-wet curvature).

The residual oil blob size distributions for MEOR columns flooded using the JF-2 or biosurfactant flooding solutions are shown in Figure 5.7a and 5.7b, respectively. These distributions demonstrate that after water flooding, residual oil blob size decreases consistently as the number of oil-wet surfaces decreases and that residual oil blob size distributions shift to smaller blob sizes after MEOR. These observations are supported by the results of Han et al. (2006) where fractional-wet columns contained fewer and larger residual phase. These results suggests that during MEOR the largest oil blobs are mobilized and/or broken up into smaller residual blobs that remain trapped in the pore-space. These results are consistent with the results of Payatakes et al. (1980) and Wardlaw et al. (1985) where residual oil blob size decreased as capillary number increased. The blob size distributions for JF-2 MEOR appear to be less dependent upon wettability than for biosurfactant MEOR, since the JF-2 flooding solution final blob size distributions are quite similar for the fractional wettabilities tested. Comparing blob size distribution and fractional wettability for JF-2 MEOR and biosurfactant MEOR, we see conflicting trends (Figure 5.7). This suggests that the presence of bacterial cells in the flooding solution may have an effect on the morphology of residual oil blobs; however, little difference is seen in the overall recovery of oil (Table 5.1). Visual inspection of the CMT images captured after MEOR indicate that the smaller trapped residual oil blobs are primarily located in oil-wet pores (Figure 5.8) which is also supported by the curvature results. In Figure 5.8 the water-wet beads are significantly larger than the oil-wet beads and can be visually identified. These images show that during water flooding, preferential flow paths developed through the water-wet pores and that a portion of the oil-wet pores drained after MEOR, however, residual oil still remained in the smallest oil-wet pore regions.

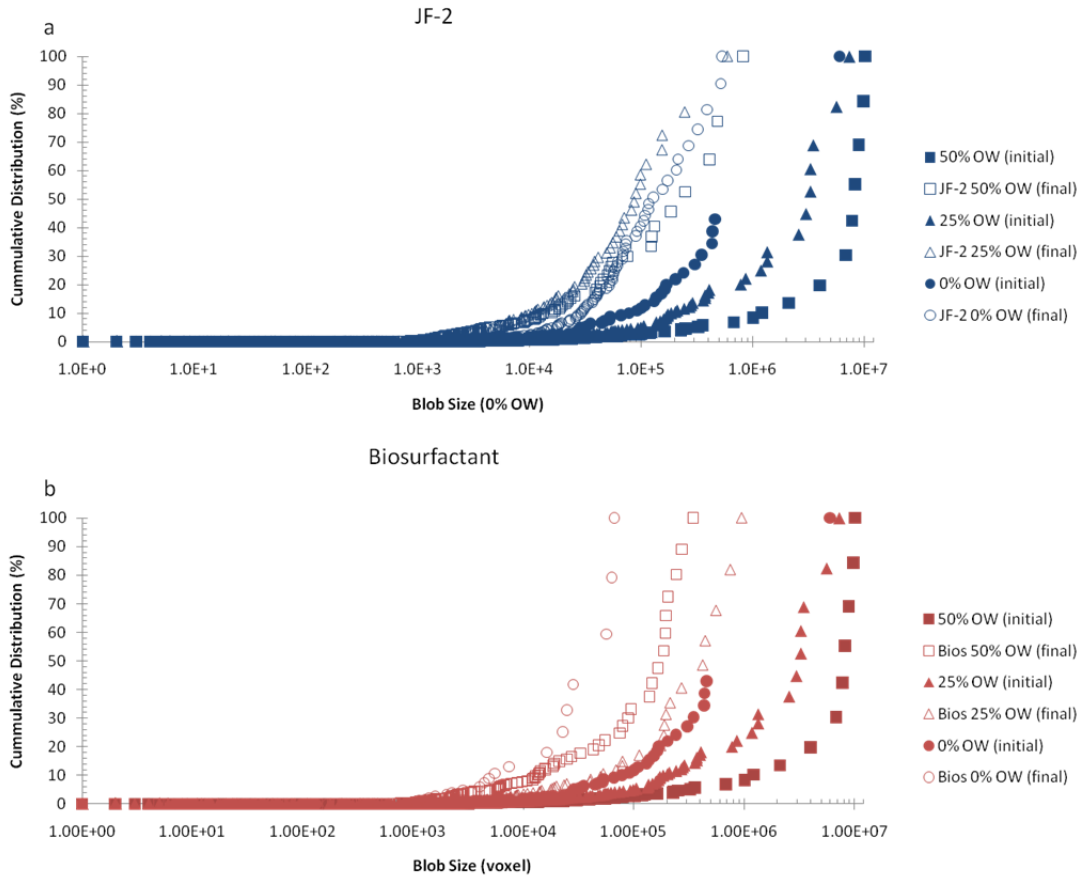

Figure 5.7: Residual oil blob size distributions for JF-2 MEOR (a) and biosurfactant MEOR (b). Solid data points correspond to blob size distributions taken directly after water flooding the wettabilities tested while the hollow data points correspond to the blob size distribution after 156 hours of MEOR for each wettability tested.

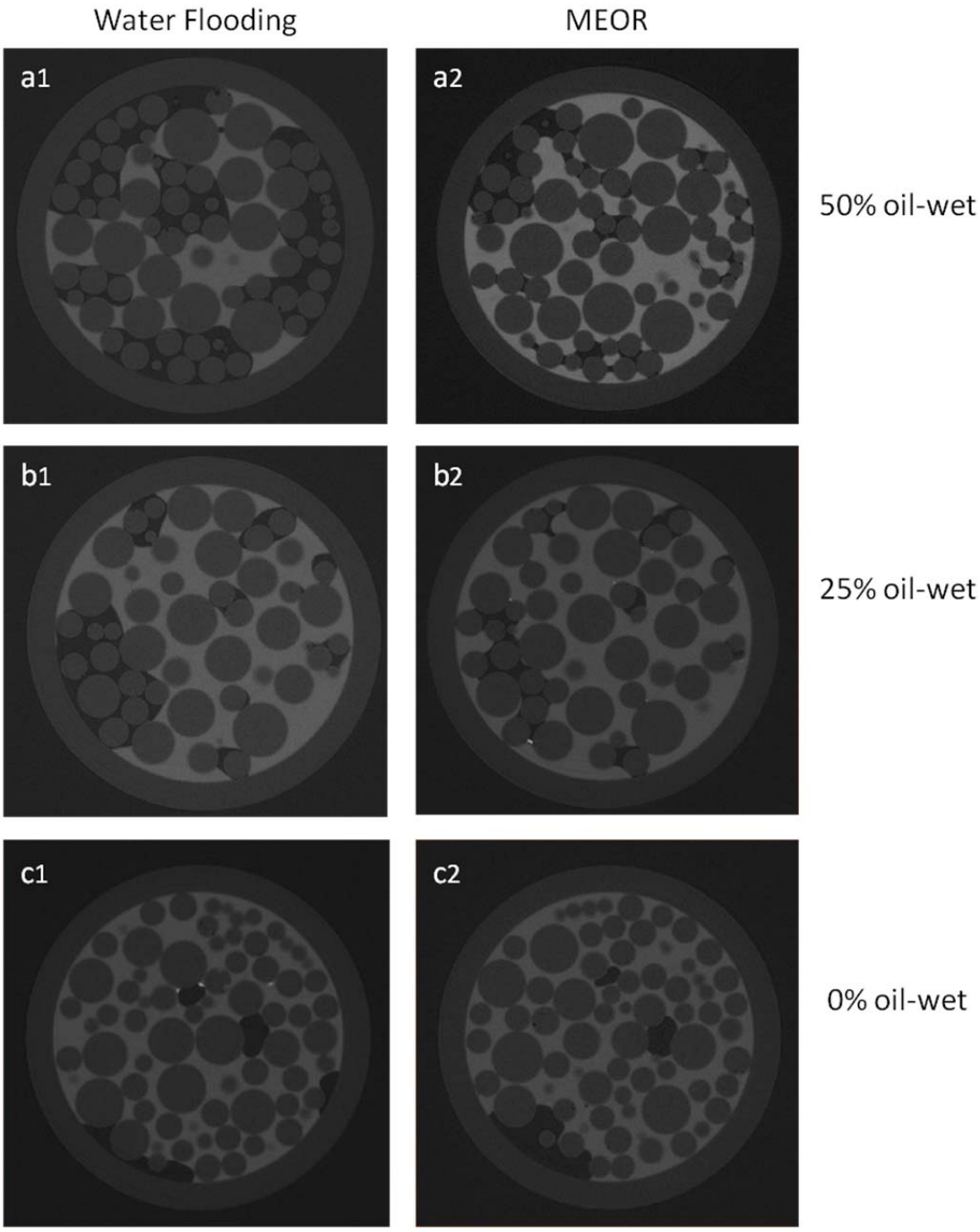

Figure 5.8: CMT images after water flooding (a1, b1, and c1) and after MEOR (a2, b2, and c2) for the 50% oil-wet (a1 and a2), 25% oil-wet (b1 and b2), and 0% oil-wet (c1 and c2) columns. In these images the brightest phase is water and the darkest phase is oil. Additionally, in the 50% oil-wet (a1 and a2) and the 25% oil-wet (b1 and b2) columns the smaller beads are oil-wet while the larger beads are water-wet.

The relationship between average residual oil blob size and the fraction of oil-wet surfaces in a column is shown in Figure 5.9a and 5.9b. The experimental results show opposite trends post water flooding and post MEOR. After water flooding our experimental results contradict experimental and pore-network model simulations reported in the literature. Both Al-Raoush et al. (2009) and Zhao et al. (2010) report that residual oil saturation and residual oil blob size decreases with increasing percentage of oil-wet surfaces in a porous medium. However, the capillary number in the Al-Raoush et al. (2009) experiment is two orders of magnitude higher than our capillary number ($1.6*10^{-8}$) during water flooding. During MEOR, the capillary number in our experiments increases by one order of magnitude due to interfacial tension reduction at which point we obtain a similar trend as Al-Raoush et al. (2009). This finding suggests that the relationship between residual oil blob size (and the amount of oil recovered) and fractional wettability is not universal and could be dependent on the interplay between viscous and interfacial forces (i.e. capillary number).

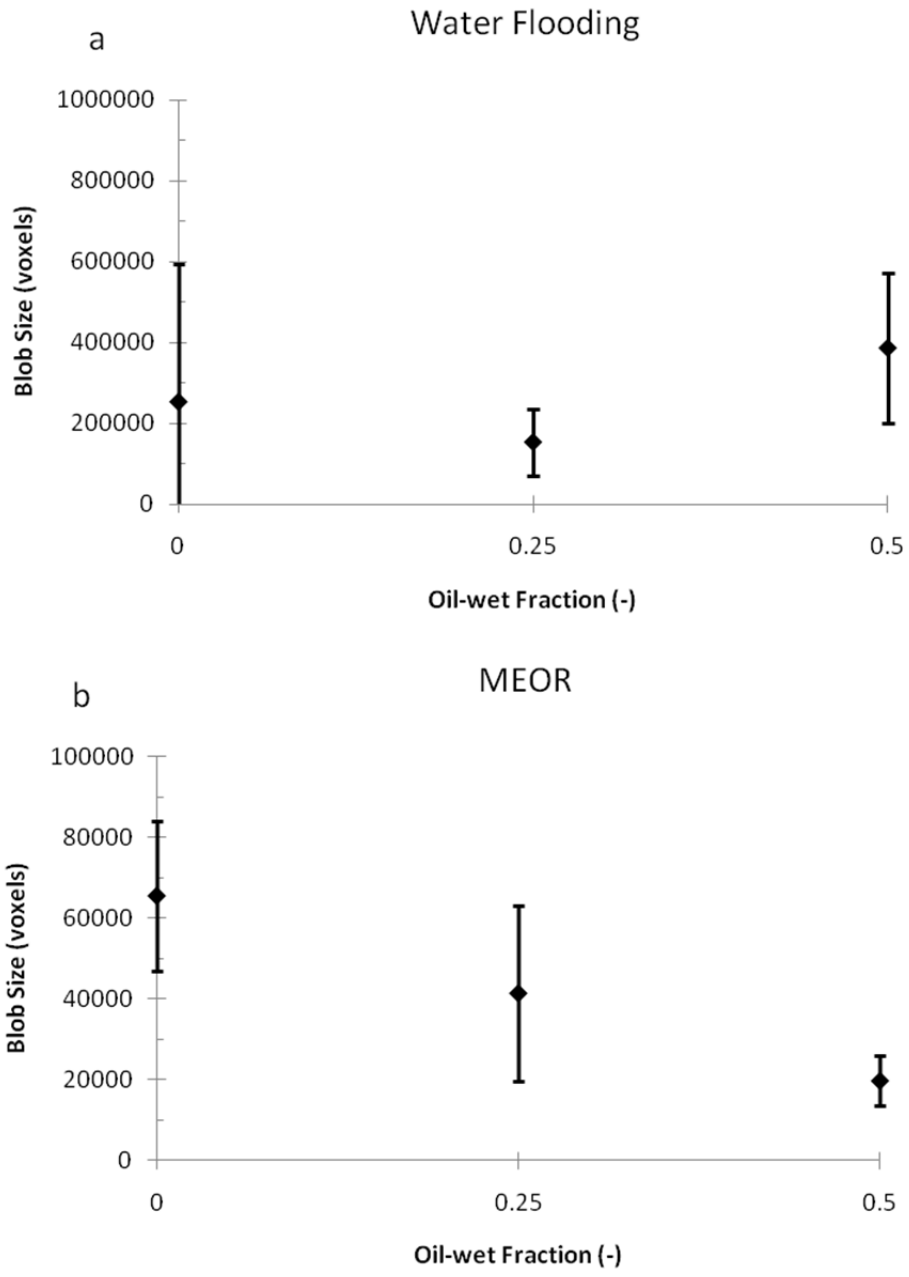

Figure 5.9: Average residual oil blob size versus the fraction of oil-wet surfaces present in a porous medium directly after water flooding (a) and after MEOR (b). Notice difference in scale on y-axis.

Based on the presented results we are able to suggest a conceptual model and summarize the prevalent mechanisms that control water flooding and MEOR in our fractional-wet systems. Each porous medium can be divided into 2 domains: (1) a water-wet domain and (2) a oil-wet domain. During water flooding the water-wet domain proceeds through dynamic forced imbibition where either snap-off or frontal displacement can occur, while the oil-wet domain proceeds through dynamic forced drainage where an entry pressure must be overcome before drainage can occur. At low capillary number the oil-wet domain does not drain since viscous forces are not large enough to overcome the entry pressure required to flood the oil-wet domain. Thus, flooding proceeds through the water-wet domain resulting in; (1) large residual oil blobs, (2) mostly water-wet curvatures, and (3) large interfacial radius of curvature. Simulation results presented by Motealleh et al. (2010) where menisci movement in fractional-wet media was investigated show that advancement of the water phase toward the oil-phase during imbibition can be impeded by the presence of an oil-wet grain, which is consistent with our experimental results at low capillary number (i.e. during water flooding). At higher capillary number (e.g. during MEOR through a reduction in IFT) the oil-wet domain drains and flooding proceeds through both the water-wet and oil-wet domains. Thus, reduction in interfacial tension reduced the entry pressure needed to initiate drainage of the oil-wet pores resulting in; (1) small residual oil blobs, (2) more oil-wet curvatures, and (3) a decrease in interfacial radius of curvature.

5.5 Conclusions

The implication of these results for field-scale MEOR operations is that oil reservoirs with a large fraction of oil-wet pores could potentially contain a large quantity of oil trapped in the oil-wet pore space. If that is the case, the type of MEOR that induces interfacial tension reduction as shown here could be quite successful in mobilizing this oil fraction. Our results show that, in porous systems that have large interconnected regions of oil-wet pore space, MEOR treatment is most successful because these interconnected regions can potentially support percolation of the oil phase.

As reported, no detrimental or beneficial effects are reported for JF-2 treatments were bioclogging of the pore space could occur. Thus, no complicated *in situ* treatment is needed. The bacterial flooding solution could be produced *ex situ* of the oil reservoir and then directly injected into the oil formation without the removal of biomass from the injection solution.

The effect of reservoir pore morphology on MEOR efficiency is the focus of on-going research and will be reported in a subsequent publication.

Overall conclusions:

- Post water flooding, fluid-fluid interfaces are located in mostly fractional-wet pores (i.e. pores surrounded by oil-wet and water-wet grains) as indicated by large interfacial radius of curvatures (i.e. rather flat interfaces) and visually identified in the CMT images.
- Post MEOR, oil-wet curvatures were measured in the 25% and 50% oil-wet columns, suggesting that residual oil was trapped in purely oil-wet pores.
- The ability to measure interfacial curvature from CMT images allowed us to study oil blob mobilization, in terms of interfacial curvature. Both types of MEOR decreased interfacial radius of curvature, which indicates that the oil recovered via MEOR is the fraction that is held in low capillary pressure pore geometries.
- As expected the trend in residual oil blob size with fractional wettability appears to be dependent on capillary number. However, the spatial location of residual oil blobs in fractional-wet systems at high capillary number differs from that obtained in water-wet systems. In fractional-wet systems, residual oil remains as pendular rings, once the oil-wet region drains.
- The JF-2 flooding solution and the biosurfactant flooding solution produced similar radius of curvature distributions and slightly different blob size distributions. The similarity in oil blob morphologies during either treatment was unexpected since it was expected that bioclogging with IFT reduction would significantly alter oil blob morphology in comparison to just IFT reduction.

5.6 Acknowledgments

Acknowledgment is made to the Donors of the American Chemical Society Petroleum Research Fund for support of this research (grant number 48505-AC9). Microtomography was performed at GeoSoilEnviroCARS (Sector 13), Advanced Photon Source (APS), Argonne National Laboratory. GeoSoilEnviroCARS is supported by the National Science Foundation-

Earth Sciences (EAR-0217473), Dept. of Energy-Geosciences (DE-FG01-94ER14466) and the State of Illinois. We wish to thank: Gabriel Iltis (Oregon State University), Yohan Davit (Université de Toulouse), James Connolly (Montana State University), and Mark Rivers (GeoSoilEnviroCARS) for help with imaging at the APS.

Chapter 6. Impact of Pore Morphology on Biosurfactant-Based Microbial Enhanced Oil Recovery

Ryan T. Armstrong[1], Brian K. Bay[2], and Dorthe Wildenschild[1]

1. School of Chemical, Biological, and Environmental Engineering, Oregon State University, 103 Gleeson Hall, Corvallis, OR 97331-2702

2. Mechanical, Industrial, and Manufacturing Engineering, Oregon State University, Dearborn Hall, Corvallis, OR 97332-2702

Journal of Petroleum Science and Engineering
233 Spring Street, New York, NY 10013
Submittal expected 2/1/2012

6.1 Abstract

Microorganisms can be utilized to mobilize capillary trapped oil in a process called microbial enhanced oil recovery (MEOR), in which numerous MEOR mechanisms are proposed. In this study, we explore the effectiveness of the MEOR mechanism of interfacial tension (IFT) reduction with and without the MEOR mechanism of bioclogging in a range of different pore morphologies using x-ray microtomography. The objective of this research is to distinguish what pore morphological parameters are of importance when considering biosurfactant-facilitated and/or biomass-facilitated MEOR. Additional oil recovered (*AOR*) is related to pore morphological parameters, including; porosity, coordination number, pore throat/body size, and sphericity. Results demonstrate that *AOR* increased from ~ 40% to ~60% with increasing pore throat size from 50 µm to 125 µm, grain sphericity from 0.1 to 0.28, and coordination number from 3.4 to 4.1, and with decreasing porosity from 0.4 to 0.1 and aspect ratio from 0.6 to 0.4. Both MEOR treatment options produce similar *AOR* results for the majority of pore morphologies tested. However, in terms of *AOR*, bioclogging out-performs IFT reduction by ~30% in the pore morphology with the highest porosity, largest aspect ratio, and lowest grain sphericity. Overall, the presented experiments demonstrate the importance of pore morphology, and thus residual oil blob morphology on the resulting effectiveness of MEOR.

6.2 Introduction

Microbial enhanced oil recovery (MEOR) involves inoculating an oil reservoir with exogenous microorganisms or augmenting the native microbial population to facilitate the mobilization of residual oil. For an in-depth review of MEOR and the mechanisms involved we refer to Youssef et al. (2008). Overall, lab-scale experiments have been mostly successful (e.g. Bordoloi et al. 2007; Bryant et al. 1998; Suther et al. 2009), in terms of oil recovery, while field-scale results have had variable success (e.g. Hiltzman, 1988, 1983; Lazar, 1991). Deleterious microbial activity or antagonistic affects due to the combination of multiple incompatible MEOR mechanisms (as discussed later) are potential reasons for inconsistent field-scale success.

Using MEOR either beneficial or detrimental microbial activity is possible (Bao et al. 2009). Beneficial activities include; biosurfactant production that reduces interfacial tension (e.g. Bryant and Douglas, 1988), generation of biogenic gas that can dissolve into the oil phase and reduce its viscosity (e.g. Bryant and Burchfield, 1989), or hydrocarbon degradation that

can reduce oil viscosity by microbial conversion of long chain alkanes to shorter chain alkanes (e.g. Wankui et al. 2006). Detrimental activities include; generation of hydrogen sulfide that is highly corrosive to oil-extraction equipment (e.g. McInerney et al. 1991) or bioclogging that can potentially inhibit oil blob mobilization (e.g. Soudmand-asli et al. 2007). While many researchers report the synergistic affect of linking multiple MEOR mechanisms, it is also likely that antagonistic affects could occur.

In this report, we investigate the MEOR mechanism of interfacial tension reduction with and without the MEOR mechanism of bioclogging to understand the synergistic/antagonistic relationship between these two MEOR mechanisms and ultimately how this relationship affects oil recovery. Previous studies (see Chapter 5) indicate that in 3-dimensional columns packed with glass beads both treatment options give similar results. Yet, in 2-dimensional micromodel experiments Chapter 4 showed that bioclogging with IFT reduction significantly enhanced oil recovery in comparison to oil recovery with just IFT reduction. Conversely, Soudmand-asli et al. (2007) demonstrate that bioclogging inhibits oil recovery in fractured 2-dimensional micromodel networks. Additionally, numerous reports have shown that microbial transport through porous media, and thus the subsequent distribution of microorganisms and microbial activity is direct dependent on the ratio between pore throat sizes and microorganism size (e.g. Lappin-Scott et al. 1988; MacLeod et al. 1988; Mckinley et al. 1988). Thus, it is likely that oil recovery with MEOR is (highly) dependent on pore morphology. It is our proposition that IFT reduction with bioclogging could either be detrimental or beneficial to oil recovery depending on pore morphology.

We take this approach since numerous multiphase flow studies have shown that understanding pore morphology is critical for oil recovery; oil blob morphology and oil saturation, which ultimately affects oil blob mobilization are directly dependent on pore morphology (Schnaar and Brusseau 2005; Schnaar and Brusseau 2006; Costanza-Robinson et al. 2008; Brusseau et al. 2009). Results, in the previously cited manuscripts, demonstrate that residual oil blob size, interfacial area, and residual oil area-to-volume ratios (and the skew of these distributions) are directly related to mean grain size, grain surface area, grain size homogeneity, and angularity. From these relations, Costanza-Robinson et al. (2008) was successful at developing an empirical relationship for air/water interfacial area as a function of water saturation and geometric grain surface area. Furthermore, the inclusion of pore-scale parameters and realistic porous networks/domains into numerical models have led to

accurate prediction of various multiphase flow properties (e.g. Karpyn and Piri 2007a, 2007b; Porter et al. 2010; Joekar-Niasar et al. 2010).

Another aspect of implementing MEOR deals with controlling/understanding reservoir microbiology. Currently, reservoir treatment regimes are being designed to augment reservoir specific microorganisms, and thus, which MEOR mechanism is utilized for recovery. For example, the addition of nitrate, nitrite, or nitrate/molybdate mixtures are used to inhibit the activity of sulfate reducing bacteria (Youssef et al. 2008; Bao et al. 2009; Jackson et al. 2010). Bao et al. (2009) conducted selective activation experiments on formation water from a Shengli oilfield (China) and were successful at stimulating the growth of hydrocarbon degrading bacteria and methane producing bacteria while restricting the growth of sulfate reducing bacteria. Field-scale reservoir characterization is often accomplished using DNA microarrays (Jackson et al. 2010), which target highly conserved species specific regions of an organisms' 16s rRNA. Zhang et al. (2010) used 16s rRNA characterization to study microbial community response during the injection of bacteria and nutrients into a Daqing oilfield (China). In laboratory experiments by Zhang et al. (2010), the targeted bacteria were easily activated, however, at the field-scale the targeted bacteria did not survive and the activated microbial communities were not the communities predicted from the lab-scale experiments. Field trials such as those previously mentioned, demonstrate that shifts in species specific population densities are likely to occur during MEOR. While further advances are needed to better control/characterize subsurface microbial communities, knowing which MEOR mechanism is the most suitable for a given reservoir, in terms of pore morphology, will help in deciding which microbial population must be stimulated to improve oil recovery.

6.3 Materials and Methods

To facilitate this research, we utilized a software package called 3DMA-ROCK, which analyzes segmented CMT images of porous media and divides the pore-space into individual pore bodies separated by pore throats (Lindquist 2002). 3DMA-ROCK has been utilized by numerous researchers to characterize porous media (e.g. Joekar-Niasar 2010, Prodanović et al. 2007), understand changes in pore morphology during biomineralization (e.g. see Appendix A), and dissolution processes (e.g. Cai et al. 2009). Pore morphology quantification is accomplished by constructing a medial axis through the void space (i.e. pore-space), followed by searching the medial axis for regions of minimal surface cross-sectional area, which are then defined as throats. 3DMA-ROCK divides the pore-space into individual pore

bodies separated by throats, which represent only a surface and have no volume. Parameters such as, pore radii, throat radii, coordination number, and pore aspect ratio, are obtainable with 3DMA-ROCK.

6.3.1 Pore Morphologies

To obtain unique and representative pore morphologies different diameter glass spheres and/or crushed glass were packed into glass columns and sintered in a muffle furnace at 760^{o}C for 20 minutes. In total four pore morphologies were generated: (1) Homogeneous spherical mixture (35%, 600 µm diameter glass spheres, 35%, 850 µm diameter glass spheres, 30%, 1.0 to 1.4 mm diameter glass spheres), (2) Heterogeneous spherical mixture (50%, 400 µm diameter glass spheres, 50%, 1.0 to 1.4 mm diameter glass spheres), (3) Fine angular mixture (100%, crushed glass < 800 µm, nominal sieve opening), and (4) Fine/coarse angular mixture (50%, crushed glass < 800 µm, nominal sieve opening, 50%, crushed glass > 800 µm, nominal sieve opening)

For the homogeneous spherical mixture the different diameter glass spheres were uniformly distributed throughout the column, while for the heterogeneous spherical mixture that was not the case. A uniform mixture is subjective and was accomplished by carefully packing the column with only a few beads at a time.

6.3.2 MEOR

Columns were sterilized with three pore volumes of ethanol and then rinsed with three pore volumes of Medium E (Table 4.1). Columns were then saturated with Soltrol 220 followed by water flooding with Medium E. Water flooding was performed under fixed flux conditions at 0.18 ml/hour with a standard syringe pump. Once three pore volumes of Media E was pumped through a column it was assumed that residual oil saturation was established, and at this point, the column was imaged with x-ray computed microtomography.

Two MEOR flooding solutions were investigated: (1) bacteria and biosurfactant, and (2) biosurfactant only. Duplicates were performed for each possible combination of pore

morphology and flooding solution. The bacterium was *Bacillus mojavensis* JF-2 (ATCC 39307), which was grown with Medium E (Chapter 4, Table 4.1) at room temperature and under well-mixed conditions in a bioreactor. The contents of the bioreactor are referred to as flooding solution 1. Interfacial tension (IFT) between the bioreactor contents and Soltrol 220 was measured with a Du Noüy ring tensiometer. Flooding solution 2 was prepared by growing a batch culture of JF-2 and then removing the bacterial cells. Bacterial cultures of JF-2 were centrifuged at 9,000 rpm for 30 minutes; the supernatant was used as flooding solution 2. A few drops of chlorine were added to flooding solution 2 to insure that bacterial contamination would not occur. The IFT of the resulting biosurfactant solution was measured to verify that the same IFT as prior to biomass removal was obtained. Thus, both flooding solutions had similar IFT.

MEOR treatment was commenced after water flooding by infusing 3-12 pore volumes of either flooding solution. A standard curve relating bacterial cell mass (as dry weight) to the optical absorbance of flooding solution 1 at 600 nm was generated. Optical absorbance measurements were then used to calculate the biomass concentration in the bioreactor, and thus, the amount of biomass infused during MEOR with flooding solution 1. After continuous pumping, at 0.18 ml/hour, for a given number of pore volumes (for flooding solution 2) or given amount of biomass infused (for flooding solution 1), the columns were imaged with x-ray computed microtomography.

6.3.4 X-Ray Microtomography

Dry columns were imaged using synchrotron-based x-ray microtomography at the GeoSoilEnviroCARS (GSECARS) 13-BM-D Beamline at the Advanced Photon Source (APS), Argonne National Laboratory. The GSECARS bending magnet beam-line provides a fan-beam of high-brilliance radiation, collimated to a parallel beam with a vertical size of approximately 5 mm. Two images were collected and stacked vertically. Thus, a 10 mm window in the vertical center of each column was imaged. During imaging, 720 projections were collected over 180° and the images were collected at 11.3 µm/pixel resolution, after 2x binning of the data. Scan time was 5 to 10 minutes. Dry column images were analyzed with 3DMA-Rock for pore morphology characterization.

MEOR induced residual oil saturation was measured using the Oregon State University, School of Mechanical, Industrial and Manufacturing Engineering, micro-CT Laboratory. The cone beam tomography system is powered by a Focus FXE-160.20 x-ray tube, which was operated at 100 keV and 78 μamp•s. For each angle collected, four projections were averaged. Over 360^{o} of rotation 1440 averaged projections were collected with a 2448 x 2048 pixel CCD camera (16-bit). Image resolution was 9.2 μm/pixel, scan time was approximately 80 minutes, and a 20 mm vertical region of each column was imaged. To enhance contrast between the wetting and non-wetting phase, cesium chloride was added to the water phase (1:6, $CsCl:H_2O$, mass ratio). The resulting images were analyzed for residual oil saturation.

6.3.5 Segmentation

Image segmentation was accomplished using indicator kriging-based thresholding (Oh and Lindquist, 1999). This approach is based on two user defined threshold values that establish reasonable upper and lower boundaries. Any voxel value below the lower limit is labeled as one phase and any voxel value above the upper limit is labeled as another phase. Voxels with values between the lower and upper limit are segmented with indicator kriging, which considers the spatial covariance of the image (Oh and Lindquist 1999).

6.3.6 Pore Morphology

A representative elementary volume (REV) analysis, in terms of porosity, was conducted on the 4 dry column images from the APS. On average, for all pore morphologies analyzed, porosity was found to be invariable at a volume greater than ~80 mm^3. The REV volumes were then imported into 3DMA-ROCK for medial axis and pore body/throat construction. When referring to the 3DMA-ROCK data, effective pore radii is the radius of a sphere of equivalent volume and effective throat radii is the radius of a circle of equivalent area. For more detailed information on the algorithms used with 3DMA-ROCK, we refer to the publications by Prodanović et al. (2006) and Lindquist (2002) and references therein.

Additionally, the REV volumes were analyzed for sphericity (*S*), which is a metric that measures how spherical an object is, calculated as

$$S = \frac{\Pi^{\frac{1}{3}}(6V_p)^{\frac{2}{3}}}{A_p} \tag{6.1}$$

where, V_p is the particle volume (length cubed), A_p is the particle surface area (length squared).

6.4 Results and Discussion

3DMA-Rock results are presented in Figure 6.1. The spherical mixtures have considerably larger pore and throat radii and broader distributions thereof, than columns constructed from the angular mixtures. The homogenous spherical mixture has the broadest effective throat and pore radii distributions, while the fine angular mixture has the narrowest effective throat and pore radii distributions. Average coordination numbers are 3.4, 3.6, 3.8, and 4.0, and average sphericities are 0.08, 0.11, 0.25, and 0.24, for the fine angular, fine/coarse angular, homogenous spherical, and heterogeneous spherical mixtures, respectively. Spherical mixtures resulted in <1 sphericity, since during the sintering process many of the smaller glass beads completely fused together instead of just fusing at the contact points.

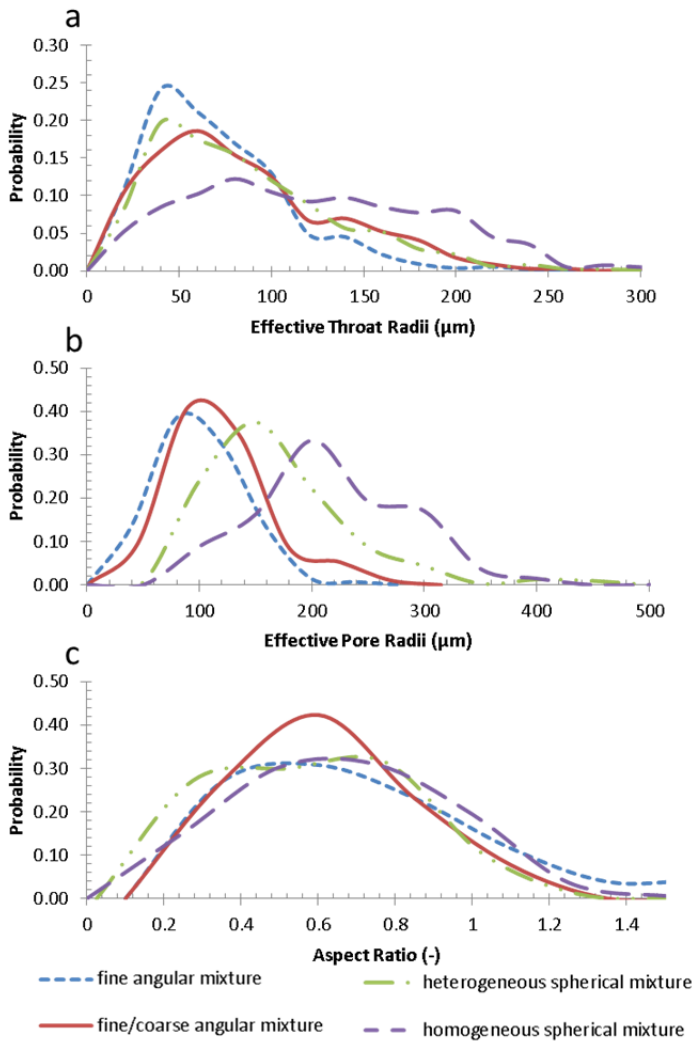

Figure 6.1: Pore morphology results from 3DMA-ROCK; effective throat radii distributions (a), effective pore radii distributions (b), and aspect ratio distributions (c).

The residual oil (S_{or}) values reported on the ordinate (at zero biomass/pore volume infused) of Figure 6.2a and 6.2b were measured after water flooding and can be used to quantify the amount of capillary trapping that occurred during water flooding (Mahmud et al. 2006; Nguyen et al. 2006; Chang et al. 2009; Knackstedt et al. 2010; see 2.2.2 Dynamic Imbibition). Pore morphologies that result in larger S_{or} are those where capillary trapping is more prevalent. Accordingly, the largest amount of capillary trapping occurred in the fine/coarse angular and heterogeneous spherical mixtures which have average effective throat radii of 77 and 78 µm, respectively, and rather broad throat radii distributions. In comparison, the

fine angular mixture had the smallest average effective throat radius (i.e. 63 µm), which would suggest more prevalent snap-off, and thus, greater S_{or} than the two previously mentioned pore morphologies. However, the narrower distribution of effective throat and pore radii for the fine angular mixture seemed to result in less snap-off. As noted by Melrose and Brander (1974), residual non-wetting phase saturation increases as the pore-size distribution broadens. In accordance with this, the presented results demonstrate that average throat radii is not the determining factor that dictated snap-off, the distribution of radii and most likely the spatial arrangement of throats also affected the amount of snap-off.

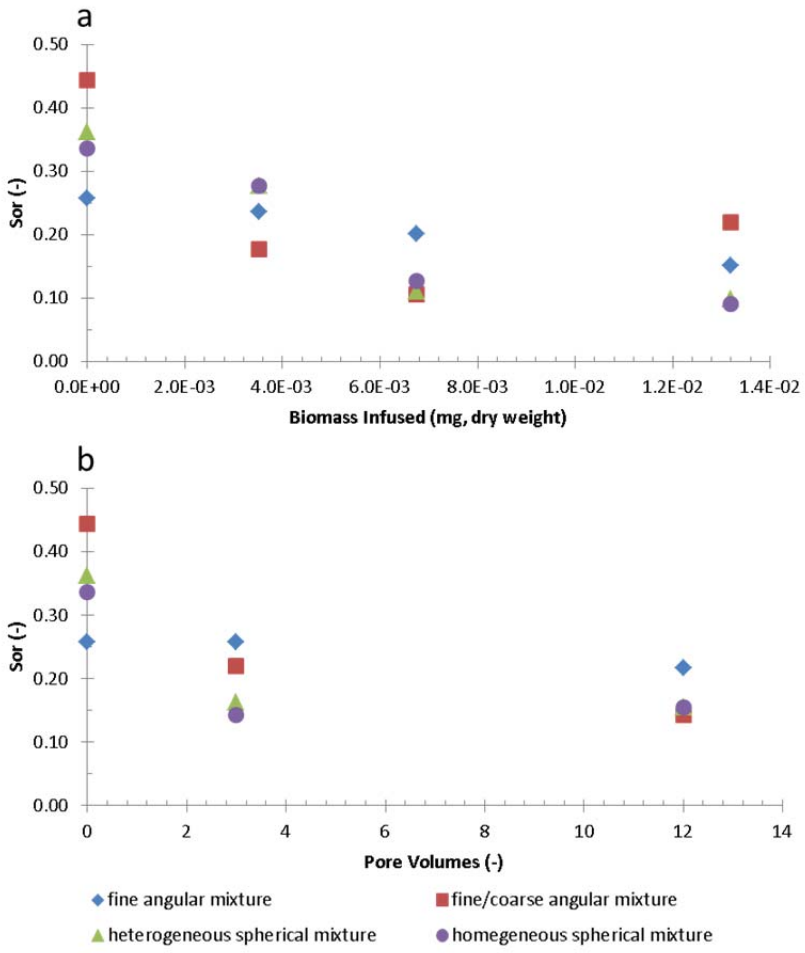

Figure 6.2: Residual oil saturation in terms of biomass infused (a) or pore volumes infused (b) for JF-2 and biosurfactant treatment, respectively. Saturation values at zero biomass/pore volume infused correspond to average S_{or} measured after water flooding.

During MEOR using JF-2 (Figure 6.2a), the amount of oil recovered was directly dependent on the amount of biomass infused. Residual oil saturations leveled-out around 6.0E-3 mg (as dry weight) of biomass infused, which corresponded to approximately 6 pore volumes of infused JF-2 solution. For biosurfactant treatment (Figure 6.2b), S_{or} values leveled-out once approximately 3 pore volumes were infused. The IFT for both treatment options was ~0.6 dynes/cm. The results suggest that when using JF-2 treatment, the majority of recovery is caused by IFT reduction via the biosurfactant, while additional recovery obtained with additional pore volumes infused is likely caused by bioclogging. Overall, both treatment options gave positive results, in terms of reduced residual oil saturation.

Visual renderings of residual oil blobs obtained in the pore morphologies tested are displayed in Figure 6.3. The red residual oil is oil recovered during MEOR, while the yellow oil blobs correspond to oil that remained trapped during MEOR. The images display significantly different residual oil blob morphologies for the pore morphologies tested. The more homogeneous mixtures (i.e. the homogenous spherical mixture and the fine angular mixture) have smaller more uniform residual oil blobs after water flooding (Figure 6.3a1 and 6.3c1), while the more heterogeneous mixtures (i.e. the heterogeneous spherical mixture and the fine/coarse angular mixture) have larger ganglia that span multiple pores after water flooding (Figure 6.3b1 and 6.3c1). Using either JF-2 or biosurfactant treatment (i.e. flooding solution 1 or 2) the largest oil bobs were recovered and at least a portion of almost every oil blob that remained after water flooding was recovered during MEOR. For example, in Figure 6.3, almost every yellow oil blob is either partially or completely connected to a red oil blob, meaning that at least a fraction of every oil blob that remained trapped after MEOR was recovered during MEOR. Lenormand et al. (1983) reported that, depending on the pressure gradient and pore neck size, two different oil blob mobilization events can occur; either the entire oil blob enters the neck and quickly becomes mobilized, or a fraction of the blob separates from the parent blob as an individual droplet that then becomes mobilized. Both scenarios are apparent in Figure 6.3; however, the latter of the two scenarios is more prevalent in the angular mixtures (Figure 6.3c1 and 6.3d1).

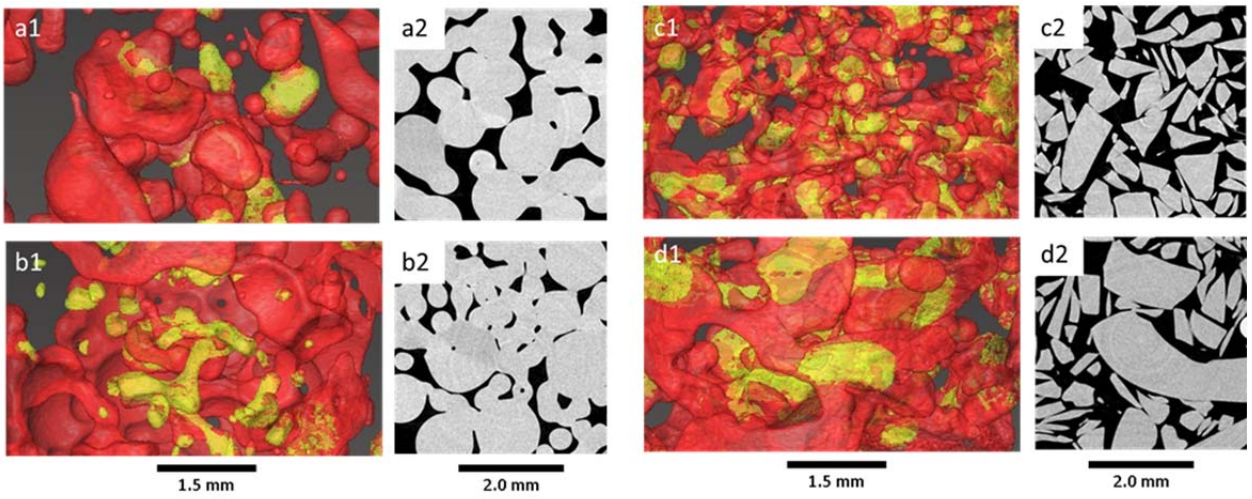

Figure 6.3: Example CMT image for the homogeneous spherical mixture (a), heterogeneous spherical mixture (b), fine angular mixture (c), and fine/coarse angular mixture (d). In the three-dimensional renderings of the residual oil blobs, red blobs were mobilized during MEOR while yellow blobs remained trapped (a1, b1, c1, and d1). In the gray-scale CMT slices showing examples of the different pore morphologies tested. The dark region corresponds to the void space (a2, b2, c2, and d2).

Additional oil recovered was correlated to average pore morphological parameters extracted from the CMT images with 3DMA-ROCK (Figure 6.4). The correlation plots demonstrated that *AOR* increases with increasing average grain sphericity, average effective throat radii, average coordination number, and average effective pore radii, while *AOR* decreased with increasing porosity and average aspect ratio. In some instances biosurfactant treatment is slightly more efficient than JF-2 treatment, however, *AOR* results were similar and no definite reverse trends are observed for either treatment option. For example, for a given pore morphology parameter, biosurfactant treatment does not consistently perform better than JF-2 treatment. However, for the fine angular mixture, which has the largest porosity, largest average aspect ratio, and smallest average sphericity, JF-2 treatment performed significantly better than biosurfactant treatment.

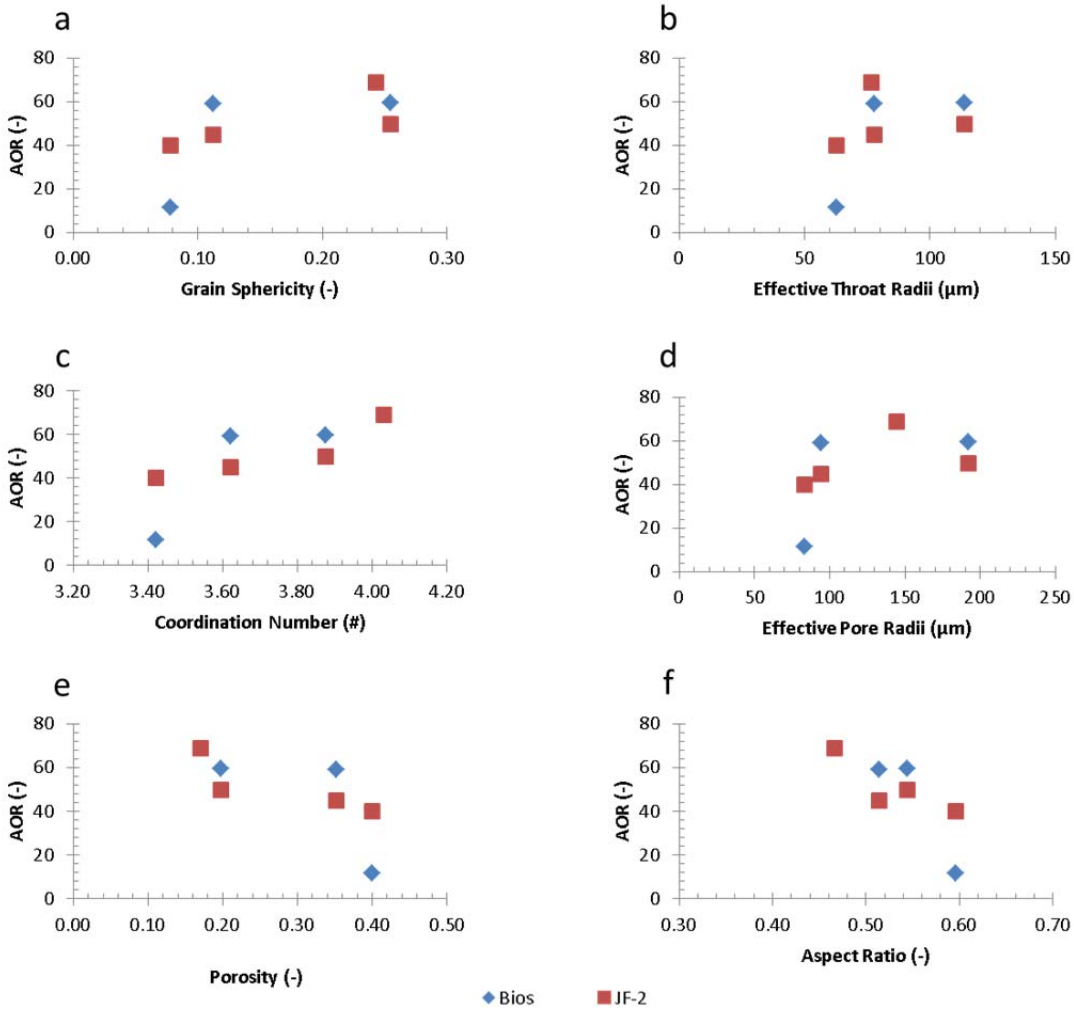

Figure 6.4: Average pore morphology parameters; grain sphericity (a), effective throat radii (b), coordination number (c), effective pore radii (d), porosity (e), and aspect ratio (f), related to additional oil recovered with either JF-2 or biosurfactant treatment.

The correlation plots, shown in Figure 6.4, can be considered in the context of the criterion for oil blob mobilization. For mobilization to occur the pressure gradient over the length of the oil blob must exceed the capillary pressure requirement for the oil blob to pass through a given pore neck (Wardlaw and McKellar, 1985). Thus, as the distribution of pore neck sizes decreases, an increasingly larger pressure gradient or a significant interfacial tension reduction is required for mobilization. Since oil blobs trapped in larger pore throat geometries require smaller pressure gradients for mobilization, *AOR* increases as average

throat size increases (Figure 6.4b). For the pore morphologies tested, less spherical grains and smaller effective pore sizes (radii) resulted in smaller effective pore neck sizes, thus, *AOR* increases as average pore radius and average sphericity increases (Figure 6.4a and 6.4d). The trend realized in Figure 6.4c is explained by the following argument: as a pore becomes more interconnected the likelihood for a given pore to have a pore-neck size that meets the critical requirement for mobilization to occur increases, and thus, *AOR* increases as coordination number increases. The negative trend seen with porosity (Figure 6.4e), may occur because columns were flooded at a constant flux of 0.18 ml/hour, and thus, lower porosity columns would have higher pore velocities, resulting in a greater pressure gradient. Overall, our results demonstrate that residual oil blob morphology (as displayed in Figure 6.3) depends on pore morphology, which ultimately affects MEOR (as shown in Figure 6.4).

6.5 Conclusions

- The amount of capillary trapping and the resulting initial morphology of residual oil blobs are explained by the average effective pore throat and body sizes and the distribution thereof.
- During bioclogging, oil recovery is directly dependent on the amount of biomass infused.
- Bioclogging with IFT reduction outperformed IFT reduction without bioclogging, in terms of *AOR*, in the pore morphology with the largest porosity, largest aspect ratio, and lowest grain sphericity.
- At least a fraction of every oil blob that remained trapped after MEOR was recovered during MEOR.
- Positive correlations between *AOR* and grain sphericity, effective throat size, effective pore size, and coordination number are reported.
- Negative correlations between *AOR* and porosity and aspect ratio are reported.

6.6 Acknowledgement

Acknowledgment is made to the Donors of the American Chemical Society Petroleum Research Fund for support of this research (grant number 48505-AC9). Microtomography was performed at GeoSoilEnviroCARS (Sector 13), Advanced Photon Source (APS), Argonne National Laboratory. GeoSoilEnviroCARS is supported by the National Science Foundation-Earth Sciences (EAR-0217473), Dept. of Energy-Geosciences (DE-FG01-94ER14466) and the State of Illinois. Cone-beam microtomography was performed at Oregon State University, School of Mechanical, Industrial and Manufacturing Engineering, x-ray Tomography Laboratory.

Chapter 7. Discussion and Conclusions

7.1 Summary

This dissertation explores the pore-scale physics occurring during microbial enhanced oil recover. Micromodel experiments imaged with stereo microscopy and column experiments imaged with computed x-ray microtomography were utilized to obtain pore-scale parameters relevant to multiphase flow. The foremost objective was to identify the oil reservoir type, in terms of wettability and pore morphology, for which a given MEOR mechanism would be the most suitable. The specific objectives of this research were to:

1. Develop and validate a method to measure the interfacial curvature of fluid-fluid interfaces from 3-dimensional pore-scale images.

2. Identify how the MEOR mechanisms of biosurfactant-facilitated and biomass-facilitated recovery compare to each other and to abiotic recovery where the flow rate of the flooding phase is increased.

3. Identify how porous systems of different inherent wettability lend themselves to biosurfactant-facilitated and/or biomass-facilitated oil recovery.

4. Identify how different porous media pore throat size distributions, pore body size distributions, and thus pore-scale spatial distribution of residual oil and oil blob morphology affect oil mobilization when using biosurfactant-facilitated and/or biomass-facilitated MEOR.

Chapter 3 presented/validated a method to measure interfacial curvature from pore-scale CMT data. The results indicated good agreement between curvature-based and transducer-based capillary pressure measurements. The presented method allows for measuring disconnected phase capillary pressure, which is unobtainable with the standard transducer-

based method. Overall, this approach allows for a detailed assessment of interfacial curvature during drainage and/or imbibition and provides researchers a new perspective from which to study these processes. This curvature estimation method was used in Chapter 5 to study oil blob mobilization during MEOR. Additionally, as highlighted in Chapter 3, the relaxation of interfaces during the transition from dynamic to static conditions was demonstrated by measuring interfacial curvature, and thus, could potentially be used to develop new dynamic capillary theoretical relationships for now P_c-S_w-A_{nw}.

Chapter 4 explored the effectiveness, in terms of oil recovered, of each proposed MEOR mechanism. Micromodel experiments allowed for direct visualization of the biological phase, such that the extent of bioclogging could be quantified. The results revealed that oil recovery was strongly dependent on the amount of biomass infused during MEOR treatment. Bioclogging (with minimal IFT reduction) was the most effective MEOR mechanism, in terms of *AOR*. However, the presented micromodel results contradict some results in the existing literature, which report that bioclogging is potentially detrimental to oil blob mobilization. Consequently, it was proposed that the effectiveness of a given MEOR mechanism is dependent on inherent pore-scale reservoir characteristics; this proposition was then addressed in Chapters 5 and 6.

Chapter 5 investigated MEOR in fractional-wet systems. A conceptual model was developed that suggests that at low capillary number, preferential flow paths develop through the water-wet regions of the pore space, resulting in a large amount of disconnected oil. The MEOR mechanisms of interfacial tension reduction and bioclogging with interfacial tension reduction were compared and no major differences between the two approaches in terms of interfacial curvature, residual oil blob size, and oil recovery, were measured. After MEOR, the remaining oil was located in purely oil wet-pores, implying that the oil recovered during MEOR was the fraction of oil in fractional-wet pores.

Chapter 6 considered the effectiveness of interfacial tension reduction with and without bioclogging in a range of different pore morphologies. The extent of capillary trapping that occurred during water flooding was strongly dependent on pore neck and body sizes and the distributions thereof, where a more skewed distribution resulted in more capillary trapping. During MEOR, oil recovery increased with increasingly larger pore throat size and sphericity

and increasingly lower porosity and aspect ratio. In the majority of pore morphologies tested, both MEOR mechanisms gave similar *AOR* results. However, in the pore morphology with the largest porosity, the largest aspect ratio, and the lowest sphericity, bioclogging with IFT reduction significantly improved recovery, in comparison to just IFT reduction.

Collectively, these results demonstrate the effect of surface wettability and pore morphology on capillary trapping and the subsequent mobilization of capillary trapped oil. In angular pore morphologies with large pore aspect ratios and low porosity or very low connectivity, such as the case with micromodels, bioclogging significantly improved oil recovery, in comparison to IFT reduction without bioclogging. In the fractional-wet systems tested, water flooding was relatively inefficient at recovering oil, and thus, a large amount of residual oil remained trapped in the oil-wet pores after water flooding. However, the recovery of this oil from the oil-wet pore space was achievable with interfacial tension reduction. With each pore morphology and fractional-wet system tested the MEOR mechanisms of bioclogging and/or IFT reduction were successful at recovering at least a fraction of the capillary trapped oil. For either mechanism, oil blob mobilization preceded in a similar manner as to what occurs during abiotic recovery (i.e. with increasing flow rate). During MEOR, relatively low capillary pressure residual oil blobs are the easiest fraction of oil to recovery, while higher capillary pressure residual oil blobs remain trapped in the pore-space. In terms of oil blob morphology, during MEOR, the largest residual oil blobs are either mobilized and recovered from the pore space or broken-up into smaller residual oil blobs that, in some circumstances, remain trapped in the pore space.

7.2 Notable Findings

The results presented in this dissertation are from an innovative approach where bacterial oil recovery processes at the pore-scale are studied using computed microtomography. While numerous lab-scale MEOR experiments have been conducted and the results are published throughout the literature, MEOR pore-scale processes (in a 3-dimensional porous medium) have not been studied. Thus, the data presented in this dissertation are the first MEOR experiments were pore-scale information was collected. Specifically, the most notable findings include the following:

- In a multiphase system the pressures in the connected and disconnected phases are significantly different. Specifically, the disconnected nonwetting phase remains at

the P_c at which snap-off occurs, and thus, the P_c of disconnected nonwetting phase can be used as a history of the pressures experienced by the system. This is the first experimental work where P_c is measured from CMT data, and thus, the results provide a valuable insight into the behavior of multiphase flow, which was previously unobtainable.

- Metabolically active microorganisms are not required for MEOR-based recovery. In micromodel experiments dead biomass with minimal IFT reduction recovered similar amounts of oil as metabolically active bacteria with maximum IFT reduction. This suggests that no complicated *in situ* field-scale implementation is required. Simply, the injection of *ex situ* produced microbial metabolic byproducts can facilitate the mobilization of residual oil.

- During water flooding, in fractional-wet systems, both imbibition and localized drainage processes occur. For localized drainage to occur, an entry pressure must be achieved by either increasing the viscous force or decreasing the interfacial force. When capillary number is low, fluid/fluid interfaces reside mostly in fractional-wet pores and the oil-wet pores drain at relatively high capillary number.

- Capillary trapping is most prevalent in porous media systems that have a wide distribution of pore throat and body sizes.

- During MEOR, the largest residual oil blobs become mobilized and in highly angular porous media the mobilization of smaller droplets from the large residual oil blobs is more prevalent than the mobilization of an entire large oil blob.

- The MEOR mechanism of bioclogging is most successful in angular pore morphologies with large aspect ratios and very low connectivity and porosity, and oil recovery is directly dependent on the amount of biomass injected.

- In reservoirs that are largely fractional-wet, the original oil in place tends to remain in place after water flooding. However, in fractional-wet systems oil recovery is achievable with either IFT reduction or IFT reduction with bioclogging.

- In terms of pore morphology, IFT reduction is more successful for high porosity media with relatively large pore throats and spherical grains, while IFT reduction with bioclogging is more suitable for reservoirs with low porosity, low pore connectivity, and angular grains.

7.3 Future Directions

It is evident from the literature and the research presented in this dissertation that a comprehensive understanding of the pore-scale physics occurring during MEOR is far from complete. This dissertation demonstrated the utility of CMT-based multiphase flow experiments and presented/validated a novel method to measure interfacial curvature from such data, which further expands the versatility of CMT-based experiments. Potential future tangents that could be taken from the presented research, providing further insights into MEOR, and thus, multiphase flow, are the following:

- In the experiments presented in Chapter 3, small interfaces, such as, pendular rings were omitted from the curvature estimate due to resolution limitations. Thus, it is unclear if disconnected wetting phase affects capillary pressure. Additionally, the curvature data presented in Chapter 3, suggests that equilibration was not fully achieved neither during drainage nor imbibition. Thus, additional drainage and imbibition experiments imaged at higher resolution and with longer equilibration times are desired.

- Theoretically, both Minkowski functionals and level set methods could be utilized to measure mean curvature from CMT data, and thus, these approaches should be compared to the isosurface approach presented in Chapter 3. These curvature methods should be used to evaluate a few simple ideal systems where error can be quantified, such that, the most accurate and most robust method for measuring interfacial curvature can be identified.

- In chapter 4, the MEOR mechanisms of bioclogging and IFT reduction were not completely decoupled. A genetically engineered model organism where the biosurfactant gene is suppressed, would allow for a direct comparison between bioclogging with and without biosurfactant production. This could be accomplished with a “shotgun” approach using Tn5 mutagenesis.

- By repeating the micromodel experiments using a well-defined growth media, nutrient uptake rates could be measured and used as a metric for microbial activity. This would allow for a well-defined system, where growth rate and biosurfactant yield could be correlated to oil recovery.

- Chapter 4 demonstrated that bioclogging resulted in lower S_{or} than that predicted by capillary number. To further address this result, 2D single phase flow Lattice-Boltzmann simulations, using the bioclogged micromodel images as an initial condition, could be developed. Since average pore velocity is used to calculate capillary number, localized high velocity channels, which may develop during bioclogging, are not well represented by capillary number. Localized high velocity channels could be identified with a Lattice-Boltzmann model, and used to explain why a lower S_{or} is obtained with bioclogging than that predicted by capillary number.

- Direct visualization of bioclogging in real porous media, where realistic pore connectivity is encountered was not achieved. Further development of the CMT-based biofilm imaging method presented in Appendix B would provide the information required to assess the affect bioclogging has on multiphase flow.

- The oil blob mobilization experiments, presented in Chapters 5 and 6, demonstrated that during mobilization large ganglia are broken-up into smaller isolated oil blobs. However, the mobilization of <u>just</u> these isolated oil blobs should be evaluated. In a relatively long column, isolated oil blobs may become trapped further downstream after mobilization. Thus, total recovery from the column could be dependent on the criterion for the mobilization of individual isolated blobs and not on the oil blob morphology after water flooding.

- In Chapter 6, only synthetic porous media was used. Therefore, it should be evaluated if the same trends hold true in more realistic pore morphologies, such as, sandstone. The addition of surface roughness and angularity that is unique to sandstone may have a significant affect on oil recovery.

- Recently the Euler number has been shown to provide significant topological information about porous media systems. The Euler number quantifies the number of connected components, the number of redundant loops, and the number of void spaces in an object. In relation to the work presented in Chapter 6, the number of connected components may provide a measure of whether or not an oil phase becomes disconnected during snap-off. Additionally, it is likely that the Euler number of a disconnected oil blob could predict if the entire blob becomes mobilized or if small droplets from the blob are mobilized.

Bibliography

Afrapoli, M., Alipour, S., and Torsaeter, O. (2010), Effect of wettability on interfacial tension on microbial improved oil recovery with *Rhodococuss sp* 094, SPE 129707, presented at the *SPE Improved Oil Recovery Symposium* held in Tulsa, Oklahoma, 24-28 April.

Al-Raoush, R. I. (2009), Impact of wettability on pore-scale characteristics of residual nonaqueous phase liquids, *Environmental Science and Technology*, 43(13), 4796-4801.

Al-Raoush, R. I., and C. S. Willson (2005a), A pore-scale investigation of a multiphase porous media system, *Journal of Contaminant Hydrology*, 77(1-2), 67-89.

Al-Raoush, R. I., and C. S. Willson (2005b), Extraction of physically realistic pore network properties from three-dimensional synchrotron x-ray microtomography images of unconsolidated porous media systems, *Journal of Hydrology*, 300(1-4), 44-64.

Amott, E. (1959), Observations relating to the wettability of porous rock, *The American Institute of Mining, Metallurgical, and Petroleum Engineers Transactions,* 216, 127-20.

Anderson, W. G. (1986), Wettability literature survey – part 1: rock/oil/brine interactions and the effects of core handling on wettability, *Journal of Petroleum Engineers*, vol. 36, No. 11.

Bao, M., Kong, X., Jiang, G., Wang, X. and Li, X. (2009), Laboratory study of activating indigenous microorganisms to enhance oil recovery in Shengli oilfield, *Journal of Petroleum Science and Engineering*, 66, 42-46.

Baviere M. (1991), Basic concepts in enhanced oil recovery processes, Elsevier Applied Science, *Critical reports in Applied Chemistry,* Volume 33.

Bear, J. (1988), Dynamics of fluids in porous media, *Dover Publications*, Inc.

Bobek, J. E., Foster, J. F., and Risser, J. K. (1956), Determination of wettability-G-UW-45, *International Report No. L-52*, April, 10, Saudi Aramco.

Bordoloi, N. K., and B. K. Konwar (2008), Microbial surfactant-enhanced mineral oil recovery under laboratory conditions, *Colloids and Surfaces B-Biointerfaces*, 63(1), 73-82.

Borysenko, A., B. Clennell, R. Sedev, I. Burgar, J. Ralston, M. Raven, D. Dewhurst, and K. Y. Liu (2009), Experimental investigations of the wettability of clays and shales, *Journal of Geophysical Research-Solid Earth*, 114, 7202, 0148-0227.

Bredholt, H., K. Josefsen, A. Vatland, P. Bruheim, and K. Eimhjellen (1998), Emulsification of crude oil by an alkane-oxidizing *Rhodococcus* species isolated from seawater, *Canadian Journal of Microbiology*, 44(4), 330-340.

Brusseau M. L., Narter, M., Schnaar, G., and Marble, J. (2009), Measurement and estimation of organic-liquid/water interfacial areas for several natural porous media, *Environmental Science and Technology, 43*, 3619-3625.

Bryant, R. S., Burchfield, T. E.; Dennis, D. M.; and D. O. Hitzman. (1990), Microbial enhanced waterflooding: mink unit project, *Society of Petroleum Engineers Reservoir Engineering*, 5, 9-13.

Bryant, R. S. and Douglas, Jonell (1988) Evaluation of microbial systems in porous media for EOR, *Society of Petroleum Engineers Reservoir Engineering*, May, 489-495.

Bryant, R. S. and Burchfield, T. E. (1989), Review of microbial technology for improving oil recovery, *Society of Petroleum Engineers Reservoir Engineering*, 4, 151-154.

Bryant, R. S. and Lockhart, T. P. (2002), Reservoir engineering analysis for microbial enhanced oil recovery, *Society of Petroleum Engineers Reservoir Evaluation and Engineering*, 5, 365-374.

Butt, H.J., Graf, K., and Kappl M. (2006), Physics and chemistry of interfaces 2nd edition, *Wiley-VCH Verlag GmbH and Co. KGaA*, Weinheim, ISBN-13: 978-3-527-40629-6.

Chase, K.L., Bryant, R. S., Burchfield, T. E., Bertus, K. M., and Stepp, A. K. (1990) Investigations of microbial mechanisms for oil mobilization in porous media, Microbial Enhancement of Oil Recovery – Recent Advances, ed. E.C. Donalsdon, *Amsterdam: Elservier Science Publishers*.

Chen, D. Q., L. J. Pyrak-Nolte, J. Griffin, and N. J. Giordano (2007), Measurement of interfacial area per volume for drainage and imbibition, *Water Resources Research*, *43*(12), 6.

Cheng, J. T., L. J. Pyrak-Nolte, D. D. Nolte, and N. J. Giordano (2004), Linking pressure and saturation through interfacial areas in porous media, *Geophysical Research Letters*, *31*(8), 4.

Costanza-Robinson M. S., Harrold, K. H. and Lieb-Lappen, R. M. (2008), X-ray microtomography determination of air-water interfacial area-water saturation relationships in sandy porous media, *Environmental Science and Technol*ogy, 42, 2949-2956.

Costerton, J., Lewandowski, D., Caldwell, D., Korber, D., and Lappin-Scott, H. (1995), Microbial biofilms, *Annual Review Microbiology*, 49, 711-745.

Crescente, C., Torsaeter, O., Hultmann, L., Stroem, A., Rasmussen, K., and Kowalewski, E. (2006), An experimental study of driving mechanisms in MIOR processes by using *Rhodococcus* sp. 094. SPE paper 100033, presented at the *International Symposium on Improved Oil Recovery*, Tulsa, Oklahoma, 22-26 April.

Crescente, C., Rekdal, A., Abriz, A., and Torsaeter, O. (2008), A pore level study of MIOR displacement mechanisms in glass micromodels using *Rhodococcus*, sp. 094, SPE 110134, presented at the *Society of Petroleum Engineers symposium on Improved Oil Recovery*, Tulsa, Oklahoma, 20-23 April.

Culligan, K. A., D. Wildenschild, B. S. B. Christensen, W. G. Gray, M. L. Rivers, and A. F. B. Tompson (2004), Interfacial area measurements for unsaturated flow through a porous medium, *Water Resource Research*, 40, W12413.

Cunningham, A. D., Characklis, W. G., Abedeen, F., and Crawford, D. (1991), Influence of biofilm accumulation in porous media hydrodynamics, *Environmental Science and Technology*, vol 25 (7), 1305-1311.

De la Cruz, V. and Spanos, T. J. T. (1983), Mobilization of oil ganglia, *American Institute of Chemical Engineers Journal,* 29, 854.

Donaldson, E. C., Thomas, R. D., and Lorenz, P. B. (1969), Wettability determination and its effect on recovery efficiency. *Society of Petroleum Engineers Journal*, 13-20, March.

Dullien F. A. L. (1992), Porous media: fluid transport and pore structure 2nd edition, *Academic Press*, San Diego, Ca, ISBN: 0-12-223651-3.

Dunsmore, B.C., Bass, C.J., and Lappin-Scott, H.M. (2004), A novel approach to investigate biofilm accumulation and bacterial transport in porous matrices, *Environmental Microbiology* 6, No. 2, 183.

Energy Information Administration (2011), Annual Energy Outlook DOE/EIA-0383 (2011). Report to the U.S. Department of Energy Washington, DC.

Fatt, I., Aime, M., and Klikoff, W. (1959), Effect of fractional wettability on multiphase flow through porous media, Technical Note, *The American Institute of Mining, Metallurgical and Petroleum Engineers Transactions*, October.

Fisher, J. B. (1987), Distribution and occurrence of aliphatic acid anions in deep subsurface waters, *Geochimica et Cosmochimica Acta*, 51, 2459–2468.

Gandler G. L. (2006), Mechanistic understanding of microbial plugging for improved sweep efficiency, *Master of Science Thesis*, The University of Texas at Austin, May 2006.

Graue, A., Bognø, T., Moe, R.W., Baldwin, B.A., Spinler, E.A., Maloney, D., Tobola, D.P. (1999), Impacts of wettability on capillary pressure and relative permeability, SCA9907, *International Symposium of the Society of Core Analysts*, Golden, Co, USA, Aug 1-4, 1-14.

Gray, W. G., and Hassanizadeh, S. M. (1991a), Paradoxes and realities in unsaturated flow theory, *Water Resources Research*, 27(8), 1847-1854.

Gray, W. G., and Hassanizadeh, S. M. (1991b), Unsaturated flow theory including interfacial phenomena, *Water Resources Research*, 27(8), 1855-1863.

Gray, W. G., and Miller, C. T. (2011), TCAT analysis of capillary pressure in non-equilibrium, two-fluid-phase, porous medium systems, *Advances in Water Resources*, 34, 770-778.

Gray, R. M., Yeung, A., Foght, M. J., and Yarranton, W. H. (2008), Potential microbial enhanced Oil Recovery Processes: a critical analysis, *Society of Petroleum Engineers Annual Technical Conference and Exhibition*, SPE 114676, Denver, Colorado, 21-24 September.

Han, J., Jin, Y., and Willson, C. S. (2006), Virus retention and transport in chemically heterogeneous porous media under saturated and unsaturated flow conditions, *Environmental Science and Technology*, 40, 1547-1555.

Hassanizadeh, S. M., and Gray, W. G. (1990), Mechanics and thermodynamics of multiphase flow in porous media including interphase boundaries, *Advances in Water Resources*, 13(4), 169-186.

Hassanizadeh, S. M., and Gray, W. G. (1993), Thermodynamic basis of capillary-pressure in porous-media, *Water Resources Research*, 29(10), 3389-3405.

Hassanizadeh, S. M., Celia, M. A., and Dahle, H. K. (2002), Dynamic effect in the capillary pressure-saturation relationship and its impacts on unsaturated flow, *Vadose Zone Journal*, 1(1), 38-57.

Head, I. M., Jones, D. M., and Larter, S. R. (2003), Biological activity in the deep subsurface and the origin of heavy oil, *Nature,* 426:344-352.

Held, R.J., M. A. Celia (2001), Modeling support of functional relationships between capillary pressure, saturation, interfacial area and common lines, *Advances in Water Resources*, 24:325–43.

Helland, J. O., and S. M. Skjaeveland (2007), Relationship between capillary pressure, saturation, and interfacial area from a model of mixed-wet triangular tubes, *Water Resources Research*, 43, W12S10.

Hiltzman, D. O. (1988), Review of microbial enhanced recovery field tests, p. VI 1-VI 41. In T. E. Burchfield and R. S. Bryant (ed.), *Proceedings of the Symposium on Applications of Microorganisms to Petroleum Technology*, National Technical Information Service, Springfield, Virginia..

Hiltzman, D. O. (1982), Petroleum microbiology and the history of its role in enhanced oil recovery. p. 162-218. In E. C. Donaldson and J. B. Clark (ed.) *Proceedings of the 1982 Conference on Microbial Enhancement of Oil Recovery*, CONF-8205140. U.S. Department of Energy, Bartlesville, Oklahoma.

His, C.D., Dudzik, D.S., and Buettner, J.W. (1994), Formation Injectivity damage due to produced water reinjection, *presented at the Society of Petroleum Engineers International Symposium on Formation Damage Control*, Lafayette, Louisiana, 7-10 Feb, SPE 27395

Jackson, S. C., Alsop, A., Choban, E., D'Achille, B., Fallon, R., Fisher, J., Hendrickson, E., Hnatow, L., Keeler, S., Luckring, A., Nopper, R., Norvell, J., Perry, M., Rees, B., Suchanec, D., Wolstenholme, Thrasher, D. and Pospisil, G. (2010), Microbial EOR – critical aspects learned from the lab, *presented at the 2010 Society of Petroleum Engineers Improved Oil Recovery Symposium* held in Tulsa, Oklahoma, 24-28 April, SPE 129657.

Javaheri, M., G. E. Jenneman, M. J. McInerney, and R. M. Knapp (1985), Anaerobic production of a biosurfactant by *Bacillus-licheniformis* JF-2, *Applied and Environmental Microbiology*, *50*(3), 698-700.

Jenneman, G. E., McInerney, M. J., Knapp, R. M., Clark, J. B., Ferro, J. M., Revus, D. E., and Menzie, D. E. (1983), A halotolerant biosurfactant-producing *Bacillus* species potentially useful for enhanced oil recovery, Chapter 45, *Developments in Industrial Microbiology,* 24: 485–492.

Joekar-Niasar, V., S. M. Hassanizadeh, and H. K. Dahle (2010), Non-equilibrium effects in capillarity and interfacial area in two-phase flow: dynamic pore-network modeling, *Journal of Fluid Mechanics*, 655, 38-71.

Joekar-Niasar, V., S. M. Hassanizadeh, and A. Leijnse (2008), Insights into the relationship among capillary pressure, saturation, interfacial area and relative permeability using pore-network modeling, *Transport in Porous Media*, 74, 201-219.

Kalaydjian, F., and B. Legait (1987), Slow displacement of 2 immiscible fluids by countercurrent in spontaneous imbibition, in a constricted tube, *Comptes Rendus De L Academie Des Sciences Series II*, *304*(15), 869-873.

Kang, Z., Yeung, A., Foght, J., and Gray, M. (2008), Mechanical properties of hexadecane-water interfaces with absorbed hydrophobic bacteria, *Colloids and Surfaces B: Biointerfaces*, 62, 273-279.

Karpyn, Z. T., M. Piri, and G. Singh (2010), Experimental investigation of trapped oil clusters in a water-wet bead pack using X-ray microtomography, *Water Resources Research*, *46*, 25.

Karpyn Z. T. and Piri, M. (2007), Prediction of fluid occupancy in fractures using network modeling and x-ray microtomography I: data conditioning and model description, *Physical Review E*, 76, 016315.

Kianipey, S. A. D. (1990), Mechanisms of oil displacement by microorganisms. Microbial Enhancement of Oil Recovery – Recent Advances, ed. E.C. Donalsdon, *Amsterdam: Elservier Science Publishers*.

Kowalewski, E., Rueslåtten, I., Gilje, E., Sunde, E., Bødtker, G., Lillebø, B., Torsvik, T., Stensen, J., Bjørkvik, B., and Strand, K.(2005), Interpretation of microbial oil recovery from laboratory experiments, *paper presented at the 13th European Sympsium on Improved Oil Recovery*, Budapest, Hungary, 25-27 April.

Kumar, M., Fogden, A., Senden, T., and Knackstedt, M. (2010) Investigation of pore-scale mixed wettability, *Society of Petroleum Engineers*, SPE 129974.

Kumar, M., and Fogden, A. (2009), Patterned wettability of oil and water in porous media, *Langmuir*, *26*(6), 4036-4047.

Kumar, M., Senden, T., Knackstedt, M., Lathan, S., Pinczewski, V., Sok, R., Sheppard, A., and Turner, M. (2008), Imaging of pore scale distribution of fluids and wettability, SCA2008-16, *International Symposium of the Society of Core Analyst*, Abu Dhabi, UAE 29 October-2 November.

Lappin-Scott, H. M., Cusack, F., and Costerton J. W. (1988), Nutrient resuscitation and growth of starved cells in sandstone cores: a novel approach to enhanced oil recovery, *Applied Environmental Microbiology*, 54:1373-1382.

Lake, L. W. (1996), Enhanced oil recovery, *Prentice Hall*, 1st edition ISBN-10: 0132816014.

Lazar, I. (1991), MEOR field trials carried out over the world during the last 35 years. *Developments in Petroleum Science*, 31, 485-530.

Leverett, M. C. (1940), Capillary behavior of porous solids*, The American Institute of Mining, Metallurgical, and Petroleum Engineers*, Tulsa Meeting, October.

Lin, S. C., Sharma, M., and Georgiou G. (1993), Production and deactivation of biosurfactant by *Bacillus licheniformis* JF-2, American Chemical Society, *Biotechnology Prog*ress, 9, 138-145.

Lin, S. C., Minton, M. A., Sharma, M. M., and Georgiou, G. (1994a), Structural and immunological characterization of the biosurfactant produced by *Bacillus-licheniformis* JF-2, *Applied and Environmental Microbiology*, *60*(1), 31-38.

Lin, S. C., Carswell, K. S., Sharma, M. M., and Georgiou, G. (1994b), Continuous production of the lipopeptide biosurfactant of *Bacillus-licheniformis* JF-2, *Applied Microbiology and Biotechnology*, *41*(3), 281-285.

Lindquist, W. B. (2002), Quantitative analysis of three-dimensional x-ray tomographic images, *Proceedings of the International Society of Optics and Photonics, SPIE 4503*, 103.

Lindquist, W.B. and Venkatarangan, A. (1999), Investigating 3D geometry of porous media from high resolution images, *Physics and Chemistry Earth (A),* 25, 593.

Lindquist, W.B., Lee, S.M., Coker, D., Jones, K. and Spanne, P. (1996), Medial axis analysis of void structure in three-dimensional tomographic images of porous media, *Journal of Geophysical Research,* 101B 8297.

Liu, Y., D. D. Nolte, and L. J. Pyrak-Nolte (2011), Hysteresis and interfacial energies in smooth-walled microfluidic channels, *Water Resources Research*, 47, W01504.

MacLeod, F. A., Lappin-Scott, H. M., and Costerton, J. W. (1988), Plugging of a model rock system by using starved bacteria, *Applied Environmental Microbiology*, 54:1365-1372.

Man H. N. and Jing X. D. (2002), Network modeling of mixed-wettability on electrical resistivity, capillary pressure and wettability indices, *Journal of Petroleum Science and Engineering*, 33, 101-122.

Manrique, E., Thomas, C., Ravikiran, R., Izadi, M., Lantz, M., Romero, J., and Alvarado, V. (2010), EOR: current status and opportunities*, Society of Petroleum Engineers Improved Oil Recovery Symposium*, Tulsa, Oklahoma, 24-28 April, SPE 130113.

Manthey, S., S. M. Hassanizadeh, R. Helmig, and R. Hilfer (2008), Dimensional analysis of two-phase flow including a rate-dependent capillary pressure-saturation relationship, *Advances in Water Resources*, 31, 1137-1150.

Marmur, A. (2009), Solid-surface characterization by wetting, *Annual Review of Materials Research*, *39*, 473-489.

Mayer, A. S. and Miller, C. T. (1992), The influence of porous medium characteristics and measurement scale on pore-scale distributions of residual non-aqueous-phase liquids, *Journal of Contaminate Hydrology,* 11, 189–213.

McInerney, M. J., Sublette, K. L and Montgomery, A. D. (1991), Microbial control of the production of sulfide, *Dev. Pet. Sci.,* 31, 441-449.

McKinley, V. L., Costerton, J. W., and White, D. C. (1988), Microbial biomass, activity, and community structure of water and particulates retrieved by backflow from a waterflood injection well, *Applied Environmental Microbiology*, 54:1383-1393.

Melrose, J. C., and C. F. Brandner (1974), Role of capillary forces in determining microscopic displacement efficiency for oil-recovery by water flooding, *Journal of Canadian Petroleum Technology*, 13 (4), 54-62.

Morrow, N. R. and Mason G. (2001), Recovery of oil by spontaneous imbibition, *Current Opinion in Colloid and Interface Sciences*, 6, 321-337.

Morrow, N. R., Chatzis, I., and Taber, J. J. (1985), Entrapment and mobilization of residual oil in bead packs*, presented at 60th SPE Conference*, Las Vegas, Nevada, SPE 14423.

Motealleh, S., Ashouripashaki, M., DiCarlo, D., and Bryant, S. (2010), Mechanisms of capillary-controlled immiscible fluid flow in fractionally wet porous media, *Vadose Zone Journal*, 9, 610-623.

Mu, B., Wu, Z., Chen, Z.,Wang, X., Ni, F., and Zhou, J. (2002), Wetting behavior on quartz surfaces by the microbial metabolism and metabolic products. Paper presented as the *7th International Symposium on Wettability and its Effects on Oil Recovery*, Tasmania, Australia, March 12 – 14.

O'Carroll, D. M., K. G. Mumford, L. M. Abriola, and J. I. Gerhard (2010), Influence of wettability variations on dynamic effects in capillary pressure, *Water Resources Research*., 46, W08505.

O'Carroll, D. M., T. J. Phelan, and L. M. Abriola (2005), Exploring dynamic effects in capillary pressure in multistep outflow experiments, *Water Resources Research*., 41, W11419.

Oh, W. and W. Brent Lindquist, (1999), Thresholding by indicator kriging, *Institute of Electrical and Electronics Engineers Transactions on Pattern Analysis and Machine Intelligence*, vol. 21, no. 7, 590-602.

Okasha, T.M, Funk, J., Al-Enezi, S., and Al-Rashidi, H., (2004) Fifty years of wettability measurements in the Arab-D Carbonate, *International Symposium of the Society of Core Analysts*, Abu Dhabi, UAE, 5-9 October, SCA2004-03.

Ollivier, B. and Magot M. (2005), Petroleum microbiology, *American Society of Microbiology Press*, Herndon, VA, ISBN 1-55581-327-5.

Pappas, T. N. (1992), An adaptive clustering algorithm for image segmentation, *Institute of Electrical and Electronics Engineers Transactions Signal Processing Society*, 40(4):901-914.

Payatakes, A. C., Ng, K. M., and Flummerfelt, R. W. (1980), Oil ganglia dynamics during immiscible displacement. Model formulation, *American Institute of Chemical Engineers Journal*, 26, 430-442.

Piri, M. and Karpyn Z. T. (2007), Prediction of fluid occupancy in fractures using network modeling and x-ray microtomography II: results, *Physical Review E*, 76, 016316.

Polson, J., Buckman, J., Bowne, D., Todd, A., Gow, M., and Cuthbert, S. (2010), An environmental-scanning-electron-microscope investigation into the effect of biofilm and the wettability of quartz, *Society of Petroleum Engineers Journal*, SPE 114421.

Porter, M. L., Schaap, M. G., and Wildenschild D. (2009), Lattice-Boltzmann simulations of the capillary pressure-saturation-interfacial area relationship of porous media, *Advances in Water Resources*, 32 (11), 1632-1640.

Porter, M. L., Wildenschild, D., Grant, G., and Gerhard, J. I. (2010), Measurement and prediction of the relationship between capillary pressure, saturation, and interfacial area in a NAPL-water-glass bead system, *Water Resource Research*, 46, W08512.

Porter, M. L., and D. Wildenschild (2010), Image analysis algorithms for estimating porous media multiphase flow variables from computed microtomography data: a validation study, *Computational Geosciences*, 14(1), 15-30.

Porter, M. L., M. G. Schaap, and D. Wildenschild (2009), Lattice-Boltzmann simulations of the capillary pressure-saturation-interfacial area relationship for porous media, *Advances in Water Resources*, 32(11), 1632-1640.

Prodanović, M., Lindquist, W., and Seright, R. (2006), 3D image-based characterization of fluid displacement in Berea core, *Advances in Water Resources*, vol. 30.

Pyrak-Nolte, L. J., D. D. Nolte, D. Chen, and N. J. Giordano (2008), Relating capillary pressure to interfacial areas, *Water Resources Research*, 44, W06408.

Reeves P. C., M. A. Celia (1996), A functional relationship between capillary pressure, saturation and interfacial area as revealed by a pore-scale network model, *Water Resources Research*, 32(8):2345–58.

Roehl, P. O. and Choquette, P. W. (editor) (1985), Carbonate petroleum reservoirs, *Springer-Verlag*, New York, 622P.

Röling, W. F. M., Head I. M., and Larter S. R. (2003), The microbiology of hydrocarbon degradation in subsurface petroleum reservoirs: perspectives and prospects, *Research in Microbiology*, 154:321-328.

Salatheil, R. A. (1973), Oil recovery by surface film drainage in mixed-wettability rocks, *The American Institute of Mining, Metallurgical, and Petroleum Engineers Transactions*, October, 1216-24, 255.

Schnaar G. and Brusseau M. L. (2006), Characterizing pore-scale configuration of organic immiscible liquid in multiphase systems with synchrotron x-ray microtomography, *Vadose Zone Journal,* 5, 641-648.

Schnaar, G. and Brusseau M. L. (2006), Characterizing pore-scale configuration of organic immiscible liquid in multiphase systems with synchrotron x-ray microtomography, *Vadose Zone Journal*, 5:641-648.

Schnaar G. and Brusseau M. L. (2005), Pore-scale characterization of organic immiscible-liquid morphology in natural porous media using synchrotron x-ray microtomography, *Environmental Science and Technology,* 39, 8403-8410.

Sethian, J. A., and P. Smereka (2003), Level set methods for fluid interfaces, *Annual Review of Fluid Mechanics*, 35, 341-372.

Sethian, J. A. (1996) Level set methods evolving interfaces in geometry, fluid mechanics, computer vision, and material science, *Cambridge Monographs on Applied and Computational Mathematics, Cambridge University Press*, ISBN 0-521-57101-9.

Sheppard, A., Sok, R., and Averdunk, H. (2004), Techniques for image enhancement and segmentation of tomographic images of porous media, *Physica A*, 339, 145-151.

Soudmand-asli, A., S. S. Ayatollahi, H. Mohabatkar, M. Zareie, and S. F. Shariatpanahi (2007), The in situ microbial enhanced oil recovery in fractured porous media, *Journal of Petroleum Science and Engineering*, *58*(1-2), 161-172.

Stadler, A.F., G. Kulik, D. Sage, L. Barbieri, and P. Hoffmann (2006), A snake-based approach to accurate determination of both contact points and contact angles, *Colloids and Surfaces A: Physicochemical And Engineering Aspects*, vol. 286, no. 1-3, 92-103, September.

Stalkup, F. I., Jr., (1984), Miscible displacement, *Society of Petroleum Engineers Monograph*, Richardson, Texas, p. 3.

Suthar, H., K. Hingurao, A. Desai, and A. Nerurkar (2009), Selective plugging strategy based microbial enhanced oil recovery using *Bacillus licheniformis* TT33, *Journal of Microbiology and Biotechnology*, 19 (10), 1230-1237.

Suthar, H., K. Hingurao, A. Desai, and A. Nerurkar (2008), Evaluation of bioemulsifier mediated microbial enhanced oil recovery using sand pack column. *Journal of Microbiological Methods*, 75, 225-230.

Tweheyo, M. T., Holt, T., and Torsæter O. (1999), An experimental study of the relationship between wettability and oil production characteristics, *Journal of Petroleum Science and Engineering*, 24, 179-188.

U.S. Census Bureau, International Data Base, August 2006; http://www.census.gov/

van Genuchten M. Th.(1980), A Closed-form equation for predicting the hydraulic conductivity of unsaturated soils, *Soil Science Society of America Journal,* 44:892-898.

Venkateswaran, K.; Moser, D. P.; Dollhopf, M. E.; Lies, D. P.; Saffarini, D. A.; MacGregor, B. J.; Ringelberg, D. B.; White, D. C.; Nishijima, M.; Sano, H.; Burghardt, J.; Stackebrandt, E.; Nealson, K. H. (1999) Polyphasic taxonomy of the genus *Shewanella* and description of *Shewanella oneidensis* sp. nov., *International Journal of Systematic Bacteriology*, *49*, 705-724.

von der Schulenburg, D. A. G., T. R. R. Pintelon, C. Picioreanu, M. C. M. Van Loosdrecht, and M. L. Johns (2009), Three-dimensional simulations of biofilm growth in porous media, *American Institute of Chemical Engineers Journal*, 55(2), 494-504.

Wankui, G., Chengfang, S., Zhenyu, Y., Zhaowei, H., Rui, J., Ying, W., Jiyuan, Z., and Guoghao, S. (2006), Microbe-enhanced oil recovery technology obtains huge success in low-permeability reservoirs in Daqing oilfield, SPE 104281*. Proceedings of SPE Eastern Regional Meeting*. Society of Petroleum Engineers, Richardson, TX.

Wardlaw N. C. and McKellar M. (1985), Oil blob populations and mobilization of trapped oil in unconsolidated packs*, Canadian Journal of Chemical Engineering*, 63: 525:532.

Wildenschild D., Hopmans, J. W., Rivers, M. L., and Kent A. J. R. (2005) Quantitative analysis of flow processes in a sand using synchrotron-based x-ray microtomography. *Vadose Zone Journal*, Vol. 4, issue 1, 122-126.

Wildenschild D., Hopmans, J. W., Vaz C. M. P., Rivers, M. L., Rikard D., and Christensen B. S. B. (2002), Using x-ray computed tomography in hydrology: systems, resolutions and limitations. *Journal of Hydrology*, 267:285-297.

Wilhelms, A., Larter, S. R., Head, I. M., Farrimond, P., di-Primio, R., and Zwach, C. (2001), Biodegradation of oil in uplifted basins prevented by deep-burial sterilization, *Nature*, 411:1034-1037.

Willhite, G. P. and Green, D. W. (1998), Enhanced Oil Recovery, *Society of Petroleum Engineers Textbook Series*, Vol. 6, SPE, Richardson, TX.

Yakimov, M. M., M. M. Amro, M. Bock, K. Boseker, H. L. Fredrickson, D. G. Kessel, and K. N. Timmis (1997), The potential of *Bacillus licheniformis* strains for in situ enhanced oil recovery, *Journal of Petroleum Science and Engineering*, *18*(1-2), 147-160.

Youssef, N., M. S. Elshahed, and M. J. McInerney (2009), Microbial processes in oil fields: culprits, problems, and opportunities, *Advances in Applied Microbiology,* vol. *66*, edited, pp. 141-251, Elsevier Academic Press Inc., San Diego.

Zhang, F., She, Y. H., Ma, S. S., Hu, J. M., Banat, I. M. and Hou, D. J. (2010), Response of microbial community structure to microbial plugging in a mesothermic petroleum reservoir in China, *Applied Microbiology and Biotechnology,* 88, 1413-1422.

Zhao, X., Blunt, M., and Yao, J. (2010) Pore-scale modeling: effects of wettability on waterflood oil recovery, *Journal of Petroleum Science and Engineering*, 71, 169-178.

Appendix A. Investigating Biomineralization using Synchrotron Based X-ray Computed Microtomography

Ryan T. Armstrong[1] and Jonathan Ajo-Franklin[2]

1. School of Chemical, Biological and Environmental Engineering, Oregon State University, 103 Gleeson Hall, Corvallis, Oregon, 97331-2702

2. Earth Science Division, Lawrence Berkeley National Laboratory, Berkeley, California, 94720

Geophysical Research Letters
2000 Florida Avenue N.W.
Washington, DC 20009-1277
Published 4/28/2011

A.1 Abstract

This work presents the results of a study where synchrotron based x-ray computed microtomography (CMT) was used to investigate changes in pore morphology during calcium carbonate biomineralization. We simultaneously examine changes in pore microstructure and bulk permeability in glass bead columns during biogenic $CaCO_3$ precipitation induced by *Sporosarcina pasteurii*. We observe a three order of magnitude reduction in permeability over relatively short time-scales (~60 hrs) during the carbonate precipitation process. The resulting precipitates were a micro-porous composite of spherical and cubic $CaCO_3$ precipitates. CMT images taken during precipitation were analyzed for effective pore radii, effective throat radii, and other pore-scale characteristics using 3DMA-ROCK. The Kozeny-Carman relation provided a poor fit to the raw permeability data, however, once this function was augmented with geometric information extracted from CMT imagery a better fit was provided suggesting that pore geometry should be considered temporally variable when modeling permeability change during biomineralization.

A.2 Introduction

Biomineralization is a natural subsurface process that can dramatically alter the physical properties of porous media. In particular, porosity and permeability changes, attributed to biologically assisted $CaCO_3$ precipitation, can have a direct effect on fluid flow and transport properties (Whiffin et al. 2007). A key factor relevant to permeability alteration is the characteristic pattern of precipitation with respect to the granular matrix i.e. are precipitates localized in pore throats, pore bodies, or on grain surfaces? Since effective medium models describing permeability (e.g. *Carrier*, 2003) and elastic properties (Dvorkin et al. 1999) are dependent on such patterns, the appropriate choice of a scenario or trajectory between scenarios (i.e. where is precipitation localized and how does localization change temporally) is a key step in building a quantitative understanding of the effects of biomineralization.

We selected *Sporosarcina pasteurii* as our model organism for studying the mineralization process, a prevalent aerobic, rod-shaped, motile, soil microbe with a very active urease enzyme (Whiffin et al. 2007). Hydrolysis of urea by the urease enzyme generates carbon dioxide and ammonia {$CO(NH_2)_2 + H_2O \rightarrow 2NH_3 + CO_2$}, causing an increase in pH {$2NH_3 + 2H_2O \leftrightarrow 2NH_4^+ + 2OH^-$}. In this alkaline environment carbonate ions form {$CO_2 + 2OH^- \leftrightarrow$

CO_3^{2-} + H_2O} and precipitation of calcium carbonate is favored {CO_3^{2-} + Ca^{2+} ←→ $CaCO_3$(s)}, (Stocks-Fischer et al. 1999).

One of the simplest permeability models is the Kozeny-Carman (KC) model which attempts to describe permeability in terms of porosity starting from first principles (*Carrier*, 2003). The KC function often fails to represent empirical data; however, this type of relationship is vital for the design and modeling of many engineered processes (e.g. geological carbon storage and hydrocarbon recovery).

A complete derivation of the KC functions (Equation A.1 and A.2) used herein is presented by (*Costa*, 2006). Permeability can be calculated using:

$$\kappa = c\left(R^2/8\right)\left(\theta/\tau\right) \quad \text{(A.1)}$$

where, R is effective radius, τ is tortuosity, and θ is porosity. However, R and τ are hard to measure/define, thus the concept of hydraulic radius is usually defined and incorporated into Equation 1 which gives the following formula:

$$\kappa = C_{kc}\left(\theta^3\right)/\left(1-\theta\right)^2 \quad \text{(A.2)}$$

where, C_{kc} is an empirical constant. Equation A.2 is essentially the classical KC function and is the starting point of our analysis. Average effective throat radius measured from CMT imagery is incorporated into Equation 1 and fitted to the empirical data.

A.3 Methods

A.3.1 Experimental Setup

A schematic of the flow-through bioreactor (L = 12 mm, ID = 8 mm) is provided in Figure A.1. The reactor was equipped with internal pressure ports and separate flow lines for urea media and calcium chloride to prevent precipitation outside the column. The column was packed with 600 μm diameter soda lime glass beads.

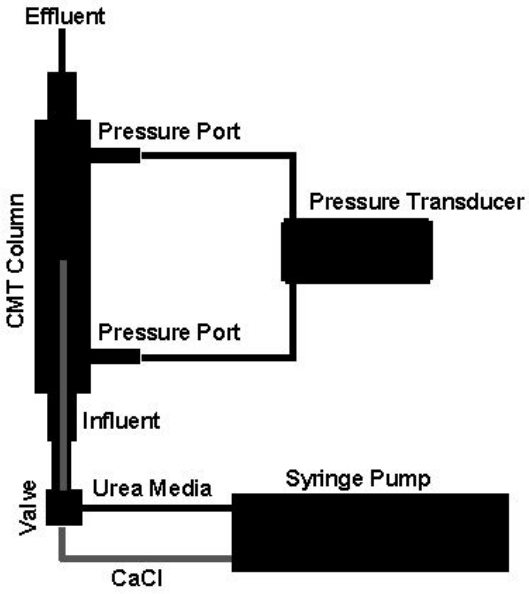

Figure A.1: Flow-through bioreactor (L = 12 mm, ID = 8 mm) piping schematic for urea media and calcium chloride solution. The CaCl flow line extends into the columns vertical center to reduce the potential for clogging to occur at the inlet.

A.3.2 Cementation Treatment

S. pasteurii (ATCC 6453) was grown to late exponential stage (~18 hours) in batch culture. Prior to inoculation, microbes were rinsed with urea media (20.0 g $CO(NH_2)_2$, 10.0 g NH_4Cl, 2.1 g $NaHCO_3$, 3.0 g Difco Nutrient Broth, total volume 1.0 L DI H_2O) by three rounds of centrifugation and resuspension in fresh urea media followed by pH adjustement to 6.5 with 1 N HCl. Columns were inoculated with approximately 10^{10} cells/ml and flow was discontinued for 4 hours allowing the microbes to revive and increase pore water pH. After the stagnant period urea media was pumped at 1.00 ml/hr and $CaCl_2$ (100 g/L) at 0.067 ml/hr (using a Harvard '33' syringe pump) giving a total Darcy velocity of 5.9E-6 m/hr and a 20mM calcium concentration.

A.3.3 Computed Microtomography

Imaging was performed at Beamline 8.3.2 at the Advanced Light Source (ALS), Lawrence Berkeley National Laboratory. Projections were acquired at 4.5 µm/pixel resolution with a monochromatic energy of 30 KeV and flow was discontinued during each scan which took ~40 minutes.

A.3.4 Porosity and Permeability Measurements

Permeability was measured under fixed flux conditions using a differential pressure transducer (Validyne, Model P55D, 1 PSI differential). CMT volumes were segmented into solid and fluid phases for porosity calculations. After applying a median filter (3x3x3 kernel) it was determined that a simple threshold was sufficient to segment the solid (glass and calcium carbonate) and liquid phases (Figure A.2).

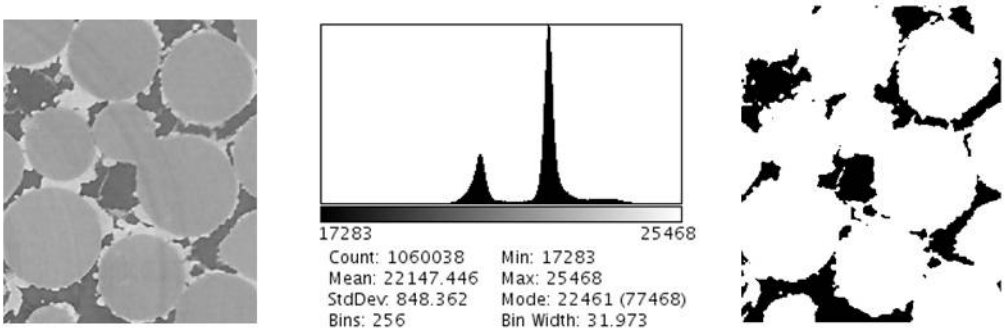

Figure A.2: Images were segmented after applying a median filter; 16-bit gray scale median filtered image (left), image histogram (middle), and binary image (right). To identify the calcium carbonate phase the column was scanned prior to precipitation and used for image subtraction from the final column image.

A.3.5 Image Analysis Using 3DMA-ROCK

Segmented volumes were imported into 3DMA-ROCK (3DMA) for medial axis and pore body/throat construction. When referring to the 3DMA data, effective pore radi is the radius of a sphere of equivalent volume and effective throat radi is the radius of a circle of

equivalent area. For more detailed information on the algorithms used in 3DMA refer to the manuscript by (Prodanović et al. 2006) and references therein.

Since medial axis and pore body/throat construction can be time intensive the analyzed image volume was restricted to a volume that could be processed in a reasonable amount of time. A volume of 25 mm^3 was found reasonable and took ~40 hours on a 64GB RAM, dual quad core Xeon X5355 2.66GHz processor platform to process.

A.4 Results

In total, 5 columns were analyzed, 1 column was a clean bead pack used to characterize the system prior to precipitation and the other 4 columns contained bioprecipitates. Once a column was imaged with CMT the experiment was ceased. This type of terminal sampling was required since preliminary experiments showed that x-ray exposure during a scan ($2.2*10^{11}$photons/(s mm^2), ~40 minutes) killed 99 out of 100 microbes.

Porosity and permeability data for the 5 columns which range in porosity from 0.35 to 0.26 and had measured permeabilities ranging from 4 D to 20mD are shown in Figure A.3. The clean glass bead pack is labeled as 5 in Figure 1. For the column with the smallest porosity change labeled as 4 in Figure A.3 the cementation treatment took ~1day, the two columns labeled 3 and 2 in Figure A.3 with intermediate porosity changes were treated for ~2 days, while the column with the greatest porosity change labeled 1 in Figure A.3 was treated for ~3 days. The porosity profile over the vertical axis for each column is shown in Figure A.3a. The average porosity versus measured permeability is shown in Figure A.3b and shows a dramatic decrease in permeability from the starting point at $\theta = 0.35$ (5) for a clean glass bead pack to $\theta = 0.26$ (1) for a completely cemented packing. Initially the KC function ($\kappa = C_{kc}(\theta^b)$) was fitted to the raw data in log space with C_{ck} = 7.0E-7 and b = 16.54 providing the best fit possible, however, the variable b deviates far from realistic b values derived from KC theory (Figure A.3b).

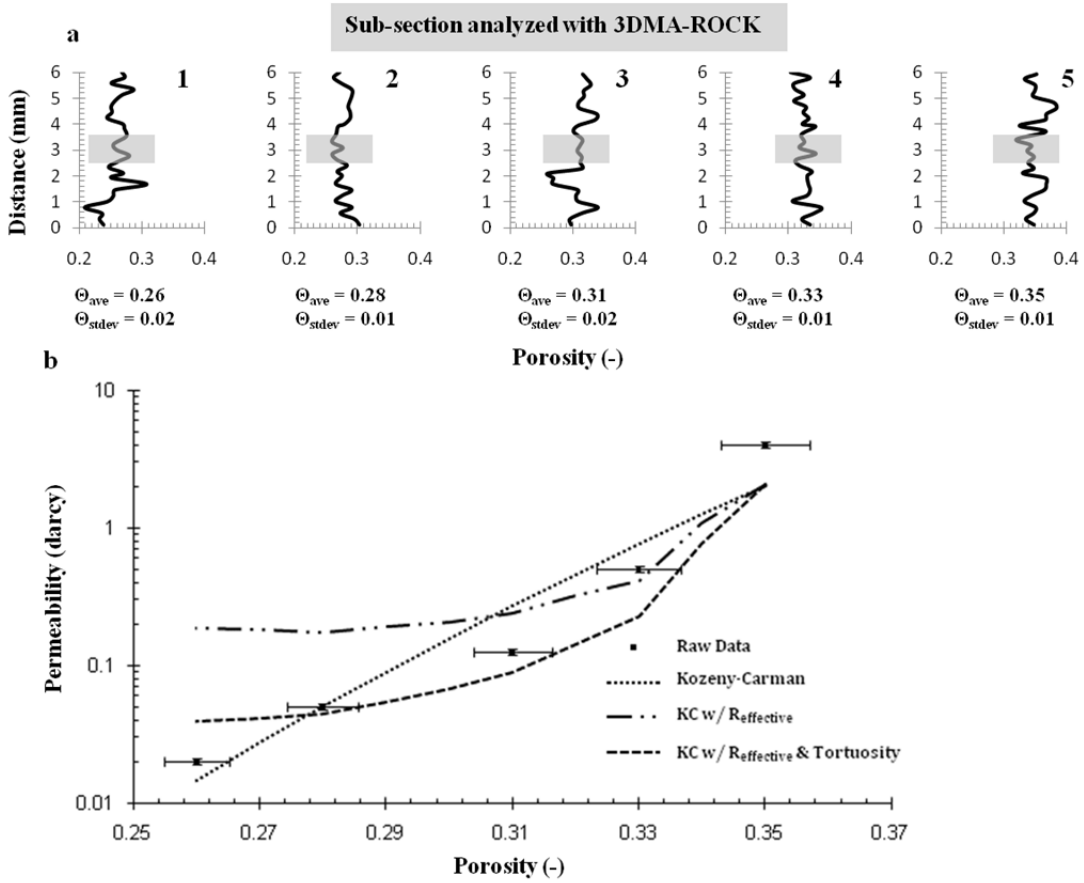

Figure A.3: The Porosity distributions between the pressure transducer ports for each column labeled 1 through 5 are shown in (A).The porosity-permeability data along with the KC curves are shown in (B). Each data point in (B) is labeled 1 through 5 and the given porosity value corresponds to the mean porosity value calculated from the porosity distributions shown in (A). The mean porosity and standard deviation for each column is reported directly below its corresponding porosity distribution graph.

The average effective pore body radius, average effective pore throat radius, and permeability for each column are shown in Figure A.4. The average effective pore body and average effective throat radii decrease during precipitation. Because a fixed water flux was imposed by pumping, mean pore velocity and pore pressure significantly increases in the highly precipitated channel. Washout of precipitates was observed in the lower permeability columns and was likely due to this increased pore velocity; however, no data is available to quantify the amount of precipitate that was washed out.

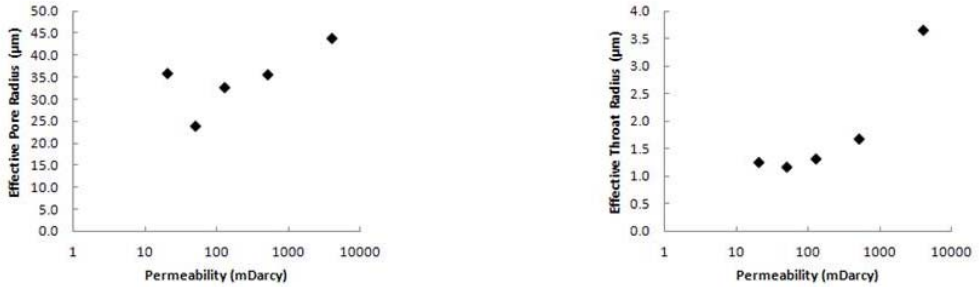

Figure A.4: Correlation plots generated from 3DMA-Rock data.

As shown in the CMT images provided in Figure A.5a, b & c calcium carbonate appears to precipitate on the glass bead surface and extend outward into the pore-space. This type of arrangement is indicative of the coupling of mass transfer and growth kinetics where calcium must diffuse from the bulk pore-space to the reactive surface (Figure A.5c) where precipitation occurs and extends the surface outward into the pore-space. However, this arrangement could also be attributed to inconsistent local cell densities causing a variation in precipitation rate. Either way, this effectively causes some regions to develop “peaks” where precipitation is favored (i.e. accelerated). These “peak” regions extend into the pore-space dividing up what was a single pore into multiple pores (as identified by 3DMA, Figure A.4) and in some locations enough precipitation occurs that adjacent beads become cemented together.

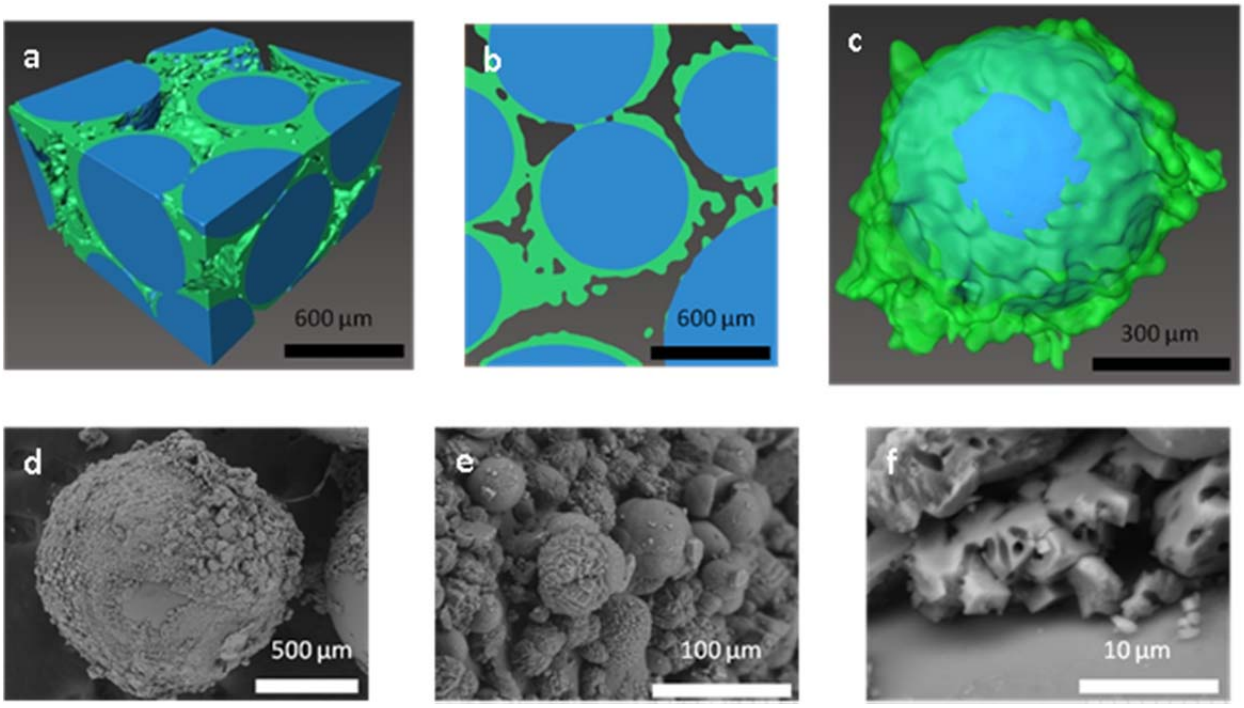

Figure A.5: CMT images are labeled a, b, and c (blue = glass, green = CaCO3). SEM images are labeled d, e, and f.

To better represent the permeability data with the KC function, average effective throat radius ($R_{effective}$) data were used to supplement Equation A.1. For porosity values where $R_{effective}$ values were not available, a linear interpolation between measured $R_{effective}$ values was used. Tortuosity was held constant at 1.5 (average theoretical tortuosity for a clean glass bead pack) and the KC function with $R_{effective}$ was fit to the raw data, results (Figure A.3b) show a better fit, however, this function still failed to represent the empirical data (fitting parameter, C = 5.3). In a third attempt tortuosity was used as a fitting parameter and allowed to change for each porosity value. The KC function with $R_{effective}$ and tortuosity included provided the best fit (Figure A.3b, fitting parameters, C = 5.3 & τ = 1.5 to 7.2). However, this approach still did not completely represent the empirical data and a tortuosity value of 7.2 seems unrealistic. Most likely, in the case of biomineralization, the KC function is too simple to properly represent the complex porosity-permeability relationship. However, two reasonable propositions that could explain our inability to predict the empirical data with the KC function must be addressed, which are either (1) sub-CMT resolution precipitate morphology is significantly reducing permeability or (2) biofilm formation which is not visible with CMT is reducing permeability.

To address the first proposition, backscattered electron SEM images (Hitachi TM-1000, Figure 2D, E, & F) of the precipitates were acquired; the excavated samples were drained and air dried at 30° C for 48 hours before being mounted with carbon tape and imaged in low vacuum conditions to mitigate charging artifacts. SEM images show that calcium carbonate precipitates are an assemblage of spherical and cubic precipitates that are micro-porous. Figure A.5 suggests that when modeling biomineralization the precipitate should not be considered a solid phase, and thus, its internal micro-porosity should be considered. However, it is reasonable to suggest that micro-porosity would not dramatically affect permeability since the pores appear too small for bulk advective transport. Figuress A.6 and A.7 provide additional details concerning the mixed precipitate morphology and precipitate composition. As found by Fredrich et al. 2006, the relationship between porosity and permeability depends on effective porosity and not the disconnected microporosity that exists at near sub-CMT resolution. Overall, micro-porosity is more likely an important parameter when considering reactivity, structural soil mechanics, and the geophysical signature of biomineralization.

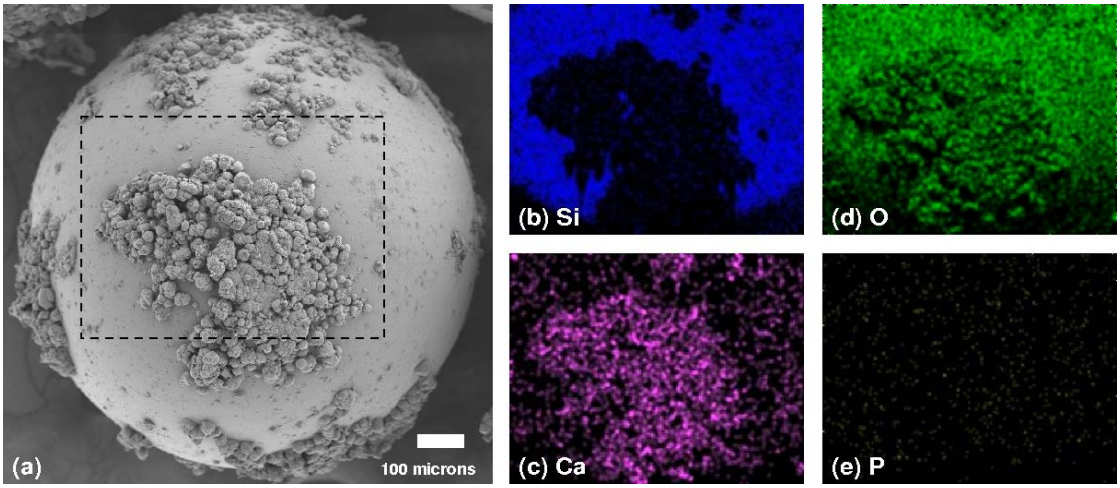

Figure A.6: Results of SEM/EDS characterization of precipitates covering bead surface: verification of precipitate composition. A sample from one of the reacted micro-columns was drained, air-dried for 48 hours at 50 C, and mounted on an SEM stub using carbon tape followed by Au/Pd coating. The sample was then imaged using a Zeiss Ultra 55 in high vacuum mode with a 5 kEv beam current. Both SEM and EDS data (EDAX detector, 10mm2) were acquired for a select region of the sample. EDS data was acquired in a qualitative capacity due to the significant surface topography which makes quantitative elemental mapping procedures problematic. Panel (a) shows a secondary electron image of one glass bead with precipitates extracted from a reacted micro column. Panels (b,c,d,e) show elemental maps for Si, Ca, O, and P as characterized by EDS for the inset area. As can be seen, the glass bead is Si rich (SiO2) while the precipitates are Ca rich (presumably CaCO3) with O present in both phases. Phosphorus, a component of the media with crystallization potential, is not present in significant amount. Maps of Cl (not shown) demonstrate that negligible CaCl remained on the grain surface. Small amounts of Ca are present in the glass (aprox. 9% by weight); this results in a measurable Ca fraction outside of the precipitate region (frame c). Fe, Mg, and Al were not present in large amounts. Considering the available cation supply present in the reactor influent, these results verify that the precipitates are CaCO3 as anticipated.

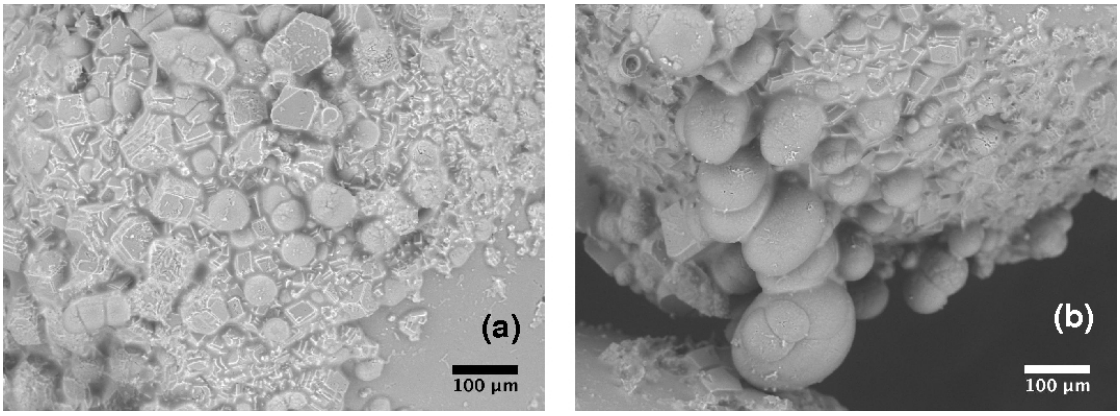

Figure A.7: Results of environmental SEM characterization of precipitates showing mixed morphology (cubic vs. spheroidal). A sample from one of the reacted micro-columns was drained, air dried for 24 hours at 30 C, and mounted on an SEM stub with carbon tape. The uncoated sample was imaged under low vacuum to avoid charging effects in a low pressure SEM (Hitachi TM-1000) with a small water film intact. Panels (a) and (b) show BSE images of two areas with examples of precipitates composed of a mixture of morphologies; spheroidal features (presumably vaterite) in close proximity with more crystalline cubic features (presumably calcite).

A second possibility is clogging due to accumulated non-mineral biological products. Microbes and exopolymeric substances have very similar x-ray attenuation coefficient as water and are not readily seen with CMT, thus any additional clogging due to bioaccumulation would not have been accounted for. However, recent confocal laser scanning microscopy images of *S. pasteurii* reported by (Shultz et al. 2011) show that this particular organism forms a very sparse biofilm. Nevertheless, permeability reduction due to biofilm formation cannot be ruled out, at this point.

A.5 Conclusion

Our results demonstrate that traditional KC models are not sufficient for predicting the porosity-permeability relationship observed during biomineralization and geometric information from CMT images were needed to supplement the KC function. A similar conclusion was reached by Chen et al. 2008, where inorganic colloid deposition in an initially simple porous media produced sufficient internal complexity, such that, the KC function could not provided a good fit. Pore morphology dramatically changed as a result of precipitation, increasing the number of pore bodies (and throats) and decreasing the

effective radii of pore throats and pore bodies. The discrepancy with the simple KC function suggests that field scale reactive transport models will require more sophisticated porosity/permeability models to effectively capture changes in transport properties generated during bioremediation or biologically-enhanced CO_2 sequestration. Overall, biomineralized $CaCO_3$ substantially reduced permeability. When modeling this reduction, porosity, effective throat radius, tortuosity, and the biofilm phase should be considered to vary both spatially and temporally.

A.6 Acknowledgments

Primary support was provided by the U.S. DOE Biological and Environmental Research Program (contract DE-AC02-05CH11231) through the LBNL Sustainable Systems Scientific Focus Area. Secondary support for J.A-F, provided by the Center for Nanoscale Control of Geologic CO_2, an Energy Frontier Research Center, funded by U.S. DOE, Office of Basic Energy Sciences (contract DE-AC02-05CH11231). We also thank Jamie Nasiatka (ALS, BL8.3.2) for flowcell design, Maša Prodanović (UT Austin) for providing 3DMA, Qianoa Hu for SEM imaging assistance, and Dorthe Wildenschild (OSU) for computing support. CMT work was performed with the assistance of Alastair MacDowell at the Advanced Light Source, Beamline 8.3.2, which is supported by the Office of Science, Office of Basic Energy Sciences, of the U.S. DOE (contract DE-AC02-05CH11231). Microbiological work was performed with the assistance of Caroline Ajo-Franklin as a User project at the Biological Nanostructure Facility in the Molecular Foundry (LBNL) which is supported by the Office of Science, Office of Basic Energy Sciences, of the U.S. DOE (contract DE-AC02—05CH11231).

A.7 References

Carrier D. (2003), Goodbye, Hazen; Hello, Kozeny-Carman, J. Geotech. *Geoenviron. Eng.* , vol. 129.

Chen, C., Packman, A. I., and Gaillard, J.-F. 2008, Pore-scale analysis of permeability reduction resulting from colloid deposition, *Geophysical Research Letters*, 35, L07404.

Costa, A. (2006), Permeability-porosity relationship: a reexamination of the Kozeny-Carman equation based on a fractal pore-space geometry assumption, *Geophys. Res. Lett.*, vol. 33, L02318.

Dvorkin, J., Berryman J., and Nur, A. (1999), Elastic moduli of cemented sphere packs, *Mech Mater.*, vol. 31.

Fredrich, J.T., DiGiovanni, A.A., and Noble, D.R. (2006), Predicting macroscopic transport properties using microscopic image data, *J. Geophys. Res.*, 111, B03201.

Prodanović, M., Lindquist, W., and Seright, R. (2006), 3D image-based characterization of fluid displacement in Berea core, *Adv. Water Resour.*, vol. 30.

Schultz, L., Pitts, B., Mitchell A., Cunningham, A., and Gerlach, R. (2011), Imaging Biologically-Induced Mineralization in Fully Hydrated Flow Systems. *Microsc. Today.* March 2011, 22-25.

Stocks-Fischer, S., Galinat, J., and Bang, S. (1999), Microbiological precipitation of $CaCO_3$, *Soil and Biology and Biochemistry*, vol. 31.

Whiffin, V., van Paassen, L., and Harkes, M. (2007), Microbial Carbonate Precipitation as a Soil Improvement Technique, *Geomicrobiol. J.*, vol. 24.

Appendix B. Imaging Biofilm Architecture within Porous Media using Synchrotron-Based X-Ray Computed Microtomography

Gabriel C. Iltis[1], Ryan T. Armstrong[1], Danielle P. Jansik[1], Brian D. Wood[1] and Dorthe Wildenschild[1]

1. School of Chemical, Biological and Environmental Engineering, Oregon State University, 103 Gleeson Hall, Corvallis, Oregon, 97331-2702

Water Resources Research
2000 Florida Avenue N.W.
Washington, DC 20009-1277
Published 2/17/2011

B.1 Abstract

A new method to resolve biofilms in three dimensions in porous media using high-resolution synchrotron-based x-ray computed microtomography (CMT) has been developed. Imaging biofilms in porous media without disturbing the natural spatial arrangement of the porous medium and associated biofilm has been a challenging task, primarily because porous media generally preclude conventional imaging via optical microscopy; x-ray tomography offers a potential alternative. Using silver-coated microspheres for contrast, we were able to differentiate between the biomass and fluid-filled pore-spaces. The method was validated using a two-dimensional micro-model flow cell where both light microscopy and CMT imaging were used to image the biofilm.

B.2 Introduction

Biofilms are observed in both natural and engineered systems, and are believed to be the primary habitat for most microorganisms (Costerton et al. 1995). In porous media, biofilm growth and development occurs over a continuum of scales ranging from nanometers to millimeters or more and has been a topic of interest in applications and industries including mining, filtration, water and wastewater treatment, and bioremediation (e.g. Fitch et al. 1998; Rawlings and Johnson, 2007; Rodriquez and Bishop, 2008). Due to the prevalence of biofilm in both natural and engineered porous media systems, a significant effort has been undertaken to understand biofilm growth and development in porous media, yet much of the information about the three-dimensional architecture of biofilms in porous media is based on the results of mathematical models rather than on direct experimental data. In order to verify and validate existing and new models, experimental data quantitatively detailing the structural arrangement and distribution of biofilm in porous media is required.

Visualization of the biological phase in porous media is a useful means for increasing our understanding of microbial-soil structure interactions and for developing quantitative experimental data sets for mathematical model validation. Conventional techniques for imaging biofilm include light microscopy (e.g. Paulsen et al. 1997; Sharp et al. 2005; Yang et al. 2000), Environmental Scanning Electron Microscopy (ESEM) (e.g. Davis et al. 2009), and Confocal Laser Scanning Microscopy (CLSM) (e.g. Leis et al. 2005; Rodriguez and Bishop, 2007), all of which are useful for examining biofilm on surfaces or in two-dimensional or quasi-two-dimensional porous systems. While the aforementioned imaging techniques are

capable of providing significant insight regarding microbial interaction and biofilm structural formation, imaging porous-media-associated biofilm using these techniques requires that model porous media systems be constrained to a few particle diameters, that the porous medium and fluid be index-matched, or that samples be extracted and prepared, thereby disrupting the pore scale structure. Thus, new techniques that allow for direct visualization of biofilm *in situ* are required in order to characterize biofilm growth, surface architecture, and three-dimensional spatial distribution within porous media to provide relevant experimental data for the verification and validation of porous media associated biofilm growth models. One such technique utilized by a number of groups to measure the three-dimensional features of biofilms is magnetic resonance microscopy (MRM) (Manz et al. 2003; Seymour et al. 2004; Seymour et al. 2007). In terms of gross structural characterization, these techniques have generally been successful. However, thus far the method has been limited in resolution (50-100 μm), and the acquisition time is very large, which could severely limit the method for some applications.

A new methodology using synchrotron based X-ray computed microtomography (CMT) to render high-resolution measurements of the spatial distribution of biofilms in porous media is presented in this work. This methodology has the advantages that (i) a variety of solid substrates can be used; and (ii) the method is non-destructive to the porous medium allowing for three-dimensional *in situ* visualization of biofilm. CMT has been available for more than three decades and has been a powerful tool for studying a wide array of processes in porous media systems (e.g. Nunan et al. 2006; Werth et al. *2010*; Wildenschild et al. 2002). However, synchrotron-based tomographic imaging of biofilms has yet to be accomplished, primarily due to the fact that obtaining x-ray contrast between the biomass and water has posed a significant challenge since conventional contrast agents, such as potassium iodide, diffuse readily into biofilm when present in the fluid phase. An additional consideration when selecting elements to use as contrast agents is the energy range of the synchrotron beam line to be used for tomographic imaging. The K-shell absorption edge for the element selected as a contrast agent must fall within the beam line energy range in order to provide sufficient contrast for segmentation. To address the contrast issue, we used a silver-based fluid-phase contrast agent that provides x-ray absorption contrast between the fluid and biofilm phases by adsorbing to the surface of the biofilm, and thereby delineating the biofilm/aqueous phase interface. To our knowledge, we report the first use of synchrotron based CMT to image biofilm within porous media as well as method validation using a separate imaging technique.

B.3 Methods

Two-dimensional micro-model flow cells were constructed from PDMS (poly-dimethyl siloxane). The inner dimensions of the flow chamber were 9.8 x 30.0 x 3.4 mm with 1 mm diameter cylindrical columns spaced 1 mm apart, see Figure B.1. *Shewanella oneidensis* MR-1 was used in all experiments. *S. oneidensis* MR-1 is a Gram negative, facultatively anaerobic, polarly flagellated bacteria capable of dissimilatory metal reduction and biofilm formation (Majors et al, 2005; Venkateswaran et al. 1999). Cultures were grown for 24 hrs in a 10% Tryptic Soy Broth (TSB) solution, concentrated at 6000 rpm for 10 minutes, resuspended in 5 ml of 10% TSB followed by inoculation of the micro-model flow cell. The injected culture sat stagnant for 24 hrs allowing for microbial attachment to the surfaces, followed by flow of 10% TSB solution at 0.01 ml/min for 12 days. Neutrally buoyant hollow silver-coated microspheres with an average diameter of 10 µm (particle range: 5-15um based on coulter counter measurements, Microsphere Technology Ltd, Pentlands Science Park, Edinburgh EH26 0PZ, UK) were deposited at the biofilm surface by flowing a concentrated solution (approximately 4 mg microspheres/mL) through the micro-model, followed by subsequent rinsing with 10% TSB to remove spheres not attached to the biomass. Imaging commenced following the micro-model rinse in order to limit the potential for biofilm rearrangement due to the antimicrobial nature of the silver microspheres.

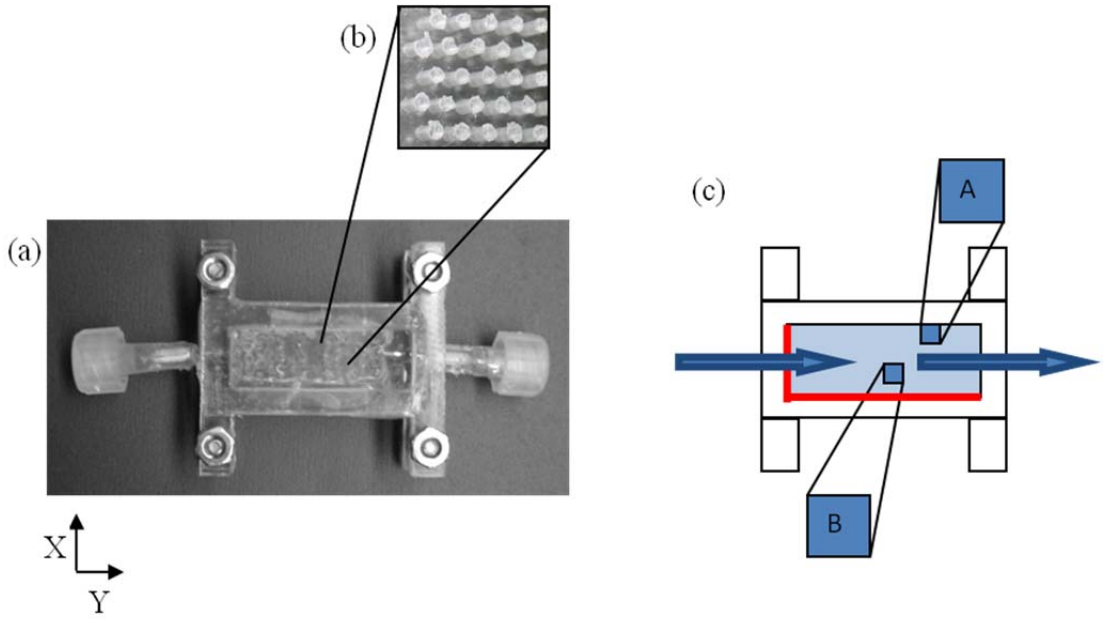

Figure B.1: Micro-model flow cell detail: (a) Example two-dimensional micro-model flow cell constructed from PDMS (poly-dimethyl siloxane). The inner dimensions of the flow chamber are 9.8 X 30.0 X 3.4 mm with 1 mm diameter cylindrical columns spaced 1 mm apart. (b) Close up detail of the cylindrical columns molded into the flow cell. (c) Plan view schematic of the flow cell. The arrows indicate the flow direction. Details A and B correspond to the locations of Features A and B. The shaded area corresponds to the region of porous matrix. The red lines correspond to the X and Y datum from which spatial measurements for locating the feature regions were taken.

A Leica Z16 APO light microscope was used to acquire light microscopy images of the micro-model at a resolution of 1.4 µm/pixel. Regions of the micro-model containing unique, identifiable, biofilm features were observed using digital microscopy; the locations of the biofilm features were measured with a stage micrometer using the micro-model sidewall as a datum. Biofilm features were mapped in all three principal dimensions to enable alignment with the CMT data. The entire micro-model flow cell was imaged using CMT and regions of interest were located in the reconstructed volume using the microscope coordinate measurements, see Figure B.1.

Microtomographic imaging was performed at beamline 8.3.2 at the Advanced Light Source (ALS), Lawrence Berkeley National Laboratory. Preliminary experiments were performed at beamline 13-BMD, GSECARS at the Advanced Photon Source (APS/ GSECARS), Argonne

National Laboratory. The data collected at the ALS and APS was acquired at resolutions of 4.5 μm/pixel and 11.8 μm/pixel respectively. An energy level slightly above the K-shell absorption edge for silver (25.5 keV) was used for imaging to optimize x-ray absorption and thus contrast.

Image reconstruction, post-processing, and segmentation were carried out with scripts written in Interactive Data Language (IDL®), and using the commercially available visualization software Avizo®. The grayscale images were coarsened to a 4.5 μm/pixel resolution corresponding to the resolution of the CMT data. Raw CMT data was pre-processed by integrating (or collapsing) volume data in the light microscopy image region of interest into a single slice for direct comparison of representative images. All images were then processed using a standard Sobel edge detection algorithm followed by segmentation using a simple histogram threshold. For additional information on the Sobel edge detection algorithm we refer to the IDL software documentation as well as to *Duda and Hart* (1973). The PointWrap surface generating algorithm in Avizo® was then applied to the resulting binary images to generate surfaces for quantification of the spatial distribution of biofilm. The PointWrap algorithm generates a surface reconstruction from a cloud of unorganized points by simulating the path of a sphere through a cloud of points or along a surface. A triangulated mesh is generated by assuming that a surface exists every time a set number of points are in contact with the simulated sphere body simultaneously. This algorithm allows for the association and interconnection of a cloud of points, which corresponds to the individual silver-coated microspheres adhering to the surface of the biofilm. For additional information on the PointWrap algorithm, we refer to the Avizo® software documentation as well as to *Sander and Runge* (2000). The PointWrap analysis was also verified using a standard marching cubes surface-generating algorithm. Surface area error estimates generated using the two methods varied by less than one percent.

Volume rendering of the CMT data for three-dimensional evaluation of the biofilm was also done using the Avizo® software package. The volume files were segmented to differentiate between the solid (PDMS) and silver particles. A Sobel edge detection filter was applied in order to segment the silver particles. Volumetric quantitative analysis using both the PDMS (solid-phase) as well as the silver micro-sphere (biofilm) surfaces as indices was performed using the triangulated mesh created using the PointWrap algorithm in Avizo®.

B.4 Results

Preliminary experimentation using the new imaging approach was conducted at the APS and provided compelling evidence that our choice of contrast agent and CMT imaging method produces realistic three-dimensional representations of biofilm present in the experimental packed bead column system. A visualization of the preliminary results is provided in Figure B.2. Figure B.2 indicates that biofilm (green) forms both on the surfaces of the glass beads within the column (gold) as well as within the column pore-space bridging multiple beads together. In order to validate our preliminary findings, we developed the previously mentioned system in which the distribution of biofilm could be visualized using both digital microscopy and CMT (Figure B.3). This validation of the CMT imaging technique for visualizing biofilm *in situ* in porous media is the focus of this work.

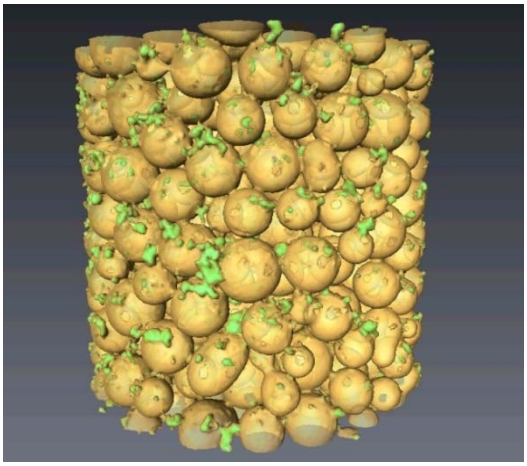

Figure B.2: Preliminary three-dimensional CMT biofilm imaging results of biofilm (green) grown in a glass bead pack (gold). The visualization experiment was performed at the Advanced Photon Source (APS), Argonne National Laboratory, using neutrally-buoyant, silver-coated hollow glass spheres (10 um diameter) as an x-ray contrast agent. The spatial arrangement of the silver particles is interpreted as being attached to the biomass grown within the bead pack.

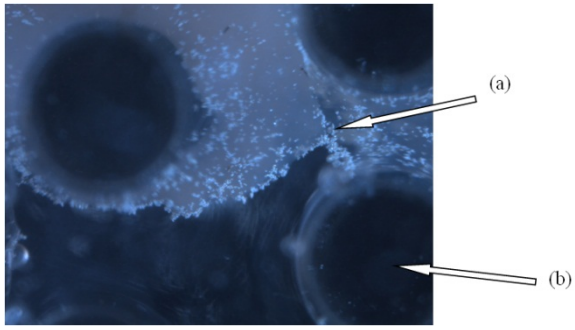

Figure B.3: Light microscopy image detailing the distribution and adherence of silver-coated hollow glass micro-spheres to the biofilm surface. The silver particles can be seen to adhere solely to the biofilm (a) as opposed to the PDMS column posts (b) indicating that spatial distribution of silver particles within the x-ray tomography data corresponds to the location of biofilm.

In the two-dimensional micro-model used for validation, two distinct regions of the micro-model flow cell containing *S. oneidensis* biofilm were selected for analysis (Features A and B). Visualizations of the light microscopy and composite CMT images of both features are depicted in Figure B.4 along with the processed binary and PointWrap biofilm representations. The flow cell column posts have been superimposed as gray circles in the grayscale images for ease of interpretation. Visual comparison of the light microscopy images to the CMT composite images indicate very good agreement between the imaging methods and suggest that the silver particles detected using CMT do, in fact, allow for the delineation of biofilm within the pore-space. The correlation between the two imaging techniques for Features A and B was quantified, via surface area, using the PointWrap surface generating algorithm on the binary images resulting in a percent error for the CMT images, normalized to the light microscopy images, of between 1-5%. Results of the comparison are detailed in Table B.1.

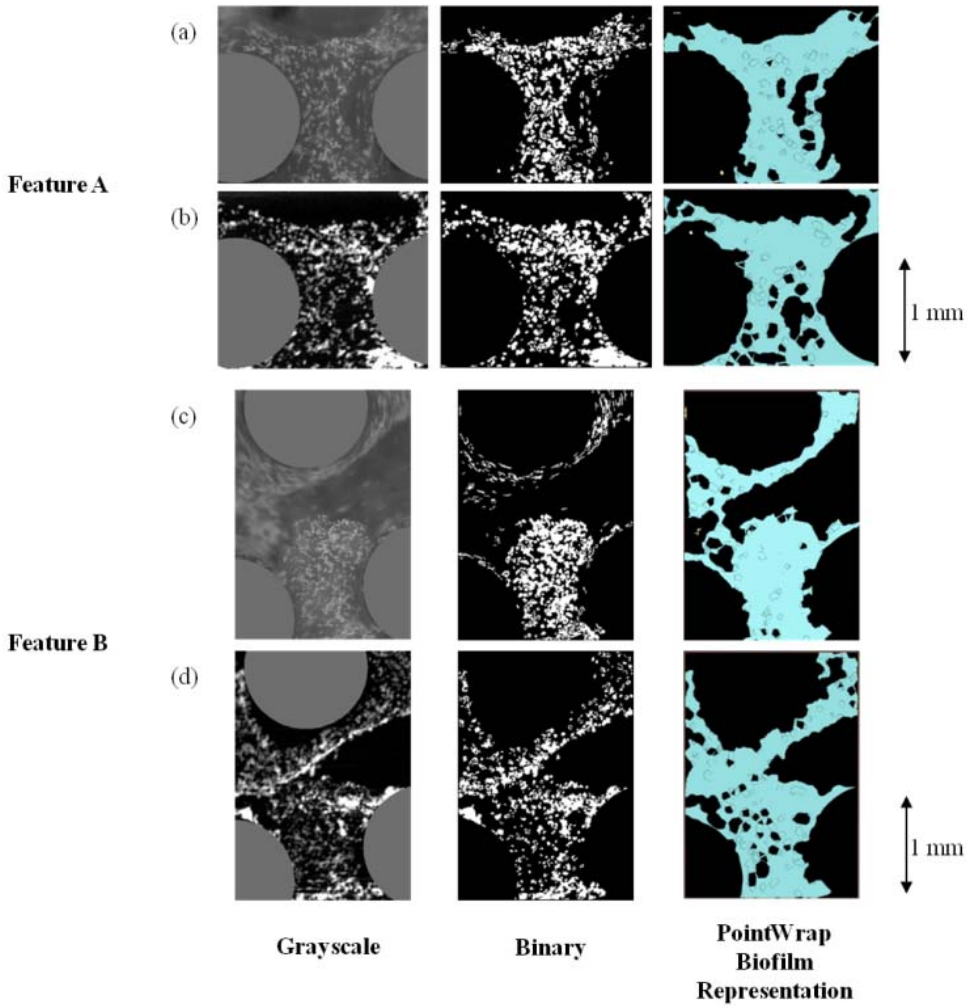

Figure B.4: Comparison of light microscopy images to representative CMT images for two unique biofilm features at the grayscale, binary and PointWrap stages of image processing. Dark areas correspond to fluid, light/grey areas show silver particles attached to biofilm. The light blue regions in the PointWrap images correspond to the representative region containing biofilm. (a) Light microscopy images of Feature A, (b) CMT images of Feature A, (c) Light microscopy images of Feature B, (d) CMT images of Feature B.

Table B.1: Quantitative comparison of the light microscopy and representative two-dimensional CMT images for two unique biofilm features using the Avizo® PointWrap algorithm.

	Surface Area	Absolute Error Normalized to Light Microscopy Image
	mm^2	%
Feature A Light Microscopy	1.595	-
Feature A Computed Microtomography	1.529	4.13
Feature B Light Microscopy	1.998	-
Feature B Computed Mictrotomography	2.034	1.82

Three-dimensional renderings that illustrate the spatial distribution of biofilm within the porous medium for Features A and B are provided in Figure B.5. Through the use of the PointWrap algorithm, the volume change and change in macroporosity associated with biofilm growth were quantified for both features. The volume of biofilm associated with Features A and B were calculated to be 1.67 mm^3 and 2.44 mm^3, which corresponds to decreases in macroporosity from 63% to 48% for Feature A and from 68% to 50% for Feature B. This three-dimensional analysis is included to illustrate the potential for quantification that the technique allows for.

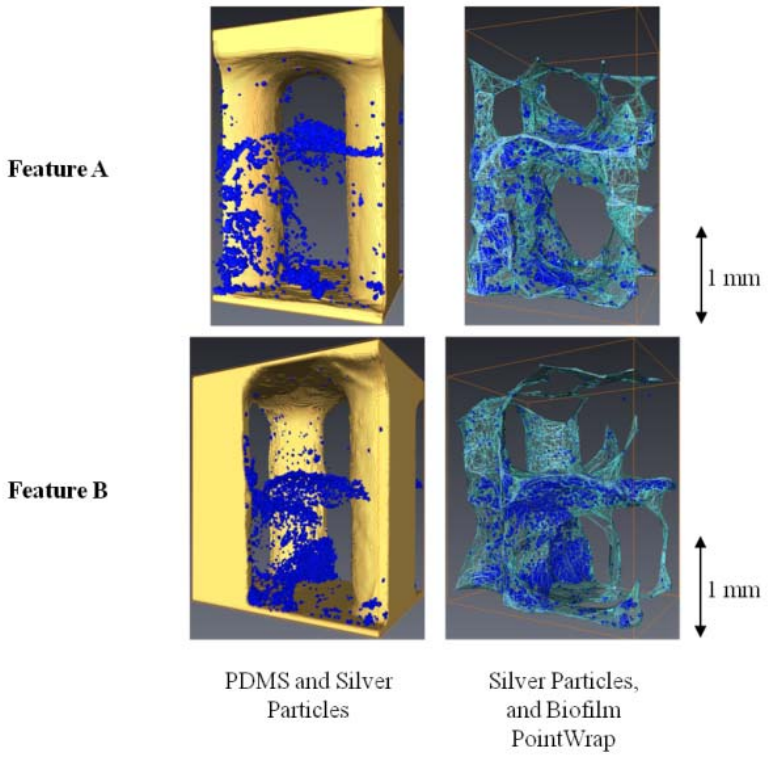

Figure B.5: Volume renderings of biofilm growth at two unique locations within the micro-model flow cell captured using synchrotron based CMT. The PDMS solid phase (gold) has a measured volume of 4.26 mm^3 and 4.31 mm^3 for Features A and B, corresponding to initial porosities of 63% and 68% respectively. The measured volume of the biofilm for Features A and B are 1.67 mm^3 and 2.44 mm^3 resulting in a decrease in macroporosity of 15% and 18%, respectively.

B.5 Discussion

Validation of CMT imaging of biofilm in porous media using silver-coated glass microspheres as a contrast agent to outline a biofilm surface was successful. The microspheres adhere to the *S. oneidensis* biofilm-aqueous phase interface providing the necessary contrast needed for CMT imaging. Light microscopy images showed good correlation with representative CMT images, and biofilm volume renderings could be created from a cloud of points generated by the distribution of silver particles across the biofilm interface with the aqueous phase. Currently, the technique facilitates three-dimensional imaging of biofilm within porous media and accurately represents the solid-biofilm-aqueous phase spatial arrangement. This method is particularly suited for pore-scale investigations were a triangulated mesh can be generated which provides a convenient platform for additional analysis (for example, fluid

and solute transport within the biofilm via a finite element or finite volume numerical simulator).The proposed CMT-based method can image biofilm within porous media with high fidelity and also allows measurement *in situ* to a biologically-relevant environment. Secondly, CMT can image at the micron scale and still provide spatial information at the centimeter scale. The beamline setup (beam width) ultimately determines the maximum sample diameter that can be imaged. The maximum specimen diameters at the beamlines utilized in this manuscript are approximately 4 to 5 cm. However, the image resolution is dependent on the magnification of the lens attached to the detector which decreases the applicable sample diameter. In general, the resulting image resolution is 1/1000 of the specimen diameter. The sample length (axial length) is effectively limited by the acceptable data acquisition time for the collection of multiple scans at different heights. Thus, CMT can provide biofilm spatial distribution over many centimeters in the sample axial direction and resolve interfacial architecture at the micron resolution. A key benefit to using CMT to image biofilm in porous media is that no limitation to direct surface access or visualization depth exists, as in the case of CLSM. Additionally, refractive index matching of the porous medium is not required since attenuation and optical transparency are not significant issues associated with the presented method. As a result, biofilms within their natural environments (e.g. soil and rock) can potentially be imaged *in situ*.

The key limitations to the method include 1) x-ray exposure associated with CMT imaging is expected to kill or severely retard microbial growth; 2) silver is a biocide and, for this reason, must be added to sample specimens immediately prior to imaging; 3) the ability to visualize biofilm is dependent on the extent of silver coverage on the biofilm surface; 4) the presented method, at this point, is limited in utility to imaging changes to the macropore structure of the porous medium, as a result the internal porosity of the biofilm is not imaged using this method. The effect of x-ray exposure as well as the introduction of silver microspheres is expected to have a negative impact on biofilm growth. As a result, the imaging of biofilm using the presented method should be considered the terminal step for particular specimens. The quality of coverage by silver particles on the surface of the biofilm is key to successful use of the presented method. Since the silver addition occurs immediately prior to imaging, surface attachment will be limited to biofilm surfaces exposed to flow channels through the micro-model or porous medium column. Dead end pores containing biofilm have the potential to be interpreted as fluid space if silver particles do not come into contact with the biofilm. Regions that are occluded from flow also have the potential to be attributed to biofilm if the region is surrounded by silver coated biofilm. Since the method relies on the

deposition of silver coated microspheres on the biofilm surface, the method is limited to providing insight into changes in macropore morphology external to the biofilm, however, the ability to acquire quantitative experimental data detailing the changes in macropore morphology can potentially provide insight into biofilm associated changes in porous media hydrodynamics as well as solute transport.

To our knowledge, this is the first successful attempt using high resolution CMT to image three-dimensional biofilms *in situ* within intact porous media. Both spatial distribution of biofilm and change in porosity are important parameters for investigating the impact of biofilm on porous media hydrodynamics, and on the mass transport and reaction processes that occur during bioremediation. Admittedly, we present one working approach for applying a contrast agent to biofilm for imaging using CMT. The method is potentially applicable using microspheres coated in a variety of elements; however, additional research into the efficacy of other contrast agents as well as the effect of varying particle size and density is ongoing.

B.6 Acknowledgements

This work was supported by the Environmental Remediation Science Program (DE-FG02-09ER64734) under the Department of Energy, Office of Biological and Environmental Research (BER), Grant No. ER64734-1032845-0014978. The work was performed at beam lines 8.3.2 at the Advanced Light Source (ALS), LBNL, and GeoSoilEnviroCARS (Sector 13), Advanced Photon Source (APS), ANL. The APS is supported by the U.S. Department of Energy, Basic Energy Sciences, Office of Energy Research, under Contract No. 248 W-31-109-Eng-38. We would like to thank Alastair MacDowell and James Nasiatka at Beamline 8.3.2, as well as Mark Rivers at GSECARS for assistance with CMT imaging.

B.7 References

Costerton, J., D. Lewandowski, D. Caldwell, D. Korber, H. Lappin-Scott (1995), Microbial biofilms, *Annu. Rev. Microbiol.*, *49*, 711-745.

Davis, D., L. Pyrak-Nolte, E. Atekwana, D. Werkema (2009), Microbial-induced heterogeneity in the acoustic properties of porous media, *Geophys. Res. Lett.,* 36, L21405.

Duda, R. O., and P. E. Hart (1973), Representation and Initial Simplification, in *Pattern Classification and Scene Analysis*, pp. 271-272, John Wiley, New York, N. Y.

Fitch, M., N. Pearson, G. Richards, J. Burken (1998), Biological fixed-film systems, *Water Environ. Res., 70*(4)*,* 495-518.

Leis, A. P., S. Schlicher, H. Franke, M. Strathmann (2005), Optically transparent porous medium for nondestructive studies of microbial biofilm architecture and transport dynamics, *Appl. Environ. Microbiol.*, *71*(8), 4801-4808.

Majors, P. D., J. S. McLean, G. E. Pinchuk, J. K. Fredrickson, Y. A. Gorby, K. R. Minard, R. A. Wind (2005), NMR methods for in situ biofilm metabolism studies, *J. Microbiol. Methods, 62*(3)*,* 337-344.

Manz, B., F. Volke, D. Goll, H. Horn (2003), Measuring local flow velocities and biofilm structure in biofilm systems with magnetic resonance imaging (MRI), *Biotechnol. Bioeng., 84*(4), 424-432.

Nunan, N., K. Ritz, M. Rivers, D. Feeney, I. Young (2006), Investigating Microbial Micro-Habitat Structure using X-ray Computed Tomography, *Geoderma, 133* (3-4), 398-407.

Paulsen, J.E., E. Oppen, R. Bakke (1997), Biofilm morphology in porous media, a study with microscopic and image techniques, *Water Sci. Technol., 36*(1), 1-9.

Rawlings, D., and D. Johnson (2007), The microbiology of biomining: development and optimization of mineral-oxidizing microbial consortia, *Microbiology, 153,* 315-324.

Rodriguez, S.J., and P.L. Bishop (2007), Three-dimensional quantification of soil biofilms using image analysis, *Environ. Eng. Sci., 24*(1), 96-103.

Rodriguez, S., and P. Bishop (2008), Enhancing the biodegradation of polycyclic aromatic hydrocarbons: Effects of nonionic surfactant addition on biofilm function and structure, *J. Environ. Eng.,* 134, 505-512.

Sander, O., and D. Runge (2000), Fast surface reconstruction using a probe sphere, *Konrad-Zuse-Zentrum fur informationstechnik Berlin,* Berlin-Dahlem, Germany, *ZIB-Report 00-50,* 1-10.

Seymour, J.D., J.P. Gage, S.L. Codd, R. Gerlach (2004), Anomalous fluid transport in porous media induced by biofilm growth, *Phys. Rev. Lett., 93*(19), 198103.

Seymour, J.D., J.P. Gage, S.L. Codd, R. Gerlach (2007), Magnetic resonance microscopy of biofouling induced scale dependent transport in porous media, *Adv. Water Resour., 30*(6-7), 1408-1420.

Sharp, R.R., P. Stoodley, M. Adgie, R. Gerlach, A. Cunningham (2005), Visualization and characterization of dynamic patterns of flow, growth and activity of biofilms growing in porous media, *Water Sci. Technol., 52*(7), 85-90.

Venkateswaran, K., D. P. Moser, M. E. Dollhopf, D. P. Leis, D. A. Saffarini, B. J. MacGregor, D. B. Ringelberg, D. C. White, M. Nishijima, H. Sano, J. Burghardt, E. Stackebrandt, K. H. Nealson, (1999), Polyphasic taxonomy of the genus Shewanella and description of Shewanella oneidensis sp. nov., *Int. J. Syst. Bacteriol., 49,* 705-724.

Werth, C.J., C. Zhang, M.L. Brusseau, M. Oostrom, T. Baumann (2010), A review of non-invasive imaging methods and applications in contaminant hydrogeology research, *J. Contam. Hydrol., 113*(104), 1-24.

Wildenschild, D., C. Vaz, M. Rivers, D. Rikard, B. Christensen (2002), Using X-ray computed tomography in hydrology: systems, resolutions, and limitations, *J. Hydrol. (Amsterdam, Neth.),* 267, 285-297.

Yang, X.M., H. Beyenal, G. Harkin, Z. Lewandowski (2000), Quantifying biofilm structure using image analysis, *J. Microbiol. Methods, 39*(2), 109-119.